MSc Thesis
Utrecht University
Supervisors: Prof.dr. C.J. Spiers, Dr. S.J.T. Hangx
Utrecht, May 2016

Field Data Correlation of Reservoir Compaction and Seismic Potential of Dutch Onshore Gas Fields

Fekkes, F.[1]

[1]Faculty of Geosciences, Utrecht University, f.fekkes@students.uu.nl

Abstract

The discovery of the Groningen gas field in 1959 led to a significant increase of the Dutch natural gas industry. Yet, deformation and stress changes in and around a reservoir during production may generate problems, such as surface subsidence due to compaction and seismicity due to fault induction on pre-existing faults. Induced seismic events are monitored since 1986 and at present times 1103 induced seismic events are registered, mainly located in the northern Netherlands. The magnitudes of these seismic events are reaching 3.6 on the Richter scale. This study correlates production and reservoir characteristics of 68 onshore gas fields in the northern Netherlands to the amount of surface subsidence and induced seismicity, thereby assessing vertical strain, total seismic moment and maximum seismic magnitude. Reservoir compaction and induced seismicity are both complex problems influenced by reservoir parameters that may also impact each other. As a consequence of the complexity of the problem and a limited data set, one univocal answer is not obtained and no single reservoir parameter can be assigned to solely contribute to reservoir compaction and seismic potential. Yet, several field parameters are interpreted to correlate well and confirm literature-based hypotheses. By examining individual reservoir parameters on their seismic potential, a general outline of a field that would be prone to seismicity is provided. In addition, field parameters that correlate well in this first level assessment cannot be ignored in further research, i.e. field porosity, length-to-width ratio, temperature, production time and reservoir depletion. Making comparisons with available knowledge considering sandstone compaction from lab experiments and theory, stress-strain curves are constructed and the translation between field and laboratory data is assessed. The experimental data results in values of one order of magnitude larger for vertical strain increase during depletion compared to field data. A generic model for bending of a clamped elliptical plate, representing anhydrite caprock or the incremental top part of a sandstone reservoir, confirms that geometry, i.e. the ratio between length and width of a field, and area are influencing the magnitude of deflection and changes in stress. Field data provides a good correlation with the model and fault reactivation can most likely be assigned to a combination of compaction and bending mechanisms in the reservoir and/or caprock.

Contents

List of Figures

List of Tables

1 Introduction

After the discovery of the Groningen gas field in 1959, exploration and production of natural gas in the Netherlands significantly increased (Herber and De Jager (2010)). This resulted in an average of 10 exploration wells per year with a rate of succes increasing from 0.3 to 0.4 at present times (Breunese et al. (2005)). The increasing natural gas industry was inherent to an economically and politically favorable position of the Netherlands, which developed into the main 'gas hub' of Europe (Herber and De Jager (2010)).

The deformation and changes of stress in a reservoir during the production of a field may generate problems, such as surface subsidence due to compaction and seismicity due to fault induction (Zoback (2010)). Induced seismic events are monitored by the Royal Netherlands Meteorological Institute since 1986 and at present times 1103 induced seismic events are registered, mainly located in the northern Netherlands. The magnitudes of these seismic events are reaching 3.6 on the Richter scale. Earthquakes are considered induced when the hypocenter equals the location and depth of a producing reservoir (Van Eijs et al. (2006); KNMI (2015)). In addition, natural seismic events mainly occur in the southeastern part of the Netherlands (Bourne et al. (2014)). Yet, a relatively large uncertainty concerning the position of the hypocenters of approximately 500 m laterally and 1-2 km vertically is present (KNMI (2015)). De Crook et al. (1998) determines the actual damage caused by induced seismicity to be mild, ranging from small, non-constructive damage on buildings to moderate, slightly constructive damage. The social consequences can however be severe, reflecting the relevance of research involving reservoir compaction and hence seismic potential to society (Van Eijs et al. (2006)). While constructive damage is the main concern considering onshore fields, fault reactivation may negatively impact offshore fields as well. Fault reactivation possibly decreases the sealing capacity of a fault by increasing permeability (Wiprut and Zoback (2000)). This results in a higher risk of a dry well when adjacent field compartments are severely depleted.

Compaction occurs when the overburden pressure stays constant while the pore fluid pressure decreases during the production of a field (Doornhof et al. (2006)). Considering only vertical stress and strain, the decrease in pore fluid pressure increases the vertical effective stress. The increased vertical effective stress during depletion thus causes a volumetric change of the pores in the reservoir, inducing strain in and around the reservoir, which is mostly accommodated by elastic deformation (Doornhof et al. (2006)). Since most onshore reservoirs in the northern Netherlands consist of high porosity rocks a large decrease in pore fluid pressure is expected, resulting in an increased potential for compaction and hence subsidence (NAM (2013)). The difference between pore pressure decrease in high porosity and permeability reservoir rocks and low porosity and permeability surrounding rocks during depletion results in a difference in strain or volumetric contraction observed in reservoir rocks compared to the surrounding rocks, which generates stress, also referred to as poroelastic stressing (Segall (1989); Segall (1992)). The stress generated in a depleting reservoir may trigger both time-independent elastic or recoverable and partly time-dependent plastic or permanent deformation of a reservoir (Hettema et al. (2002)). Segall and Fitzgerald (1998) refer to empirical evidence of the occurrence of induced seismicity, where the pore fluid pressure was decreased several tens of MPa during production of an oil or gas field. The poroelastic stress change associated with production occurs within or near a reservoir and may induce earthquakes due to fault slip. In most cases induced seismicity is assigned to slip on pre-existing faults in the subsurface (Van Eijs et al. (2006); Mulders (2003)). Segall (1989) states that slip on a pre-existing fault surface, i.e. fault reactivation, occurs when the frictional resistance of the existing slip planes is surmounted by the total shear stress, i.e. the surrounding or ambient stress plus the induced shear stress during production of a reservoir. This relation is usually illustrated by a Coulomb failure criterion, where the shear traction overcomes the normal traction times the coefficient of friction (Segall et al. (1994)). Although the above explains the mechanisms of reservoir compaction and seismicity, yet no uniform behavior of fields regarding these mechanisms can be seen and research is hence essential (Bourne et al. (2014)). Reservoir compaction and induced seismicity are possibly coupled to several field parameters or geological characteristics, thereby causing an individual reservoir to acquire a higher seismic potential during production (Van Eijs et al. (2006); Segall (1989)).

Zoback (2010) explains stress-strain data from a typical laboratory experiment for an uniaxially deformed rock. Over an axial stress range between approximately 9 to 45 MPa linear elastic behavior can be observed, followed by permanent strain with grain and pore collapse at higher stress, i.e. lower pore fluid pressure at constant vertical stress (Zoback (2010)). Thus, when a gradual reduction of the pore fluid pressure (depletion) causes the vertical effective stress to increase sufficiently, the inelastic part of the stress-strain curve may be reached. This implies a large increase in strain with little stress increase or further depletion. Looking at the simple mechanical response of different gas fields, it is determined in this study whether this increased permanent deformation occurs in the northern Netherlands as well.

The first research objective is to correlate production and reservoir characteristics or parameters with both compaction, i.e. vertical strain, and the amount of seismicity, i.e. total seismic moment or maximum seismic magnitude. The parameters are determined from 68 onshore gas fields that are mainly located in the northern Netherlands. The locations of the investigated fields including the locations representing the occurrence of induced seismicity are illustrated in figure 1. Next to the correlation with several reservoir parameters an attempt is made to explain reservoir compaction and ultimately seismicity by deriving stress-strain properties of the reservoir rocks. The individual stress-strain properties of each reservoir are determined by the field data obtained from 68 onshore gas fields in the northern Netherlands, making comparisons with available knowledge about sandstone compaction from lab experiments and theory. An important

factor in this approach is determining whether it has any predictive potential for seismicity, possibly having important implications on further exploration and production of natural gas reservoirs in the Netherlands and beyond.

Secondly an attempt is made to derive an analytical model that may explain the different amounts of reservoir compaction, subsidence and hence seismicity, in which it is determined whether compaction and fault reactivation mechanisms can be correlated with and understood from field data parameters. Hence focussing on field-based compaction models, an attempt is made to construct a simple model for the stress changes during depletion in different reservoirs, possibly effecting fault reactivation and energy release, i.e. seismicity.

Van Eijs et al. (2006) uses a statistical method correlating production properties of reservoirs to historical occurrence of seismic events, where a good correlation is observed between pressure drop at first earthquake, fault density in the reservoir and stiffness contrast between seal and reservoir rock. This study focuses on the correlation of field parameters with seismicity occurrence as well as compaction in a reservoir. In addition, this study considers laboratory experiments and a theoretical model, representing bending of a caprock and incremental top part of a reservoir during depletion. A first level assessment is hence provided, where after qualitative analysis reservoir parameters can be subdivided into two groups; parameters that possibly can be eliminated in further research and parameters that correlate with reservoir compaction and/or induced seismicity, which therefore cannot be eliminated in further research.

Summarizing, two key questions prevail in this study: *1) Can subsidence and hence ultimately seismic potential of Dutch onshore gas fields be correlated with and understood from field data?, and 2) Is there any predictive potential from such an approach?*

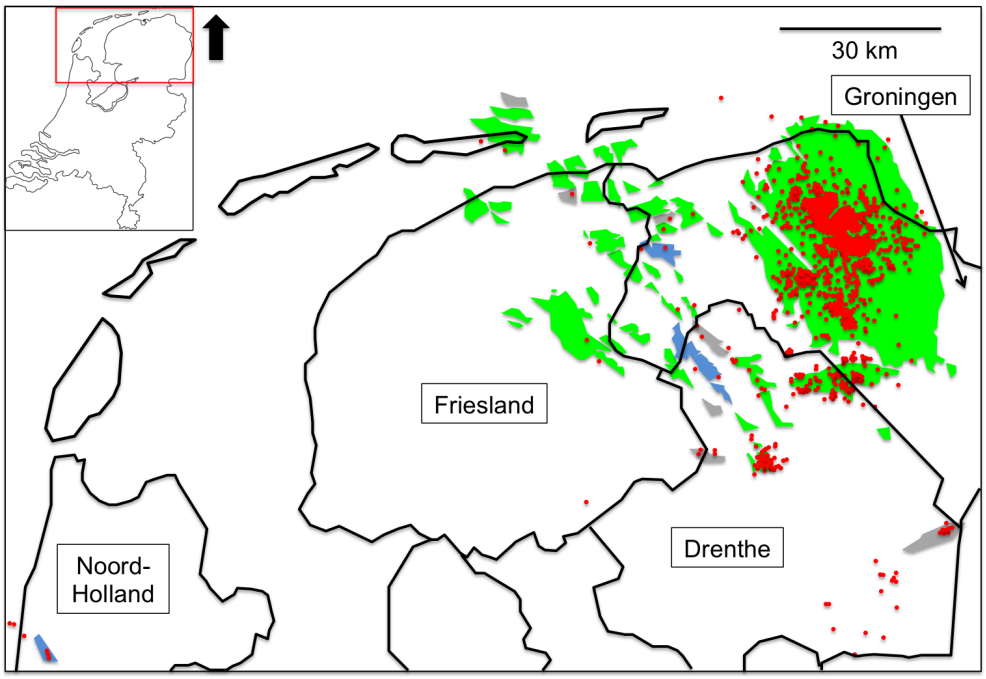

Figure 1: *A map of the northern Netherlands illustrating the locations of the 68 examined gas fields. The locations where induced seismicity has occurred are visualized by red dots. Blue fields represent fields used for underground gas storage, grey fields represent depleted gas fields and green fields represent producing fields (data from www.nlog.nl). N.B. Other fields apart from the 68 displayed gas fields are present in the northern Netherlands, but not displayed in this figure.*

2 Methodology

In light of answering the key questions in this study, reservoir compaction and seismic potential are approached from several perspectives, whereby firstly the main focus is on correlating reservoir and production parameters or characteristics to compaction, seismicity and laboratory experiments. Secondly, hypotheses resulting from the field data correlation are assessed by an analytical model.

2.1 Correlation of Reservoir Parameters

A database is constructed including a selection of both production and reservoir characteristics or parameters. The parameters that are examined in the 'Field Data Correlation' section of this study are listed in table 1. The field data of the following 68 onshore gas fields is used: *Ameland-Noord, Ameland-Oost, Ameland-Westgat, Anjum, Annerveen, Appelscha, Assen, Bedum, Bergermeer, Blija-Zuid, Blija Zuid-Oost, Blija-Ferwerderadeel, Blijham, Boerakker, Een, Eleveld, Engwierum, Ezumazijl, Faan, Feerwerd, Gasselternijveen, Grijpskerk UGS, Groningen, Grootegast, Harkema, Houwerzijl, Kielwindeweer, Kollum, Kollum-Noord, Kollumerland, Kommerzijl, Lauwersoog-C, Lauwersoog-Oost, Lauwersoog-West, Leens, Marum, Marumerlage, Metslawier, Moddergat, Molenpolder, Munnekezijl, Nes, Norg UGS, Norg-Zuid, Oostrum, Opende-Oost, Oude Pekela, Pasop, Roden (block 1), Roden (block 2), Rodewolt, Roswinkel, Saaksum (Oost), Saaksum (West), Sebaldeburen, Suawoude, Surhuisterveen, Tietjerksteradeel (Upper Rotliegend Group), Tietjerksteradeel (Vlieland Formation), Ureterp, Usquert, Vierhuizen (Oost), Vries (Noord), Vries (Zuid), Warffum, Witterdiep, Zevenhuizen and Zuidwending-Oost.* The majority of these fields is operated by NAM, except for the Bergermeer field, which is operated by TAQA. Since the Dutch mining law makes it obligatory for operators to publish field data, the selection of field data listed in table 1 is acquired from publicly available resources, e.g. end-off-well reports, well logs, petrophysical evaluations and winningsplannen. Surface subsidence data is for example inferred from NAM (2010), using satellite measurements (Interferometric Synthetic Aperture Radar or InSAR). Mean porosity of a field is determined by averaging the porosities of the reservoir strata from the end-of-well reports of all the wells drilled in that particular field. Reservoir temperatures are acquired by using the TNO ThermogGIS Expert software, from which temperatures of particular reservoir strata can be obtained. The compaction coefficient of several reservoir rocks is determined both in-situ and with laboratory experiments (NAM (2010)). The thickness of the primary caprock is determined from Zechstein thickness maps from Duin et al. (2006). The Zechstein thickness maps show the thickness of the entire Zechtstein Group. The Zechstein thicknesses are averaged for each field and are especially in the case of the Groningen field averaged over a large area, imposing an uncertainty. The field data content can be found in appendix 1.

Understanding the geological setting and depositional history of the reservoirs named above can be fundamental for understanding the system and necessary to obtain certain reservoir parameters, e.g. maximum burial depth. The geological setting and depositional history of the northern Netherlands are discussed in the 'Geological Framework' section. A theoretical background is provided as well, including a selection of relevant research regarding reservoir compaction and seismic potential.

The reservoir parameters are examined by plotting them against both vertical strain and maximum seismic magnitude and total seismic moment and analyzed by dividing the data in ranges of depletion. The ranges are defined to distinguish between values of a reservoir parameter while simultaneously keeping a reasonable amount of data within each range. In order to summarize the relation between two variables, the type of relation (positive or negative), linearity (linear or non-linear) and strength of the relation is considered. If a (rough) correlation is determined, the suggested trend will be displayed for clarity. This method may provide some insight in the dominant factors increasing strain and/or seismic potential and determines whether a reservoir parameter or characteristic may have some distinguishing capacity for seismicity. In other words, if a visual distinction is seen where a parameter above or below a certain value illustrates a substantial amount of seismic or aseismic fields only ($> 10/68$ fields in this study) it is referred to as 'distinguishing capacity'. Van Eijs et al. (2006) uses this method as well for determining whether a reservoir parameter provides a distinguishing capacity for seismicity by plotting the reservoir parameter and the released seismic energy.

Applying a portion of the field data from table 1, stress-strain curves are constructed representing the relation between stress and strain for 68 examined gas fields. These results are compared with stress-strain curves obtained from recent uniaxial compaction experiments on the Groningen field reservoir rock from Hol et al. (2015). By comparison of both field and laboratory based data, new insights regarding translation between these data can be acquired and general trends can be compared. Thus comparing field data from different fields, with different sized reservoirs, located at different depths and with different degrees of depletion, will promote some understanding of which factors determine compaction, how this compares with lab data and what may trigger seismicity in gas fields. Several hypotheses regarding the factors influencing reservoir compaction and seismic potential will be assessed, based on the results of the field data correlation. As this study includes a large-scale approach it is important to realize that, although 68 gas fields is a substantial amount, the resulting database is limited in terms of statistics.

2.2 Analytical Model for Stress Change in a Reservoir and Caprock

In an attempt to test hypotheses obtained from correlating field data, a simple analytical model is constructed with the purpose of simulating, explaining and predicting the complex physical processes involved in reservoir depletion; promoting stress changes in a reservoir and fault reactivation. Making use of simple generic equations involved in bending due to a vertical force in a fixed beam from Young and Budynas (2002), the behavior of a reservoir and caprock bounded by faults is approached by determining the horizontal stress acting on the edge of the beam, i.e. the fault bounding a reservoir. The geometry considers length, width and thickness and is expanded to a ellipse-shaped geometry, thereby approaching real-life geometries of gas fields in the Netherlands. Assuming similar boundary conditions, individual reservoir parameters can be used as variables and tested on the likelihood of changing the stress state in such a way that the failure envelope will be reached and induced seismicity occurs. A simple analytical model is chosen over finite element modeling, since analytical modeling is a relatively simple and transparent method that may capture and explain the general trends as seen in the correlation of field data and thus the likelihood of induced seismicity to occur. Roest and Kuilman (1994) uses both simple and complex models to simulate induced seismicity near the Eleveld field, whereby both models correlate well. It is thus expected that the simple analytical model proposed in this study will provide a reasonable correlation compared to more complex models. Additionally the data involved in this study may be subjected to a data-limitation problem as described in Roest and Kuilman (1994), where no definite solution is possible due to the relative data limitation and complexity of the problem. Simplification of model components is hence proposed (Roest and Kuilman (1994)).

Table 1: *Reservoir parameters used in field data correlation.*

Reservoir parameter	Symbol	Unit
Structural element location	AP = Ameland Platform, LT = Lauwerszee Trough, GP = Groningen Platform, LSB = Lower Saxony Basin, FP = Friesland Platform, CNB = Central Netherlands Basin	-
Reservoir type	$ROSLU$ = Upper Slochteren Sandstone, $ROSL$ = Slochteren Sandstone, $ROCLT$ = Ten Boer Claystone, RO = Upper Rotliegend Group, DC = Limburg Group, RBM = Main Buntsandstein Subgroup, $KNNS$ = Vlieland Sandstone Formation, ZE = Zechstein Group	-
Maximum burial depth	d_{max}	m
Mean porosity	ϕ	-
Compaction coefficient	C_m	$10^{-5} \cdot 1/bar$
Present depth to reservoir top	d	m
Reservoir thickness	t	m
Reservoir temperature	T	°C
Depth to GWC (gas-water contact)	d_{GWC}	m
Production time	-	$years$
Initial gas pressure	$P_{f(initial)}$	bar
Current gas pressure	$P_{f(current)}$	bar
Surface subsidence	ΔL	cm
Mean overburden density	ρ	kgm^3
Vertical overburden stress on reservoir top	σ_v	MPa
Depletion	ΔP_f	MPa
Vertical effective stress	σ_{veff}	MPa
Type of primary caprock	ZE = Zechstein Group, $RBSH$ = Main Claystone Formation, $RNSOC$ = Sölling Claystone Formation, $KNNC$ = Vlieland Claystone Formation, $ROCLT$ = Ten Boer Claystone	-
Thickness of primary caprock	t_c	m
Seismic (Y/N)	-	-
# of induced earthquakes $\geq$ 1.5	-	-
# of induced earthquakes $\geq$ 3	-	-
Maximum seismic magnitude	M_L	Richter scale
Total seismic moment	M_o	Nm
Earthquake near (± 500 m) fault zone (Y/N)	-	-
Vertical strain	ϵ_v	-
Length field	L	m
Width field	W	m
Volume field	V	m^2
Area field	A	m^3

3 Geological Framework

Understanding the geological setting and depositional history of both reservoirs and caprocks examined in this study is fundamental, since the processes involved may influence the initial reservoir characteristics. It is hence possible that geometrical and petrophysical parameters may be influenced or altered by depositional setting and structurally active episodes. This section therefore discusses the geological framework for mostly the northern Netherlands.

3.1 Depositional Setting and Lithostratigraphy

The 68 onshore gas fields examined in this study consist of similar types of reservoir and caprock, on which this geological framework will focus. The following reservoir types: Upper Slochteren Sandstone (ROSLU), Slochteren Sandstone (ROSL), Ten Boer Claystone (ROCLT), Upper Rotliegend Group (RO), Limburg Group (DC), Main Buntsandstein Subgroup (RBM), Vlieland Sandstone Formation (KNNS), Zechstein Group (ZE), and the following caprock types: Zechstein Group, Main Claystone Formation (RBSH), Sölling Claystone Formation (RNSOC), Vlieland Claystone Formation (KNNC) and Ten Boer Claystone represent the gas fields examined in this study. Except for the Lower Cretaceous Vlieland Formation, all reservoir and caprock types are deposited from the Middle Permian to Early Triassic (Kombrink et al. (2012)). Table 2 illustrates these lithostratigraphic units (Kombrink et al. (2012); NAM (2013)).

Table 2: *Lithostratigraphy of the examined gas fields in the northern Netherlands.*

Period	Age [Ma]	Group	Formation	Member	Code	Role Petroleum System
Early Cretaceous	139-126	Rijnland	Vlieland Claystone		KNNC	Caprock
			Vlieland Sandstone		KNNS	Reservoir
Middle Triassic	247-241	Upper Germanic Trias	Sölling Formation	Claystone	RNSOC	Caprock
Early Triassic	257-247	Lower Germanic Trias	Main Buntsandstein		RBM	Reservoir
			Main Claystone		RBSH	Caprock
Late Permian	260-257	Zechstein			ZE	Caprock/Reservoir
Middle Permian	269-260	Upper Rotliegend	Silverpit	Ten Boer Claystone	ROCLT	Caprock/Reservoir
			Slochteren	Upper Slochteren Sandstone	ROSLU	Reservoir
			Silverpit	Ameland Claystone	ROCLA	Caprock
			Slochteren	Lower Slochteren Sandstone	ROSLL	Reservoir
Early Permian	299-269	Lower Rotliegend				
Late Carboniferous	323-303	Limburg			DC	Reservoir

The Late Carboniferous Limburg Group consists of an alternation of fluvio-deltaic sediments and coals as a part of a regressive mega-trend (Kombrink et al. (2012)). The Saalien unconformity bounds the Carboniferous and Permian sediments and represents an hiatus caused by the Variscan orogeny, creating a depositional relief (Brouwer (1972); Geluk (2007); Kombrink et al. (2012); NAM (2013)). The Early Permian strata are represented by the Lower Rotliegend Group and consist of volcanic and volcanoclastic deposits that are not evidently demonstrated in the Netherlands (Brouwer (1972); Geluk (1999); Geluk (2007); Kombrink et al. (2012)). Hence, the Upper Rotliegend Group is seen as the first post-orogenic deposit in the Netherlands after the Carboniferous Variscan orogeny (Brouwer (1972)). The majority of the reservoirs of the 68 examined onshore gas fields are present in the Upper Rotliegend Group, deposited in the Southern Permian sag Basin. The East-West trending Southern Permian Basin extended from the United Kingdom to Poland between approximately 15-20 °N in an arid environment (Brouwer (1972)). Since the Netherlands was positioned in the northern foreland of the Variscan mountain range during the Variscan orogeny, the Upper Rotliegend Group forms a wedge that is onlapping on the higher located Carboniferous relief in the southeast and thickening towards the northwest, where more accommodation space was available (Geluk (2007); Kombrink et al. (2012); NAM (2013)). The arid aeolian sequences of the Upper Rotliegend Group are alternated with fluvial deposits, grading into finer lake deposits further northwards and alluvial and braided river deposits to the South (NAM (2013)). The Ameland and Ten Boer Claystones consist of silty to shaly lake deposits with intercalated halites due to regional lake highstands and the mixed fluvial and aeolian deposits are both represented by the Lower and Upper Slochteren Sandstone (Kombrink et al. (2012); NAM (2013)). The Upper Rotliegend Group depositional setting as seen in the northern Netherlands coincides with the description of an aeolian depositional environment of Nichols (2009), including a lateral succession of alluvial fan deposits, sand accumulations of aeolian dunes and ephemeral lakes with clay and evaporite minerals. The overlying Zechstein Group consists of cyclic marine evaporite deposits, where the high amount of halite acts as an excellent impermeable caprock for the Upper Rotliegend reservoirs (Kombrink et al. (2012); NAM (2013)). During the Early Triassic, the continuous subsidence of the Southern Permian Basin facilitated an infill of playa shales (Main Claystone Formation) and an overlying alternation of aeolian to fluvial sediments (Main Buntsandstein Formation) and lacustrine shales (Kombrink et al. (2012)). The Sölling unconformity divides the Lower and Upper Germanic Trias Group and the super-imposed Sölling Claystone, which represents an increased marine influence due to the connection with the Tethys ocean (Geluk et al. (2007)). Since none of the 68 examined gas reservoirs are of Jurassic age, the depositional environment of the Jurassic sediments is of less importance in this study. Continuing with the Lower Cretaceous sediments, where the shallow marine and bioturbated

Vlieland Sandstone of the Rijnland Formation represents the base of a transgressional sequence, followed by the fine-grained marine Vlieland Claystone (Kombrink et al. (2012)).

3.2 Structural Setting

The Early Permian was a tectonically stable period with only minor faulting, as seen in both facies and isopach maps, while the Late Permian strata were involved in two tectonic phases; mild East-West extension and uplift and erosion (Gaupp and Okkerman (2011); Geluk (1999); Van Wees et al. (2000)). During the deposition of the Lower Triassic Buntsandstein tectonic quiescence occurred, followed by several tectonic stages (Gaupp and Okkerman (2011)). The first tectonic stage was the Triassic-Middle Jurassic rift resulting in block faulting and rotation, following and reactivating NW-SE trending faults and fault systems that were established during the Paleozoic. During the Late-Jurassic and Early-Cretaceous thermal doming occurred as a consequence of an increased rifting rate associated with the North Sea and Tethys rift systems, which was followed by thermal subsidence and thus a transition from rift to sag phase (Gaupp and Okkerman (2011); Kombrink et al. (2012); Van Wees et al. (2000)). The Late-Jurassic to Early Cretaceous period of intensified rifting is also referred to as Late Kimmerian rifting, from which most structural elements in the Netherlands are inherited (Kombrink et al. (2012)). The Late Cretaceous and Early Tertiary represent a period of uplift and inversion of former extensional faults (Gaupp and Okkerman (2011)). Since not all structural elements in the Netherlands have been inverted (Kombrink et al. (2012)), the structural elements involving reservoirs examined in this study are specified further. The 68 onshore gas field examined in this study are located in the following structural elements: Ameland Platform, Lauwerszee Trough, Groningen Platform, Lower Saxony Basin, Friesland Platform and Central Netherlands Basin, from which only a minority is located in the Lower Saxony Basin and Central Netherlands Basin. The locations of the structural elements from the perspective of the Dutch continental shelf is illustrated in figure 2. The Ameland Platform is a relatively stable block, bounded by faults by the Schill Grund Platform, Friesland Platform and partly the Lauwerszee Trough and passed into the Terschelling Basin, Groningen Platform (where the top Rotliegend is positioned at somewhat shallower depths) and partly the Lauwerszee Trough (Duin et al. (2006); Kombrink et al. (2012)). The WNW-ESE trending Central Netherlands Basin is only represented in this study in the Bergermeer field, where strong N-S inversion is seen as a consequence of the Late Cretaceous Alpine orogeny (Duin et al. (2006); Kombrink et al. (2012); NAM (2013)). The large and stable Friesland Platform is fault-bounded by the Lauwerzee Trough and the Central Netherlands Basin and includes regions where Jurassic sediments are eroded (Duin et al. (2006); Kombrink et al. (2012)). The Groningen Platform was not inverted and tectonically stable since the Late Kimmerian doming and is fault-bounded by the Hantum Fault Zone in the West, separating the Groningen Platform from the Lauwerszee Trough while the succesion is similar (Kombrink et al. (2012); NAM (2013)). The Lauwerszee Trough is bounded on both the northeast and southwestern sides by large fault zones (including the Hantum Fault Zone), which have not been reactivated (Kombrink et al. (2012)). Notable is that the outline of the gas reservoirs in the northern Netherlands, but especially in the Lauwerszee Trough, follows a distinctive NW-SE pattern, similar to the Paleozoic and Triassic-Middle Jurassic reactivated fault systems. Duin et al. (2006) defines the Lower Saxony Basin as distinctive due to the presence of sediments of Late Jurassic to Early Cretaceous age. The basin is inverted and bounded in the northwest by the Friesland and Groningen Platforms and the Lauwerszee Trough (Kombrink et al. (2012)).

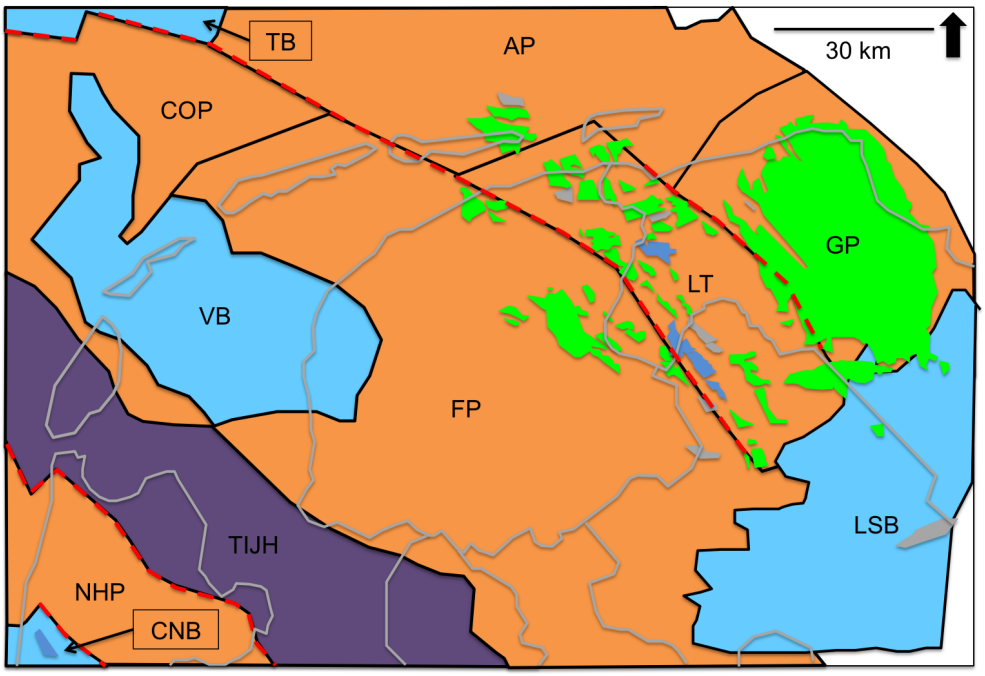

Figure 2: *The structural elements of the Netherlands, formed during the Late Jurassic-Early Cretaceous (adapted from Kombrink et al. (2012)). The gas fields examined in this study are illustrated as well. The red dotted lines represent the locations where the edge of a structural element coincides with a fault. The orange structural elements represent platforms, the blue structural elements represent basins and the purple structural element represents a high. AP = Ameland Platform, LT = Lauwerszee Trough, GP = Groningen Platform, LSB = Lower Saxony Basin, FP = Friesland Platform, CNB = Central Netherlands Basin, TB = Terschelling Basin, COP = Central Offshore Platform, TIJH = Texel-IJsselmeer High, VB = Vlieland Basin and NPH = Noord-Holland Platform.*

3.3 Influence of Depositional and Structural Setting on Petrophysical and Geometrical Parameters

Since both depositional and structural history are influencing the final geometry and petrophysical parameters of a field, differences in fields regarding compaction and seismicity may possibly be related to differences in depositional and structural history. Rotliegend core observations from NAM show different porosities for different depositional settings, where aeolian dunes, fluvial floodplain deposits and wet sandflat deposits have a porosity between 15-25, 5-10 and 3-8 %, respectively. Fluvial deposits generally have a lower porosity than the well sorted aeolian deposits, since fluvial deposits are often intercalated with silty beds. Nichols (2009) illustrates that generally, aeolian dunes generate thicker and more laterally extensive sequences or deposits than fluvial depositional environments. This may imply that gas fields consisting of high porosity reservoirs are also thicker, since they have developed in an aeolian dune depositional environment. Athy (1930) developed an empirical generic law relating the decrease of porosity to depth, later refined by Zoback (2010) as

$$\phi = \phi_0 e^{-C_m \sigma_{veff}} \tag{1}$$

where ϕ is the porosity at a certain depth, ϕ_0 is the initial porosity before burial, Cm is the compaction coefficient and σ_{veff} is the vertical effective stress. The vertical effective stress is defined as

$$\sigma_{veff} = \sigma_v - P_f = \rho g h - P_f \tag{2}$$

where σ_v represents the density times the gravity times the depth ($\rho g h$) and P_f represents the pore fluid pressure (Hantschel and Kauerauf (2009)). Hence compaction coefficient (i.e. the degree of compressibility or inverse stiffness) is dependent on the porosity, depth and density of the overburden. It is important to note that the porosity is altered by the maximum burial depth in geological history, thus relating porosity to structural setting. The depth of the reservoir top is largely influenced by structural history as well, since the current depth of the reservoir top is determined by the amount of burial and inversion in geological history. The different structural elements that are relevant in this study have different geological histories and therefore different maximum burial depths. Verweij et al. (2012) discusses the influence of burial history on fluid pressures in the Dutch subsurface. Large differences in regional burial history yet imply normal fluid pressures in the West Netherlands Basin, Broad Fourteens Basin and the Central Offshore Platform and overpressures in the Terschelling Basin, Step Graben, Dutch Central Graben, Lower Saxony Basin, Schill Grund Platform, Friesland Platform and the

Lauwerszee Trough (Verweij et al. (2012)). Gaupp and Okkerman (2011) state that the present depths of the Rotliegend reservoirs in the northern Netherlands are between 2 and 4.5 km. This depth is taken as the maximum burial depth for the Ameland Platform, Lauwerszee Trough, Groningen Platform and Friesland Platform reservoirs examined in this study, since in these structural elements no major inversion has taken place (Gaupp and Okkerman (2011); Kombrink et al. (2012)). NAM (2013) states that the maximum burial depth for the Groningen Platform is represented by the present depth to reservoir top as well. The Lower Saxony Basin has a different structural history since it was subjected to inversion and therefore the maximum burial depths are also different (Kombrink et al. (2012)). A 3D basin modeling study for the Lower Saxony Basin is done by Bruns et al. (2013), where the maximum burial depths of the Rotliegend, Zechstein and Buntsandstein are 4650, 4450 and 4250 m respectively. The maximum burial depth for the inverted Central Netherlands Basin is 2800 m according to Nelskamp et al. (2008) and this value is used for the only examined gas field in the Central Netherlands Basin, which is the Bergermeer field. Following an average geothermal gradient in the Netherlands of 31°C per kilometer (from www.thermogis.nl), the reservoir temperature is partly dependent on the present depth of the reservoir, and thus dependent on the structural setting. The geometry of fields is partly dependent on depositional setting, since the depositional environment influences the type of sediments that accumulates and therefore the geometry of fields (e.g. fluvial deposits have a different geometry and lateral extension than aeolian deposits). The field geometry is also dependent on structural setting, presuming this factor determines the availability of accommodation space and thus the geometry of accumulated sediments. Tectonics after deposition of a reservoir may alter the field, creating compartments within a field by faulting. Reservoirs that are bounded or intersected by natural faults are generally more prone to induce seismicity, since they contain weak zones along which movement can occur, resulting in the earlier ascription of induced seismicity to fault reactivation (Van Eijs et al. (2006); Mulders (2003); NAM (2013)). Additionally, sealing faults can alter the reservoir pressure and gas-water contact between neighboring fields or between field compartments. Kombrink et al. (2012) states for example that sealing faults in the Hantum Fault Zone cause the gas-water contact to be different and independent in the Groningen Platform with respect to the Lauwerszee Trough.

4 Literature Background

This section describes the theoretical background, thereby relating the reservoir parameters examined in this study to the mechanisms of reservoir compaction, subsidence and induced seismicity from literature. In order to compare field data to the theoretical background hypotheses are formulated.

4.1 Relating Reservoir Parameters to Compaction and Seismicity

A distinction can be made between volumetric change in a reservoir, i.e. compaction, occurring during depletion and during burial. Compaction during depletion occurs in in relatively weak formations when the overburden pressure stays constant while the pore fluid pressure decreases during the production of a field (Doornhof et al. (2006); Zoback (2010)). Rearrangement of grains during burial, increasing density, is referred to as mechanical compaction, while cementation relates to chemical compaction (Hantschel and Kauerauf (2009)). Additionally Ramm (1992) discusses several porosity-reducing or compaction mechanisms, where between a depth of 0 to 2.5/3 km mechanical compaction is the primary mechanism and from a depth of 2.5/3 km chemical compaction is controlling.

Numerous authors have described the relation between initial porosity, i.e. porosity prior to the start of production, and compaction. A general relation is stated where compaction or strain during depletion of a reservoir significantly increases with increasing initial porosity (NAM (2013); Trautwein and Huenges (2005)). Porosity is observed to be decreasing with increasing depth (Athy (1930); Ramm (1992)). Fisher et al. (2003) states that the rheology and style of deformation of a sandstone are largely influenced by cementation of quartz. Quartz cementation is temperature-dependent and causes a decrease in porosity, thereby increasing the strength of the rock with an increase in temperature (Fisher et al. (2003); Walderhaug (1996)). Below a temperature of 90 °C quartz cementation is not substantial (Fisher et al. (2003); Walderhaug (1996)). Zoback (2010) describes that a higher temperature creates expansion of the pore fluids, thus increasing the pore fluid pressure in theory. Generally an increase in temperature is accompanied by an increase in depth, since heat is generated by crystalline basement at depth due to radioactive decay (Zoback (2010)). However, the time-scale on which heating occurs is much longer compared to the time-scale in which overpressures are generated (Zoback (2010)).

The majority of research is focused on small-scale geometry of grains and pores, while this study emphasizes on larger scale reservoir geometry. Actual site-specific forecasts of behavior and stress changes in gas fields during depletion is described in Orlic (2013). Orlic (2013) performed geomechanical simulations to calculate the amount of stress disturbance, dependent on reservoir geometry, structural setting and reservoir characteristics, during depletion around 4 gas fields that were analyzed for the purpose of CO_2 storage. The areal extent of stress disturbance or change was observed to be small and only continuing a couple of kilometers when considering small, highly compartmentalized gas fields (Orlic (2013)). Holt et al. (2004) describes the relation between field geometry and stiffness contrast with the amount of compaction. On the basis of the ratio between thickness and length of a field the amount of compaction is estimated, whereby an increase in compaction and reservoir bending is seen when the thickness/length ratio of a reservoir, i.e. aspect ratio, is decreasing (Holt et al. (2004)). A reduction in compaction is observed with an increase in stiffness contrast between the particular field and enclosing lithostratigraphic units (Holt et al. (2004)). Additionally, Chilingarian et al. (1995) states that substantial compaction is subjected to cemented gas reservoirs when reservoirs with a significant area and thickness (>50 m) are considered. Geertsma (1973) allocates 3 main factors needed for significant compaction to occur; the amount of pressure reduction, the compaction coefficient and the height of the depleted reservoir interval. The above implies that geometry of a reservoir may be a crucial factor for the determination of reservoir compaction and subsequent increase in seismic potential.

The uniaxial compaction coefficient is a material property that gives the degree of compressibility, depending on the contact area of grains and thus on the amount of cementation, the type of rock, the burial history and porosity (Geertsma (1973); NAM (2013)). It is defined as

$$Cm = \frac{1}{E}\frac{(1+v)(1-2v)}{1-v} \tag{3}$$

where Cm is the uniaxial compaction coefficient $[10^{-5}bar^{-1}]$, E is the Young's modulus and v is Poisson's ratio (NAM (2013)). Generally the compaction coefficient ranges from approximately 0.3 (compact rock) to 20-40 (very loose rock, e.g. loose sands) $\cdot 10^{-5}bar^{-1}$ (Geertsma (1973)).

Focussing on the Groningen gas field only, Bourne et al. (2014) illustrates the distribution of reservoir parameters within this field. It can remarkably be observed that in the region within the Groningen field where most induced seismic events have occurred, the reservoir compressibility and reservoir compaction are clearly high compared to the less seismic parts of the field. The net reservoir thickness is significantly higher and the fault density significantly lower in the field region where the highest amount of induced seismicity occurred, relative to the regions with lower seismicity. This low-seismicity region is positioned mainly in the southeast part of the field, having a relatively low net reservoir thickness, low compaction, low compressibility and high fault density. Pressure depletion is observed to be rather continuous throughout the entire field. A study of the Eleveld field by Roest and Kuilman (1994) provides evidence of induced seismicity related to field geometry relative to faults present in and bounding the reservoir, whereby the amount and direction of fault dip

influences slip locally. Local fault reactivation due to reservoir depletion and differential compaction was defined to most likely occur along normal faults with a subvertical orientation (Roest and Kuilman (1994)).

Surface subsidence and stress change in and around a reservoir can occur during depletion, thereby increasing the possibility of fault reactivation (Zoback (2010)). Positive effects can also be involved in depletion, since compaction drive can be an important mechanism for the enhancement of hydrocarbon recovery (Zoback (2010)).

4.2 Relating Compaction to Surface Subsidence

Doornhof et al. (2006) describes the relation between compaction in a reservoir and surface subsidence, where surface subsidence is essential to estimate reservoir compaction during depletion since it is complicated to observe reservoir compaction per se. The volumetric change in the reservoir is passed on to the surface and may cause a decline in surface level by the creation of a subsidence bowl when the pore fluid pressure in a reservoir is significantly lowered, the overburden is able to deform downward and the reservoir rocks are compactable to a certain extend (Allen et al. (1971); Doornhof et al. (2006)). The deformation due to reservoir depletion is, considering the large lateral extent compared to the vertical extent, or thickness of the reservoir, mostly in the vertical direction (Geertsma (1973)). The lateral spreading of the subsidence bowl is depending on both the overburden material properties and reservoir depth (Doornhof et al. (2006)). The shape of the subsidence bowl is mostly larger than the area of the compacting reservoir and fairly symmetrical, since during the transmission of each compacting element to the surface variance is partly eliminated (Doornhof et al. (2006)). Doornhof et al. (2006) states that compaction in a reservoir is equal to the surface subsidence when no expansion of the overburden is present, also referred to as time-dependent creep. Time-dependent creep may cause an increase in compaction and strain, even after the production of a field has stopped (Hettema et al. (2002); NAM (2010); Schutjens (1991)).

Hettema et al. (2002) describes the delay in translation between depletion of a field and the subsidence at the surface, where the relation between these parameters is non-linear. In later stages of reservoir depletion this relation becomes more linear, similar to prognoses made on the base of linear elasticity. The shift between beginning of reservoir depletion and the beginning of subsidence is called the subsidence-depletion delay effect, which is 3.2 years for the Groningen gas field (Hettema et al. (2002)). The subsidence-depletion delay effect is assigned to overpressures, pore pressure diffusion and other compaction mechanisms such as creep, the relation between compaction to loading rates that are geological or production-induced and high initial stiffness of the rock (Hettema et al. (2002)). The study therefore implies that the currently measured subsidence at the surface above a field may not be the final subsidence generated by a certain depletion.

Hettema et al. (2000) discusses the differences in expected amount of compaction for depleting gas fields in laboratory uniaxial experiments (i.e. no lateral strain; only vertical compaction is allowed) and in the field. For the Groningen gas field the predicted compaction and subsidence from laboratory experiments is larger than the actual compaction and subsidence as measured in the field itself. This suggests a higher stress path, i.e. change in stress during depletion, in laboratory experiments than measured in the field (Hettema et al. (2000); Zoback (2010)). Two explanations for these observations are proposed. The first explanation implies that the stress path of the Groningen field may have low values compared to laboratory experiments when frictional sliding across normal faults is a controlling factor in the amount of horizontal field stress present in the field. Additionally, the low stress path of the Groningen gas field may be caused by the overlying Zechstein caprock (mainly halite) that balances the change in stress during depletion due to its ductile behavior (Breckels and Van Eekelen (1982); Hettema et al. (2000)). Similarly, ductile behavior of halite may cause the subsidence as seen at the surface to be smaller than the actual compaction in the subsurface (NAM (2010); NAM (2013)). Marketos et al. (2015) asses the role of evaporite above a depleting reservoir, concluding that a larger surface subsidence is predicted as the evaporite layer is smaller. Also, ductile evaporites may induce time-dependent creep (Marketos et al. (2015); NAM (2010); NAM (2013)). These hypotheses are further investigated in the discussion of the field data results, focussing on the thickness of the Zechstein caprock and surface subsidence of the 68 onshore reservoirs in this study.

4.3 Relating Compaction to Seismicity

The relation between depletion in a reservoir, reservoir compaction and hence induced seismicity is briefly described in the 'Introduction' section, whereas this section continues in more detail. Anthropogenic seismicity, i.e. induced seismicity, can be generated by both fluid injection and depletion (McGarr et al. (2002); Segall (1992)). In the case of fluid injection in a permeable layer, the increase in pore fluid pressure may generate induced seismicity due to the transmission of the increase in pore fluid pressure to a fault, thereby lowering the fault's normal stress and approaching the Coulomb failure criterion (Frohlich (2012); McGarr et al. (2002); McGarr (2014); Zoback (2010)). The in-situ stress field and orientation of the fault are important factors for determining whether induced seismicity occurs (Frohlich (2012); Roest and Kuilman (1994)). While an increase in pore fluid pressure provides the Mohr circle of a specific rock to approach the Coulomb failure criterion, fluid production, i.e. pore pressure decrease, in theory provides a larger distance from the failure criterion and thus lower the potential for induced seismicity (Segall (1989); Zoback (2010)). The mechanism for anthropogenic seismicity due to depletion is indirectly linked to the decrease in pore fluid pressure, which causes deformation, in this

case: contraction or compaction, of the reservoir rocks (Roest and Kuilman (1994); Segall (1989); Segall (1992)). Since high porosity and permeablility reservoir rocks are subjected to a higher decrease in pore pressure compared to low porosity and permeability rocks that enclose the reservoir, differential compaction occurs and stress is hence generated (Holt et al. (2004); Mulders (2003); Segall (1989); Segall (1992)). During production of a reservoir, the horizontal stress in a reservoir generally decreases, while the vertical stress stays constant under the condition that length versus thickness ratio of the reservoir is equal to 10:1 (Segall and Fitzgerald (1998); Zoback (2010)). The decrease in horizontal stress may promote the Mohr circle of a particular rock to reach the failure criterion, thereby inducing seismicity (McGarr et al. (2002)). Concluding, failure can occur due to two different mechanisms, namely 1) Lowering the effective normal stress (σ_n) by increasing the pore fluid pressure and 2) Increasing the shear stress (τ) due to a lowering of the horizontal stress (σ_3), for the injection and depletion scenario, respectively (McGarr et al. (2002)). Bourne et al. (2014) observes a relation between induced seismic events in the Groningen field with a magnitude larger than 1.5 on the Richter scale and the degree of compaction in the reservoir, whereby 90 % of the induced seismic events occur in a part of the reservoir with a minimum compaction of 18 cm. This observation thus illustrates the large influence of compaction, generated by reservoir depletion, on induced seismicity (Bourne et al. (2014)).

4.4 Hypotheses Summary

In order to maintain clarity the hypotheses for field behavior during depletion, as inferred from the theoretical background, are listed below. These hypotheses will be examined in the following sections.

Table 3: *A summary of the hypotheses examined in this study.*

Main Topic	Sub Topic	Hypothesis
Compaction Seismicity		Fields that accommodate more compaction have a higher total seismic moment; An increase in compaction will increase total seismic moment.
Depletion	Compaction Seismicity	An increase in depletion will both increase reservoir compaction and seismicity occurrence.
	Depth	Depletion increases with depth.
Porosity	Compaction Seismicity	An increase in mean field porosity will increase compaction and seismicity occurrence.
	(Burial) depth	Porosity decreases with increasing (burial) depth.
Temperature	Compaction Seismicity	An increase in reservoir temperature will decrease compaction and seismicity.
	Porosity	An increase in reservoir temperature decreases porosity due to quartz cementation from 90 °C.
Current production time	Depletion Compaction	An increase of a fields production time increases depletion and compaction, thereby increasing the seismic potential.
	Seismicity	Seismicity occurrence and magnitude increase over time.
Depth	Compaction Seismicity	Reservoirs at greater depths are already compacted and will not compact significantly during depletion, resulting in a low seismic potential.
Geometry	Length/Width	An increase in length-to-width ratio of a field decreases compaction and seismic potential.
	Thickness	An increase in reservoir thickness will both increase reservoir compaction and seismicity occurrence.
	Length/Thickness	An increase in length-to-thickness ratio of a field decreases compaction and seismic potential.
	Length/Depth	Length-to-depth ratio has small values for compaction initially, continuing with a steep increase in compaction and seismic potential.
	Width	An increase in field width will both increase reservoir compaction and seismicity occurrence.
	Width/Thickness	An increase in width-to-thickness ratio gives a decrease in vertical strain and seismicity.
	Area Volume	A large field area and volume will increase reservoir compaction and seismicity occurrence.
	Area/Thickness	An increase in A/t ratio gives a decrease in reservoir compaction and seismic potential.
Vertical effective stress	Compaction Seismicity	An increase in current vertical effective stress on the reservoir top increases compaction and total seismic moment.
Compaction coefficient	Compaction Seismicity	An increasing compaction coefficient will both increase reservoir compaction and seismicity occurrence.
Zechstein thickness	Compaction Seismicity	An increase in Zechstein thickness decreases surface subsidence and vertical strain and increases total seismic moment.

5 Results & Discussion - Correlation of Reservoir Parameters

The correlation between several gas field characteristics (i.e. parameters) and the occurrence of seismicity in gas fields is examined in this section, where parameters may provide a distinguishing capacity for the occurrence of seismicity. Plotting several reservoir parameters against vertical strain, maximum seismic magnitude and total seismic moment will provide some understanding about which gas field characteristics may influence and possibly increase or decrease the seismic potential in a depleting reservoir.

5.1 Correlation of Vertical Strain, Maximum Seismic Magnitude & Total Seismic Moment

Understanding vertical strain, maximum seismic magnitude and total seismic moment is essential considering the reservoir parameters or characteristics are plotted against these field data. Vertical strain is determined as the change in reservoir thickness divided by the initial reservoir thickness, or

$$\varepsilon = \frac{\Delta L}{L_0} = \frac{L_0 - L_1}{L_0} \tag{4}$$

where L_0 is defined as the initial reservoir thickness, L_1 is the initial reservoir thickness minus the surface subsidence (i.e. the thickness of the compacted reservoir). Surface subsidence is adopted positive in this equation. Lateral movement of the overburden and the occurrence of Zechstein salt as a caprock may cause disturbance in the translation from compaction in a subsurface reservoir to surface subsidence due to the lowering of the stress path (Doornhof et al. (2006); Hettema et al. (2000)). Ergo, taking surface subsidence as a direct measurement of compaction in a reservoir is a substantial but inevitable assumption. Both stress path lowering and lateral movement of the overburden decrease the translated surface subsidence compared to compaction in the reservoir and thus it is likely that the actual compaction in the reservoir is slightly larger than assumed in this study. Nevertheless, since reservoir deformation occurs mostly vertically, vertical strain is assumed to be a good representation of deformation or compaction in a reservoir (Geertsma (1973)).

Both seismic magnitude and seismic moment are determined in this study and related by the following equation

$$M_o = 10^{(\frac{3}{2} \cdot M_L) + 16.1} \cdot 10^{-7} \tag{5}$$

where M_o and M_L represent the seismic moment [Nm] and seismic magnitude [Richter scale], respectively (Abdulaziz (2014); Kanamori (1983); Tipler (1995)). Since M_o and M_L are related by a logarithmic function it is expected that only a modest difference between maximum seismic magnitude and total seismic moment of individual gas fields exists, as the total seismic moment is predominantly defined by the largest magnitude earthquake. For example, two induced seismic events have occurred in the Appelscha field with magnitudes of 1.7 and 2.3 on the Richter scale, each producing a seismic moment of $4.5 \cdot 10^{11}$ and $3.5 \cdot 10^{12}$ Nm, respectively. The largest magnitude earthquake (with a seismic moment of $3.5 \cdot 10^{12}$ Nm) thus mostly defines the *total* seismic moment of $4 \cdot 10^{12}$. Naturally, this relation will not apply if numerous induced seismic events of similar magnitudes have occurred; the maximum seismic magnitude will then be significantly lower than the *total* seismic moment. From figure 3 it can be observed that the relation between maximum seismic magnitude and total seismic moment is linear. Additionally, several gas fields have only produced one induced seismic event resulting in a perfectly linear relation between maximum seismic magnitude and total seismic moment. This perfectly linear relation only applies for low magnitude earthquakes prior to a magnitude of 1.5 on the Richter scale. Hence, the interpretation is made that the total seismic moment is mostly defined by the maximum seismic magnitude and plotting reservoir parameters will have similar results for both maximum seismic magnitude and total seismic moment. Nonetheless all examined parameters are plotted against total seismic moment, thereby representing the total released seismic energy. Figures illustrating the reservoir parameters plotted against maximum seismic magnitude can be found in appendix 2.

It is essential to compare field data with similar magnitudes of gas field depletion, i.e. change in pore fluid pressure, since fields that have been depleted only a minor amount will behave different than fields that have been depleted severely. Considering reservoir parameters are plotted against vertical strain, maximum seismic magnitude and total seismic moment, it is fundamental to define the relation between vertical strain and seismicity from field data. Hereby the hypothesis is that *fields which accommodate more compaction generate larger stress changes in and around the reservoir, thus increasing the seismic potential* (Segall (1989); Segall (1992)). Figure 4 illustrates the total seismic moment versus the vertical strain, divided into pore pressure intervals of 0.1-10, 10-20, 20-30 and 30-48 MPa. Using these intervals a reasonable amount of data remains to describe a possible relation per interval. The dataset (68 gas fields) is however still limited. The vertical strain values range from $6.90 \cdot 10^{-5}$ to $3.13 \cdot 10^{-3}$ (Assen and Ameland-Oost fields, respectively) and the total seismic moment and maximum seismic magnitude values from zero to $1.00 \cdot 10^{16}$ Nm or 3.6 on the Richter scale (Groningen Gas Field). Five gas fields are removed from the plot, namely the fields that have a pore pressure depletion of zero (Ameland-Noord, Lauwersoog-C and Vierhuizen (Oost)) and the Tietjerksteradeel fields. The Tietjerksteradeel fields consist of reservoirs located in the Upper Rotliegend Group (RO) and in the Vlieland Formation (KNNS), whereby the Tietjerksteradeel KNNS field is positioned above the Tietjerksteradeel RO field. The degree of depletion is similar

for both fields, i.e. 23.7 and 20.1 MPa for the Tietjerksteradeel RO and KNNS fields, respectively. Consequently it is impossible to determine whether the vertical strain, defined by surface subsidence, is generated by the production of the Tietjerksteradeel RO or KNNS field.

Trends and linearity are difficult to distinguish in figure 4. Fields with larger vertical strains roughly appear to have a larger total induced seismic moment. A very large vertical strain with relatively low induced seismicity can be seen in the Ameland-Oost field (vertical strain = 0.00313, total seismic magnitude = $1.26 \cdot 10^{12}$). The large vertical strain in this field may be caused since this field is both largely depleted (ΔP_f = 47 MPa) and overpressured. Since both seismic and aseismic fields occur in the complete vertical strain range except for the Ameland-Oost and Groningen fields (total seismic moment of $1 \cdot 10^{16}$), vertical strain can be interpreted to have no distinguishing capacity for the occurrence of seismicity. The lack of distinguishing capacity and the relatively inconclusive trend can be explained as possibly other parameters are involved, such as reservoir porosity or field geometry. Alternatively, inaccurate surface subsidence and thus vertical strain data may lead to a possible misfit, which can be improved when new InSAR data is provided.

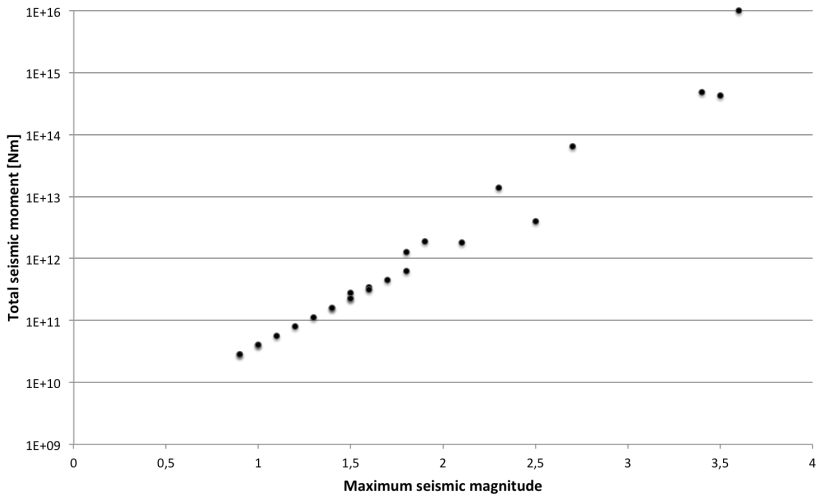

Figure 3: *Total seismic moment versus maximum seismic magnitude for 25 seismic onshore gas fields.*

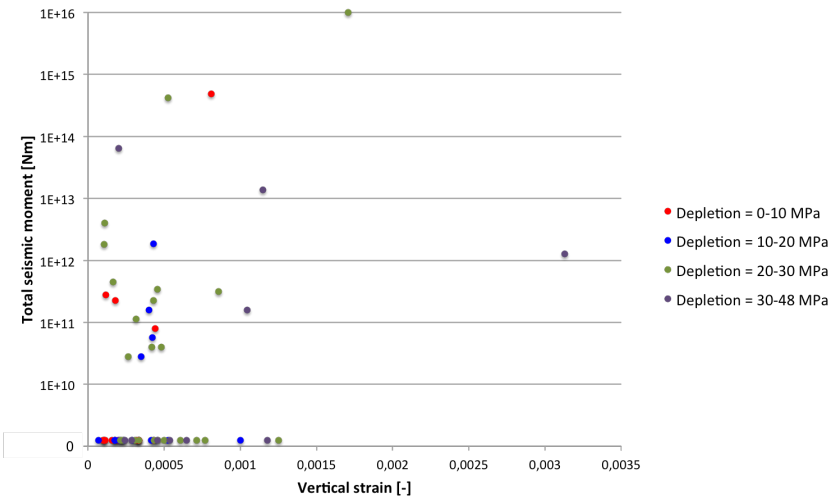

Figure 4: *Total seismic moment versus vertical strain for 63 onshore gas fields.*

5.2 Correlation of Depletion, Compaction & Seismicity

This section examines the relation between depletion, vertical strain and total seismic moment, since all reservoir parameters are subdivided per depletion range. The hypothesis from theory is that *an increase in depletion, i.e. an increase in the change in pore fluid pressure during production, will both increase reservoir compaction and the potential for induced seismicity.*

Figure 5 illustrates vertical strain versus the total current change in pore fluid pressure (ΔP_f) per field, thereby displaying the dependence of vertical strain or compaction on depletion for 63 onshore gas fields. Change in pore fluid

pressure ranges from 0.4 (Ameland-Noord, Lauwersoog-C, Vierhuizen-Oost and Tietjerksteradeel fields filtered out of this figure) to 47.3 MPa (Anjum field). A weak relation can be observed, showing larger vertical strains at a depletion increase, i.e. a large change in pore fluid pressure. From a ΔP_f of 35 MPa a positive linear relation is observed, not taking the overpressured Ameland-Oost field into account (vertical strain = $3.13 \cdot 10^{-3}$). Additionally low vertical strain values (<0.0005) can be observed at relatively high ΔP_f (>20 MPa), illustrating that the amount of vertical strain can not be related solely on the degree of depletion.

The dependence of ΔP_f on total seismic moment for 65 fields is illustrated in figure 6, to determine the general relation and distinguishing capacity for the change in pore fluid pressure regarding seismicity. It is expected that with a higher depletion and thus a higher ΔP_f the maximum seismic magnitude increases. However, due to scattering of data this relation can not be observed. Within a ΔP_f range of 14.5-35.2 MPa a rough trend may be visible, but no clear relation can be seen. The highest seismic magnitudes are clustered around a ΔP_f of 14.5-35.2. Since seismicity occurs at all ΔP_f values, no distinguishing capacity for this parameter can be observed.

The Anjum and Roswinkel fields show notable behavior, not conform hypothesis. The Anjum field is severely depleted (47.3 MPa) but no induced seismicity occurred and the Roswinkel field is only depleted with a minor amount (4.1 MPa), but has a very large total seismic moment of $4.86 \cdot 10^{14}$ Nm. It can be interpreted that other parameters, such as geometry or compaction coefficient are needed to explain these results. Another clarification could be that fields that are currently non-seismic, may generate induced seismicity in the future, which could be possible in the Anjum field. However, this is not very likely considering the very large depletion and relatively large production time of 18 years until present. Hence, multiple parameters apart from depletion are interpreted to be essential for seismicity to occur.

Due to the increasing overburden pressure at depth it is expected that the initial reservoir pressure, i.e. initial pore fluid pressure, is increasing with depth as well. This increases production rates at depth, resulting in *a possible increase in depletion or change in pore fluid pressure with depth.* In order to examine this hypothesis figure 7 illustrates the relation between depth and initial pressure and change in pore fluid pressure during depletion for 65 onshore gas fields. An increase in initial gas pressure with depth can be generally observed. The general hydrostatic pressure gradient of 0.01 MPa/m for fresh water is also plotted in this figure, which is the pressure exerted by a water column continuing towards the surface (Hantschel and Kauerauf (2009), Schlumberger Oilfield Review). However, the slope of the hydrostatic pressure gradient can be influenced by the formation water's salinity. The observation is that initial gas pressure shows linear behavior, but is positioned above the hydrostatic pressure gradient by approximately 5 MPa. Allowing some variability in pressure, it is more likely that the salinity of the formation waters in the northern Netherlands implicate an actual steeper slope of the hydrostatic pressure gradient rather than most of the gas fields illustrated being overpressured. In this case, the known overpressured Ameland-Oost field for example, having a initial pressure of 570 bar and depth of 3300 m, remains overpressured. Verweij et al. (2012) states that fields in the Friesland Platform and Lauwerszee Trough are indeed overpressured. It is thus interpreted that most likely a combination of actually overpressured fields and a difference in slope due to salinity occurs. Additionally a general increase in ΔP_f with increasing depth can be observed, especially looking from a ΔP_f of 20 MPa. The change in pore fluid pressure depends on multiple factors, such as the duration of production, which possibly explains several low ΔP_f values at a large depth. Generally it can be interpreted that both initial gas pressure and ΔP_f increase with depth, which is possibly due to larger production rates at a larger initial gas pressure at depth.

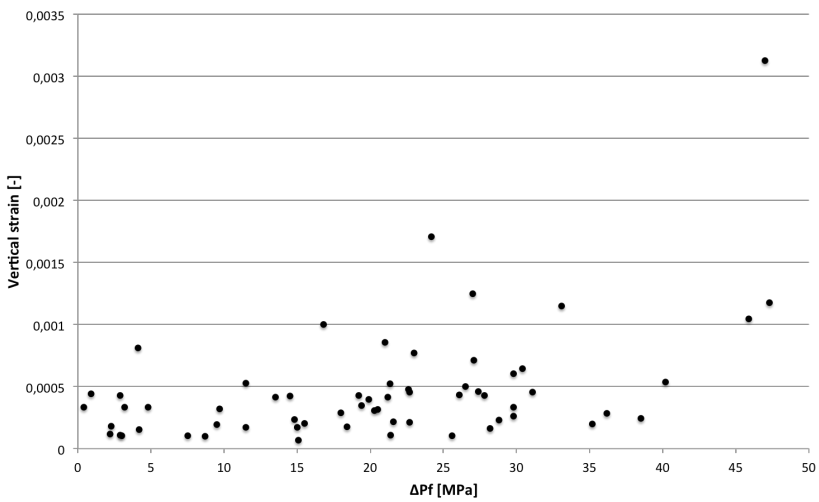

Figure 5: *Vertical strain versus ΔP_f for 63 onshore gas fields.*

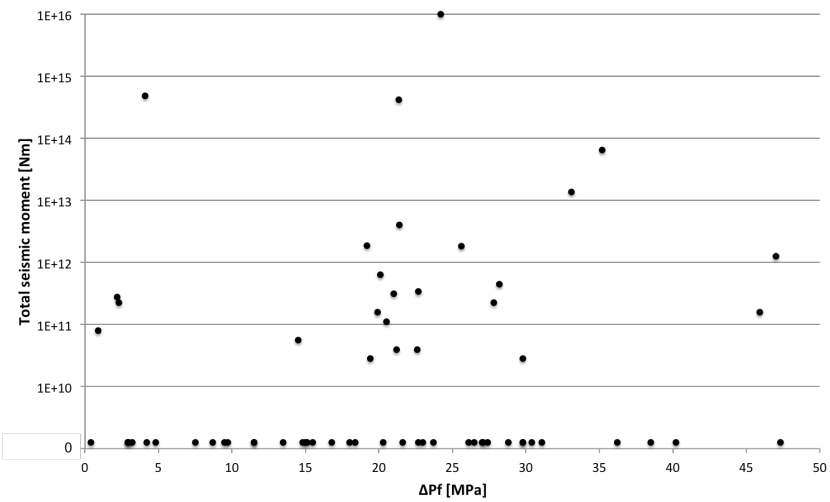

Figure 6: *Total seismic moment versus ΔP_f for 65 onshore gas fields.*

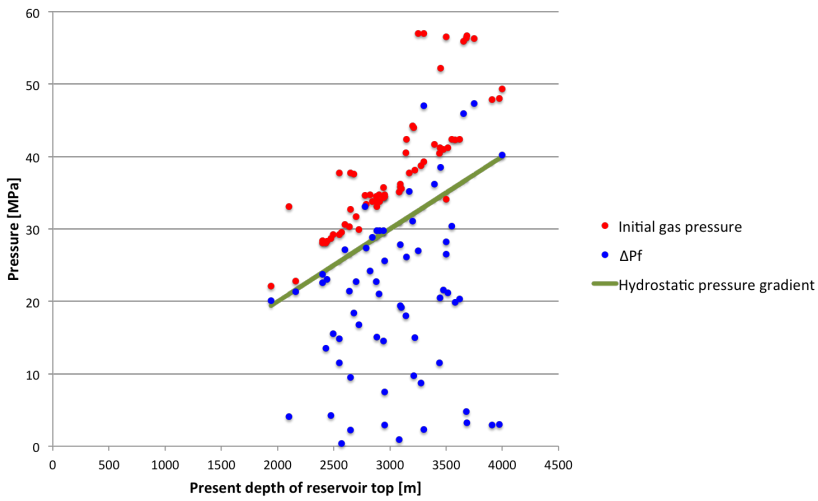

Figure 7: *Initial gas pressure and ΔP_f versus depth for 65 onshore gas fields. The general hydrostatic pressure gradient of 0.01 MPa/m for fresh water is also plotted in this figure (Schlumberger Oilfield Glossary).*

5.3 Correlation of Porosity, Compaction & Seismicity

From theory relating porosity prior to production to the amount of compaction and seismicity, it is expected that *high porosity gas fields can accommodate more compaction and strain, thereby increasing the seismic potential.* Figure 8 illustrates the relation between vertical strain that has been generated during the production of a field and mean reservoir porosity, subdivided by amount of depletion in a field with pore pressure decline intervals of 0.1-10, 10-20, 20-30 and 30-48 MPa. The mean porosities range from 9.10 (Kielwindeweer field) to 22.33 % (Bergermeer field). It is clearly visible that the outlier regarding vertical strain is again the overpressured Ameland-Oost field.

A weak trend can be observed where fields with larger mean porosities appear to accommodate more compaction. Around a porosity of 15 % relatively small strains occur, where between a porosity of 9.10-14.5 and 15.5-22.33% strains increase with increasing porosities. Most examined fields have a porosity around 15 %. A relation disconform hypothesis can roughly be observed in the depletion range of 20-30 MPa, yet this is also the depletion range in which most investigated fields occur (24 of the 63 gas fields). Apart from the Ameland-Oost field, three fields with a relatively small mean porosity and large vertical strain can be seen (Ameland-Westgat, Annerveen and Een, with respective porosity and strain values of 11.5 % and $1.25 \cdot 10^{-3}$, 11.7 % and $1.15 \cdot 10^{-3}$ and 10.2 % and $1.00 \cdot 10^{-3}$). These anomalies can be interpreted to be possibly influenced by other parameters. For the Ameland-Westgat field the relatively high strain at relatively low porosity can possibly be explained considering this field, just as the Ameland-Oost field, is severely overpressured. Furthermore, the Annerveen field is a very large field with a distinctive geometry compared to other, smaller, fields and this could be influencing the strain results. The low reservoir thickness (10 m) of the Een field may explain the relatively large vertical strains. Alternatively, the relatively low porosity-high vertical strain fields could be explained by inaccurate strain data.

Figure 9 illustrates the relation between total seismic moment and mean porosity, again subdivided into ΔP_f intervals of 0.1-10, 10-20, 20-30 and 30-48 MPa for 65 onshore gas fields. The Tietjerksteradeel RO and KNNS fields are both included in the seismicity analysis, since only one induced seismic event has occurred in the KNNS field. Notable is the observation that the three fields with the highest total seismic moment and maximum seismic magnitude, namely the Bergermeer, Roswinkel and Groningen gas fields, also have relatively high mean porosities of 22.33, 20 and 19 %, respectively. A rough linear trend can be observed where porosity increases with increasing seismic magnitudes. Severely depleted fields, in the range of 20-30 and 30-48 MPa, show a relatively steep trend, where at relatively low porosities the total seismic moment largely increases with a small increase in porosity. Within a depletion range of 30-48 MPa substantial total seismic moment (between $1 \cdot 10^{12}$-$1 \cdot 10^{14}$ Nm) can be found at low porosities (<13.2 %). Seismicity in a low depletion interval (ΔP_f = 0.1-10 MPa) can only be observed at porosities >15 %, from which can be interpreted that a higher porosity is needed to induce seismicity at a low level of depletion. Ergo, the general interpretation is that high seismicity may occur at low porosities if substantial depletion of a field occurs and high seismicity may occur at low depletion intervals if the mean porosity of a field is substantially high. Additionally, substantially large total seismic moments and maximum seismic magnitudes, of 3.4, 3.5 and 3.6 for the Roswinkel, Bergermeer and Groningen field can only occur from a porosity of 19 %. The Roswinkel field has a relatively large total seismic moment considering only a small depletion of 4.1 MPa has occurred. It could therefore be interpreted that apart from the large mean porosity of this field (20 %) also other parameters are involved, such as the compaction coefficient that is unusually large. Since both seismic and aseismic fields occur in the complete porosity range, porosity can be interpreted to have no further distinguishing capacity for the occurrence of seismicity and seismicity cannot be distinguished solely on the basis of porosity. Figures that contain illustrations regarding mean porosity versus maximum seismic magnitude, clustered per seismic magnitude (Richter scale) and per porosity range can be found in appendix 3.

As Athy (1930) describes a generic law relating porosity to depth, in which a decrease in porosity occurs while increasing depth during burial, this relation is expected to be seen in the field data as well. Figure 10 illustrates the mean porosity versus both the present depth and maximum burial depth of the reservoir top for 68 onshore gas fields. Computing porosity against maximum burial depth gives the most accurate result, considering porosity is determined by the maximum depth at which the reservoir has been exposed Fisher et al. (1999). Yet, for most reservoirs the maximum burial depth is equal to the present depth of reservoir top. Additionally for structural elements where maximum burial depth is diverging from the present depth the maximum burial depths are determined from literature and thus may not be representing the actual burial depth of the particular reservoir. Using the maximum burial depth or the present depth of the reservoir top alone imposes an uncertainty, hence both depths are illustrated in figure 10. From this figure it can be observed that no evident relation can be found that may prove the hypothesis. Possibly a very weak trend can be observed where porosity is decreasing with increasing depth. A possible explanation for the ambiguous results is that mean porosities from fields are used, where consequently sparse sampling density and non-homogeneous reservoirs contribute to porosities that may not represent reality. Alternatively, the mean porosities taken from several wells within each field may not represent the initial porosity before production of a field, since some wells were drilled while the field was already in production.

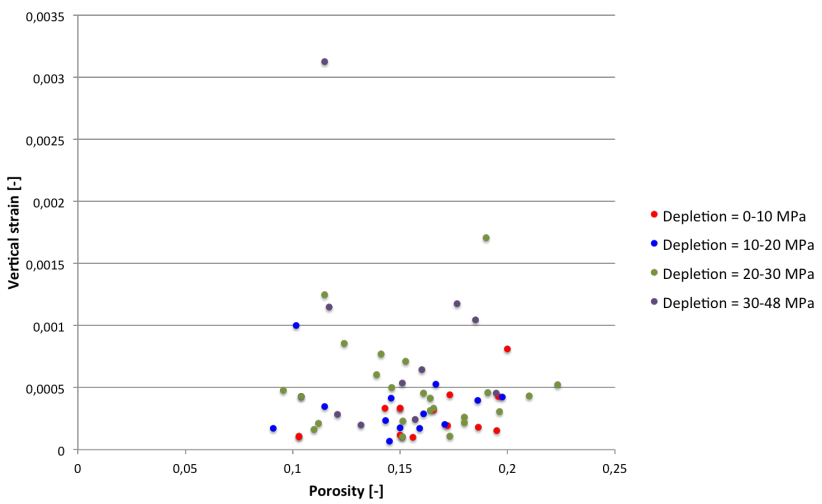

Figure 8: *Vertical strain versus mean porosity for 63 onshore gas fields.*

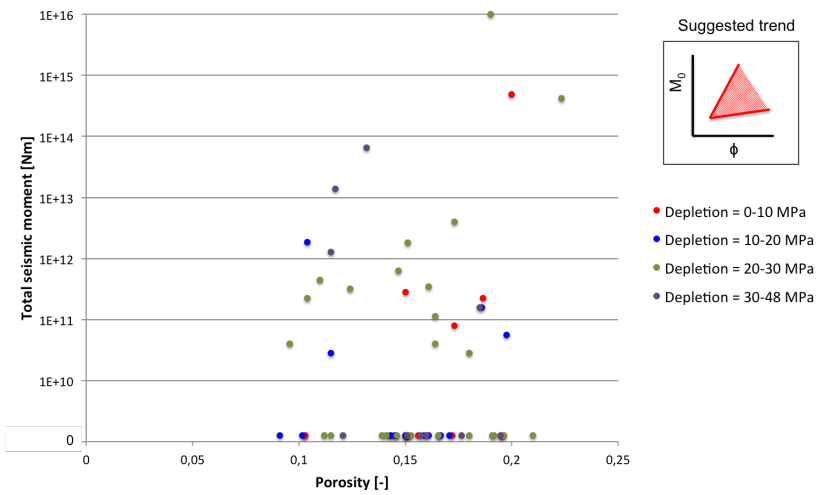

Figure 9: *Total seismic moment versus mean porosity for 65 onshore gas fields.*

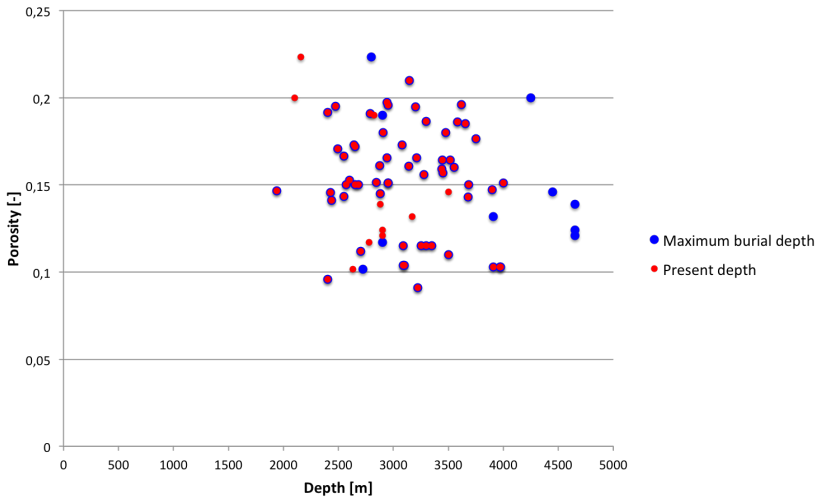

Figure 10: *Mean porosity versus depth of reservoir top for 68 onshore gas fields, including both the present depth and maximum burial depth in geological history.*

5.4 Correlation of Reservoir Temperature, Compaction & Seismicity

Research by Fisher et al. (2003) and Walderhaug (1996) describes higher rock strengths at higher temperatures. It is thus expected that failure occurs at lower rock strengths and *an increase in compaction and induced seismicity will most likely be seen in reservoirs that are at lower temperatures.* Reservoir temperature is determined from the ThermoGIS Expert tool (TNO) that illustrates a temperature model of the Netherlands. The method for this temperature model is described by Bonté et al. (2012) and includes thermal-tectonic forward modeling calibrated with reservoir temperature values from corrected BHT measurements (Bottom Hole Temperature, margin of error of approximately $5 - 10\,^{\circ}$C) and DSTs (Drill Stem Tests, margin of error of approximately $5\,^{\circ}$C).

Figure 11 illustrates the relation between vertical strain generated during the production of a field and reservoir temperature, subdivided by amount of depletion in a field with pore pressure decline intervals of 0.1-10, 10-20, 20-30 and 30-48 MPa. The reservoir temperature in the 63 onshore gas fields can be observed to have a relatively large range from 85 to $144\,^{\circ}$C. The exceptionally large strain of 0.0031 at a temperature of $110\,^{\circ}$C is again from the overpressured Ameland-Oost field. Generally strains >0.0005 can be observed at lower reservoir temperatures from approximately 85 to $110\,^{\circ}$C. Around approximately 110 to $120\,^{\circ}$C only low strains occur. From $128\,^{\circ}$C higher strains occur again. From figure 11 it can be observed that from $128\,^{\circ}$C strains >0.0005 only occur with a sufficient depletion of a field in the range of 30-48 MPa. At depletion intervals of 0.1-10 and 10-20 MPa larger strains only occur at relatively low reservoir temperatures. It is hence interpreted that reservoirs at lower temperatures accommodate more strain and high-temperature reservoirs can only accommodate strain >0.0005 when the field is produced sufficiently.

Figure 12 illustrates the total seismic moment that has occurred during the production of a field versus the reservoir temperature for 65 onshore gas fields, again divided into depletion intervals. It can be observed from this figure that

higher seismic magnitudes are reached at lower reservoir temperatures and lower seismic magnitudes are reached at higher reservoir temperatures. The Tietjerksteradeel field in the Vlieland Formation has significantly lower reservoir temperature (78 °C) than the predominantly Rotliegend reservoir fields that are positioned lower in stratigraphy. It is notable that the fields with the highest maximum seismic magnitudes (Roswinkel, Bergermeer and Groningen) have relatively low reservoir temperatures. This especially accounts for the Roswinkel and Bergermeer fields, which both have reservoir temperatures of 85 °C. The Groningen field contains a reservoir temperature of 99 °C. From a reservoir temperature of 110 °C only small total seismic moments ($<1 \cdot 10^{12}$ Nm) occur. No seismicity occurs from a reservoir temperature of 133 °C and all fields generate induced seismicity below a temperature of 90 °C, indicating that the reservoir temperature parameter may have some distinguishing capacity for seismicity. Nonetheless, both fields with and without seismicity occur within a temperature range of 90-133 °C. Additionally, the limited amount and margin of error of datapoints providing some distinguishing capacity support the interpretation that reservoir temperature has no affirmative distinguishing capacity for seismic or non-seismic fields. This indicates that other parameters (e.g. reservoir geometry) are involved and seismicity is not solely based on reservoir temperature. The observations from figure 12 appear to be conform the hypothesis, considering larger total seismic moments occur at lower reservoir depths. Strikingly, the occurrence of only non-seismic fields below a reservoir temperature of 90 °C coincides with the temperature from which quartz cementation becomes significant. Yet, the relation with the level of depletion of a field seems less evident than comparing reservoir temperature to vertical strain. Figures containing illustrations of reservoir temperature versus maximum seismic magnitude, clustered per seismic magnitude (Richter scale) and per temperature range can be found in appendix 3.

To determine whether *a higher reservoir temperature causes smaller porosities due to quartz cementation from* 90 °C (Fisher et al. (2003); Walderhaug (1996)), reservoir temperature is plotted against porosity (figure 13). From figure 13 no apparent trend can be observed, where larger reservoir temperatures can be related to smaller porosities and thus no evident relation can be found that may prove this hypothesis. A very weak trend can possibly be observed where porosity is decreasing with increasing temperature. Once more, the apparent misfit may be explained by porosities that may not represent the actual initial porosities in a field and by sparse sampling density of porosity in a field. Alternatively, the temperatures from the ThermoGIS Expert tool may not be accurate enough to prove the relation between porosity and temperature. As the majority of the reservoir temperatures are above 90 °C, from which quartz cementation becomes significant, only limited datapoints occur below 90 °C. In addition, porosity is also a function of depth, initial porosity before burial, compaction coefficient and vertical effective stress (Athy (1930); Zoback (2010)), which makes it difficult to prove this relation by only illustrating reservoir temperature and porosity. Additionally, when comparing porosity versus temperature to porosity versus depth plotted in earlier sections, the illustrations look noticeably similar. This can be attributed to the large dependence of depth of both porosity.

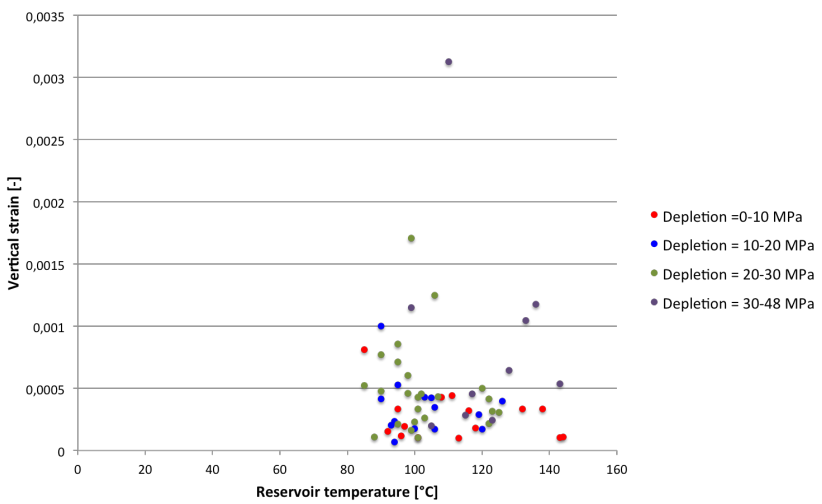

Figure 11: *Vertical strain versus reservoir temperature for 63 onshore gas fields.*

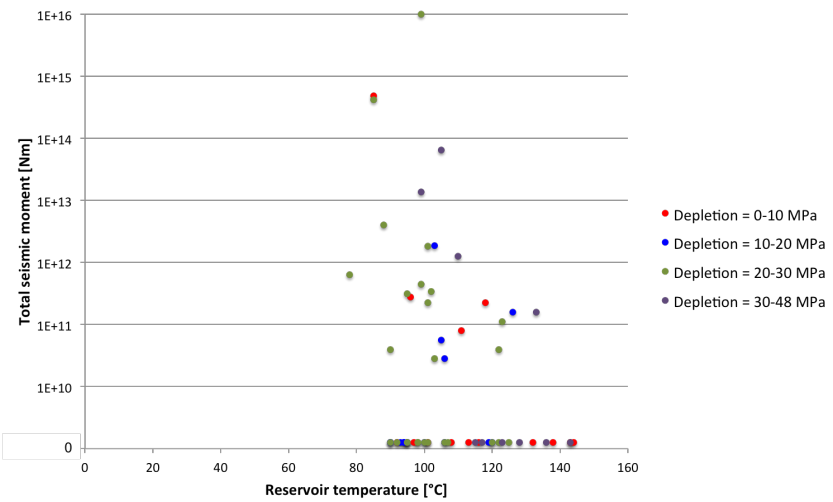

Figure 12: *Total seismic moment versus reservoir temperature for 65 onshore gas fields.*

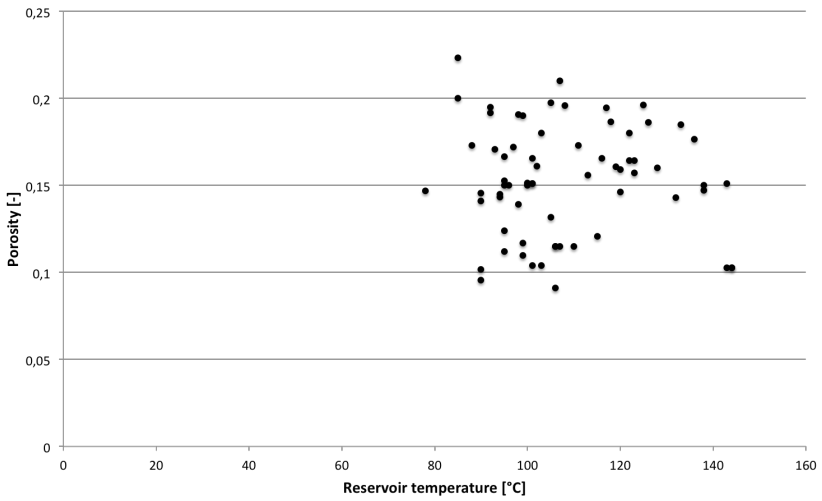

Figure 13: *Mean porosity versus reservoir temperature for 68 onshore gas fields.*

5.5 Correlation of Current Production Time, Compaction & Seismicity

Since most fields are currently in production the current time of production is used. Logically, *an increase of a fields production time will promote a larger depletion and thus fields may experience larger strains, thereby increasing the seismic potential.* When the reservoir pressure during production is lowered sufficiently, thus increasing stress, time-dependent permanent deformation may take place, where the inelastic part of the stress-strain curve is reached and grain and pore collapse occurs (Hettema et al. (2002); Zoback (2010)). This will give relatively larger strains compared to the elastic part of the stress-strain curve with an equal stress change. Firstly, the relation between current production time and depletion is verified to see whether increasing production time actually promotes larger depletion of a field. Secondly, the relation between vertical strain and seismicity versus current production time is determined. Finally the relation between the occurrence of seismicity over time in several fields with multiple induced seismic events is assessed.

Figure 14 illustrates the relation between the amount of depletion of a field versus the present production time for 65 gas fields. From this figure a trend can be observed, where generally the increase in current production time coincides with an increase in depletion of a reservoir, i.e. the lowering of the pore fluid pressure.

Figure 15 illustrates the relation between vertical strain and current production time of 63 onshore gas fields, divided into depletion intervals of 0.1-10, 10-20, 20-30 and 30-48 MPa. The current production time of the 63 illustrated gas fields ranges from 0 (Rodewolt and Usquert fields) to 52 years (Groningen field). Vertical strain appears to increase with the production time of a field. The majority of fields with a relatively low depletion of 0.1-10 MPa can be observed to have a relatively low production time, which is conform hypothesis. The two fields that have been produced the longest are the Annerveen an Groningen gas fields, having a current production time of 42 and 52 years, respectively. If, theoretically, any of the fields were positioned in the inelastic part of the stress-strain curve, this behavior would most likely be accompanied

by fields that have been produced for both a substantial amount of time and with a substantial amount of depletion. The Annerveen and Groningen field both fall within these conditions and the occurrence of time-dependent strain is expected to increase the vertical strain excessively compared to other fields. The Annerveen and Groningen gas fields both endured large strains compared to other fields, however this relation cannot be confirmed with only one data point per field.

Figure 16 is used to determine the relation between current field production time and total seismic moment. No distinguishing capacity can be demonstrated as only two fields are seismic beyond 41 years of production time and other parameters (e.g. geometry or porosity) are interpreted to be involved. Nonetheless, a trend seems to be present where higher maximum seismic magnitudes occur at larger production times. At a low current production time no induced seismicity or only low values for total seismic moment occur. This can be illustrated by the observation that within the first 10 years of production, only 4 out of the 20 fields in that production time interval are seismic. The total of examined fields is 65. Relatively highly seismic fields between maximum seismic magnitude range of 3-4 on the Richter scale, such as the Roswinkel, Bergermeer and Groningen field (maximum seismic magnitudes of 3.4, 3.5 and 3.6 and total seismic moments of $4.86 \cdot 10^{14}$, $4.23 \cdot 10^{14}$ and $1.00 \cdot 10^{16}$ Nm) on the other hand only occur from a production time of 25 years. Notable is that the Roswinkel field with a relatively large total seismic moment and maximum seismic magnitude of $4.86 \cdot 10^{14}$ Nm and 3.4 has a very small ΔP_f of only 4.1 MPa. Illustrations regarding maximum seismic magnitude versus current production time, clustered per seismic magnitude (Richter scale) and per production time range can be found in appendix 3.

Many of the 68 examined fields in this study are aseismic, namely 43 onshore gas fields. From the 25 gas fields in which induced seismicity has occurred, only a few fields generated several seismic events. To determine whether *seismicity occurrence and magnitude increase over time* four fields are chosen that have generated a substantial amount of induced seismic events: the Annerveen, Bergermeer, Eleveld and Roswinkel field. The Annerveen and Eleveld fields are currently in production, the production of the Roswinkel field was suspended in 2005 and the Bergermeer field is now being developed into an underground gas storage facility. Figure 17 illustrates all seismic events (Richter scale) that have occurred in the previously mentioned fields against the year in which they took place. From this figure can be observed that the Annerveen field shows a rough increase in seismic magnitude when focussing on the minimum seismic magnitudes over time, but a decrease in seismic magnitude looking at the maximum seismic magnitudes. The observation for the Bergermeer field is that the seismic magnitudes roughly increase over time. The Roswinkel field does not show an increase in induced seismicity over time, since the induced seismic occurrences with the largest seismic magnitudes occur in an earlier stage of field production. This same relation accounts for the Eleveld field as well. From these observations the interpretation can be made that no clear relation is seen between the year of induced seismicity occurrence and the seismic magnitude involved. Additionally, no evidence for a significantly large increase of seismic events over time can be seen, as expected when the inelastic part of the stress-strain curve is reached. Since the Annerveen, Bergermeer, Eleveld and Roswinkel fields started producing respectively from 1973, 1972, 1975 and 1980, the start of production occurred well before the occurrence of the first seismic event for each of the fields. The number of years from the start of production to the first induced seismic event is 21, 22, 16 and 12 years respectively for the Annerveen, Bergermeer, Eleveld and Roswinkel fields. From the 25 of the 68 gas fields where seismicity has occurred in the field the number of years from the start of production until the occurrence of the first seismic event is investigated. For three of the 'seismic' fields, the occurrence of induced seismicity predates the start of production (Boerakker and Rodewolt) or the time between induced seismicity and start of production is noticeably low (1 year for the Witterdiep field). The interpretation can be made that for these fields the induced seismicity may be caused by neighboring fields. The remainder of the seismic fields illustrate a mean time between the start of production and the first occurrence of induced seismicity of 16 years. A general note regarding the year of the first induced seismicity occurrence is that this year represents the first detected seismic event. For example, a geophone monitoring network was only installed in the Groningen field from 1993, thereby lowering the detection limit (NAM (2013)). No induced seismicity was detected in the northern Netherlands before 1986 (KNMI (2015)).

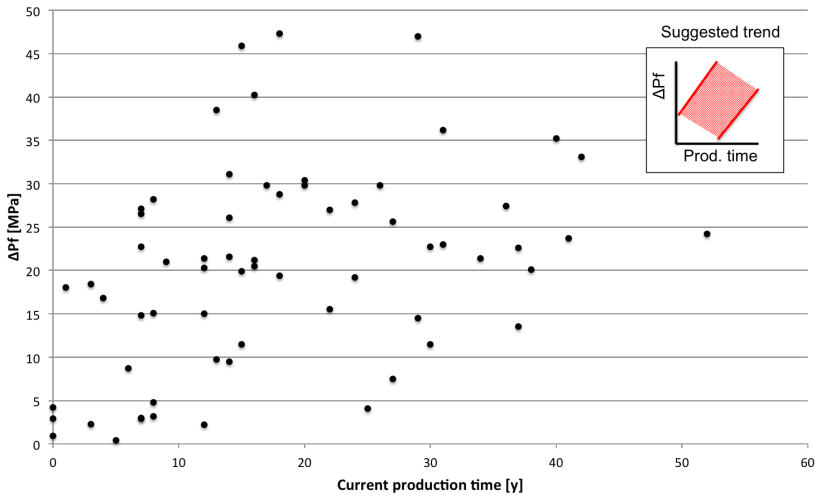

Figure 14: *ΔP_f versus current production time for 65 onshore gas fields.*

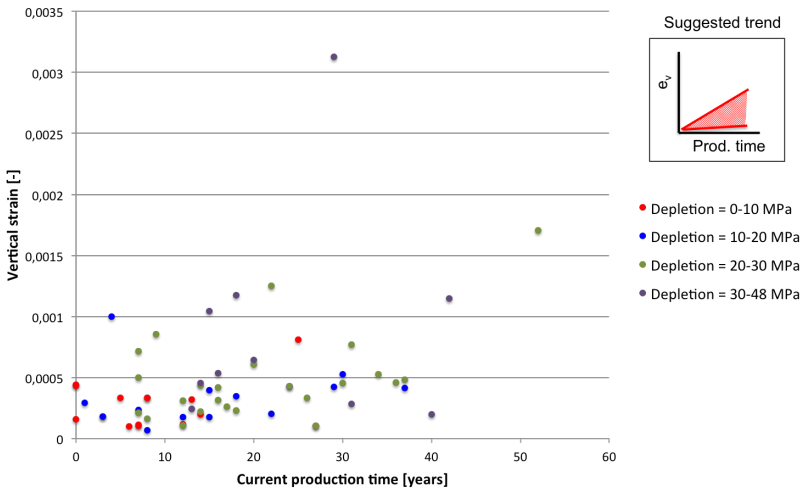

Figure 15: *Vertical strain versus current production time for 63 onshore gas fields.*

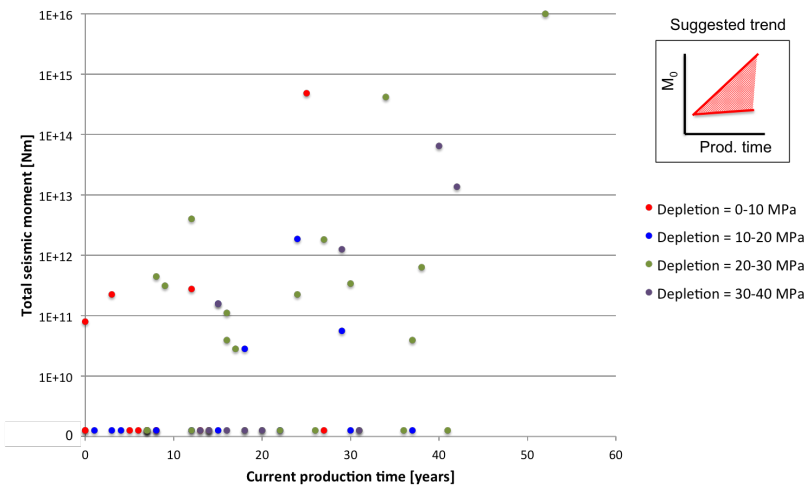

Figure 16: *Total seismic moment versus current production time for 65 onshore gas fields.*

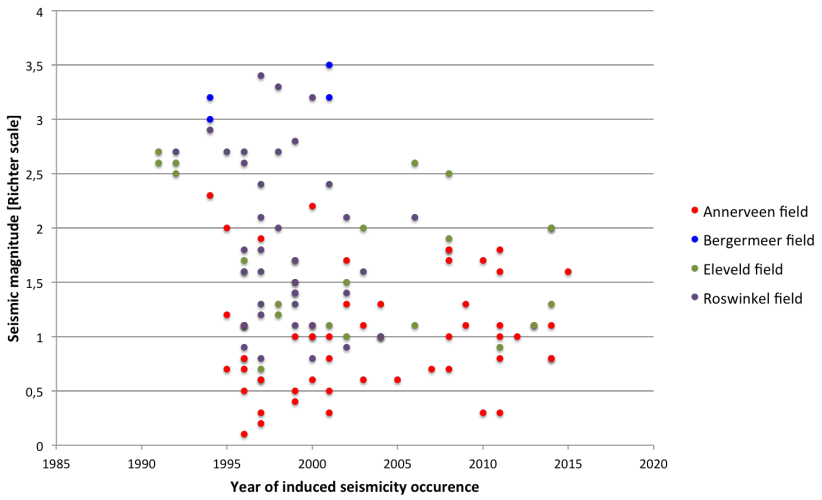

Figure 17: *Seismic magnitude (Richter scale) versus year of induced seismicity occurrence for the Annerveen, Bergermeer, Eleveld and Roswinkel fields.*

5.6 Correlation of Depth to Reservoir Top, Compaction & Seismicity

Both present depth to reservoir top and maximum burial depth in geological history influence certain reservoir parameters, e.g. the earlier discussed mean porosity (figure 10) and ΔP_f (figure 7). In this section the present depth to reservoir top is plotted against both vertical strain and seismicity, explaining the observed relation on the basis of mean porosity and degree of reservoir depletion. The general hypothesis is that *rocks at greater depths are already compacted and will not compact that significantly during depletion as rocks that are positioned at lower depths, resulting in a lower seismic potential compared to relatively shallow rocks.*

Since the maximum depth in burial history is for most of the 68 onshore gas fields based on the present depth of the reservoir top it is assumed that the results for present and maximum burial depth will be similar. The present depth to reservoir top for the 68 onshore gas fields ranges from 1940 (Tietjerksteradeel field, Vlieland Formation) to 4000 m (Ezumazijl field). Figure 18 illustrates the vertical strain versus the present depth of reservoir top for 63 onshore gas fields, subdivided by amount of depletion in a field with pore pressure decline intervals of 0.1-10, 10-20, 20-30 and 30-48 MPa (excluding the Tietjerksteradeel KNNS and RO fields). The observation is made that no single relation can be seen between an increase in vertical strain with either an increase or decrease in present depth of reservoir top. A combination of both can be interpreted, where the observed 'pyramid'-shape shows large strains around a reservoir depth of approximately 2900-3000 m. Appendix 3 shows vertical strain plotted against maximum burial depth (figure 99), generally showing similar results.

The relation between total seismic moment and present depth of reservoir top is illustrated in figure 19, subdivided per depletion interval. Present reservoir depth appears to have some distinguishing capacity for seismicity since only aseismic fields are observed from a present reservoir depth of 3653 m, however the limited amount of fields deeper than 3653 m complicate statistical relevance. A peak of seismicity appears to be present for fields with a reservoir depth around 2900 m, which is similar to the vertical strain observations. Both the Roswinkel and Bergermeer fields illustrate particularly low present depths to reservoir top (2100 and 2160 m, respectively). In these fields it is important to recognize the maximum burial depth as well. The Roswinkel and Bergermeer fields are located in the Lower Saxony Basin and the Central Netherlands Basin, respectively. Since inversion took place in these basins, the maximum burial depth becomes much higher than for the fields located in the Groningen Platform, Friesland Platform, Ameland Platform and the Lauwerszee Trough. Gaupp and Okkerman (2011) states that in these structural elements no major inversion took place and thus often the present depth of the reservoir is used as the maximum burial depth. The maximum burial depth of the reservoirs from literature in the Lower Saxony Basin (Buntsandstein) and Central Netherlands Basin are 4250 and 2800 m, respectively (Bruns et al. (2013); Nelskamp et al. (2008)). This imposes a change in figure 19, where the Roswinkel and Bergermeer field actually have a higher depth to reservoir top when the maximum burial depth is included. No distinguishing capacity for seismicity can be interpreted when incorporating maximum burial depth.

An explanation is proposed for the appearance of a 'pyramid'-shape in especially the vertical strain versus depth of the reservoir top illustration. Considering the earlier discussed mean porosity and ΔP_f relations with depth, *a certain 'high-seismicity-high strain' reservoir depth occurs around 2900-3000 m, where the reservoir depth is 1) shallow enough to remain a relatively large porosity and small initial compaction and 2) deep enough to have a large* ΔP_f. From previous sections namely a decrease of mean porosity and an increase of ΔP_f with depth is discussed. However, the relation between ΔP_f and reservoir depth is more apparent than the relation between mean porosity data. Athy (1930) and Ramm (1992)) describe a decrease in porosity with depth. This strengthens the discussion that the porosity data are

possibly not completely accurate, as described in section 5.3. Additionally the explanation considering mean porosity and ΔP_f remains plausible.

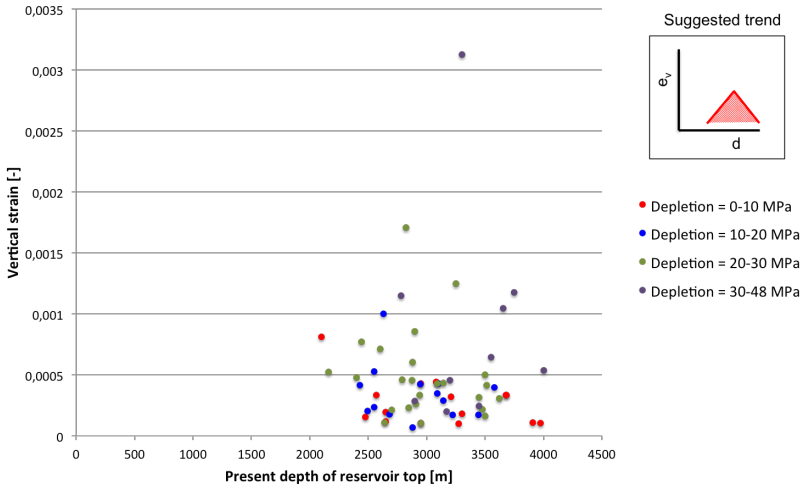

Figure 18: *Vertical strain versus present depth of reservoir top for 63 onshore gas fields.*

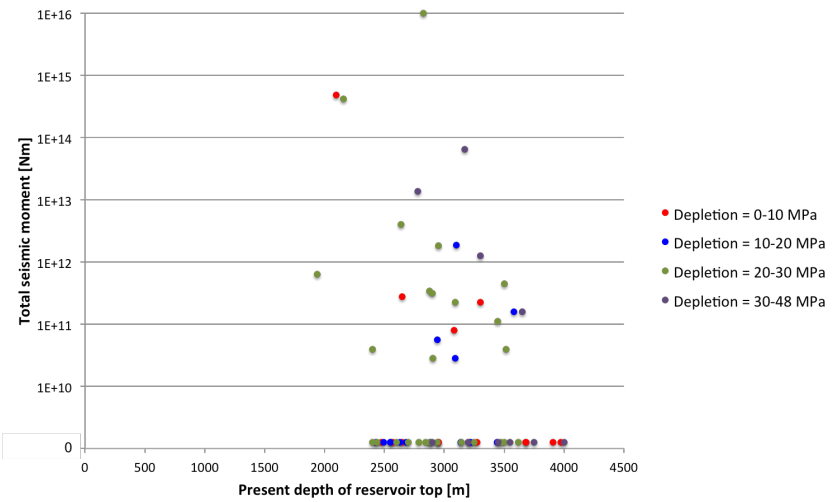

Figure 19: *Total seismic moment versus present depth of reservoir top for 65 onshore gas fields.*

5.7 Correlation of Field Geometry, Compaction & Seismicity

Orlic (2013), Holt et al. (2004) and Chilingarian et al. (1995) indicate the relevance of field geometry for determining reservoir compaction and seismic potential, thereby linking small, compartmentalized gas fields to low stress changes around the reservoir and fields with a larger areal extent and thickness to high stress changes during depletion. Certain gas field characteristics are related to its geometry, such as length, width, thickness, area and volume. These geometry aspects are described in this section to investigate whether the geometry of a gas field may influence reservoir compaction and the occurrence of seismic events, including length versus width, length versus thickness, length versus depth, width versus thickness, volume and area, and area versus thickness.

5.7.1 Length versus Width

Hypothetically it could be possible that *when the ratio between the length and width of a field is large, i.e. the field has a large length and a small width, the seismic potential is small since the field accordingly cannot accommodate for a large amount of compaction.* Additionally, a field with a length/width ratio that is close to 1, i.e. when the length of the field is similar to the width of a field, could be able to accommodate more compaction and would cause a higher seismic potential. Hence intuitively, applying an equal force to an equal area with a length-to-width ratio close to 1 compared to an area with a large length-to-width ratio will promote deformation in the area with the ratio close to 1.

To examine this hypothesis, figure 20 illustrates the ratio between length and width (L/W) versus vertical strain for 63 onshore gas fields, subdivided by amount of depletion in a field with pore pressure decline intervals of 0.1-10, 10-20, 20-30 and 30-48 MPa. Roughly, L/W ratios close to 1 appear to coincide with high vertical strains and vice versa, which is conform hypothesis. At L/W ratios larger than approximately 5 vertical strain does not exceed a value of 0.0005. Within depletion intervals of 0.1-10 and 10-20 MPa no apparent trend is visible.

An important observation not conform hypothesis is that several fields occur with a relatively low L/W ratio (<2) and a small vertical strain (<0.0005). A possible explanation is that fields with these characteristics represent relatively small fields, thereby having a small L/W ratio and additionally a small areal extent, thus unable to accommodate large vertical strains. To examine the possibility of small fields causing low strains at L/W ratios close to 1, both the areas and volumes of the 68 gas fields are determined. The areas range from $6.1 \cdot 10^5$ (Engwierum field) to $1.5 \cdot 10^9$ m^2 (Groningen field). Since the Groningen gas field is significantly larger than the remainder of gas fields, the areas excluding the Groningen gas field are used, thus ranging from $6.1 \cdot 10^5$ to $1.3 \cdot 10^8$ m^2 (Annerveen field). A definition of a small field needs to be specified and therefore firstly each area below the mean area (excluding the Groningen field) is defined as a small field. This implies that each field below an area of $1.2 \cdot 10^7$ m^2 is defined as a small field. For defining the volume of a small field similar definitions as for the area are used, i.e. eliminating the fields smaller than the mean volume (excluding the Groningen field). Using this definition, only gas fields with a volume larger than the mean volume ($1.3 \cdot 10^9$ m^2) are included. Hereby it needs to be noted that the volumes of fields are estimations, since the reservoir thickness will not be constant throughout the entire field and the field outline may be strongly irregular. Table 4 illustrates all fields defined as having a large area and volume.

Table 4: *Fields defined as having large area and volume.*

Large Area Fields	**Large Volume Fields**
Kollum	Kollum
Vries (Noord)	Vries (Noord)
Lauwersoog-Oost	Lauwersoog-Oost
Nes	Nes
Moddergat	Moddergat
Roswinkel	Roswinkel
Ameland-Oost	Ameland-Oost
Tietjerksteradeel RO	Tietjerksteradeel RO
Tietjerksteradeel KNNS	Tietjerksteradeel KNNS
Annerveen	Annerveen
Groningen	Groningen
Norg UGS	Norg UGS
Bedum	Bedum
Munnekezijn	Munnekezijl
Ameland-Westgat	Roden (block 1)
Anjum	Bergermeer
Ameland-Noord	Warffum
Blija-Ferwerderadeel	Grijpskerk UGS

Examining the relation between small fields, L/W ratio and vertical strain, the overpressured Ameland-Noord and Tietjerksteradeel RO and KNNS fields are excluded, as vertical strain cannot be determined from surface subsidence in overlying fields with a similar amount of depletion. Figure 21 illustrates the remainder of onshore gas fields excluding small fields, including the fields remaining when both the area and volume definitions of small fields are used. Relatively large vertical strains appear to be present at L/W ratios close to 1. Yet, a cluster of fields with low vertical strains and L/W ratio remains, causing small fields to only partly explain the behavior in figure 20. It could be possible that the definition of a small field is not correct and needs to be altered. An alternative explanation is possibly that other reservoir characteristics, e.g. mean porosity of a field, are involved.

Figure 22 illustrates the total seismic moment versus the length/width ratio for 65 onshore gas fields, again divided into depletion intervals. The general observation is again that the expected relation can partly be seen in figure 22 with larger total seismic moments occurring at L/W ratios closer to 1. However, seismicity is observed at high L/W ratios as well. These fields are Bedum, Witterdiep, Norg UGS and Boerakker with a L/W ratio and total seismic moment of respectively 7.89 and $3.44 \cdot 10^{11}$ Nm, 9.09 and $4.47 \cdot 10^{11}$ Nm, 7.69 and $2.80 \cdot 10^{11}$ Nm and 7.69 and $2.82 \cdot 10^{10}$ Nm. By individually examining these fields, explanations are proposed for this behavior. A possible explanation could be that the

seismicity is caused by neighboring fields that actually have a L/W ratio close to one and therefore accommodate more compaction and generate stress. Another explanation could be that the initial length/width ratio was actually not correct, since the individual fields are largely compartmentalized. Zoback (2010) states that when a reservoir is compartmentalized, one reservoir compartment behaves as one single interconnected unit, while between compartments the behavior can be significantly different. The possibility arises that a field, which was first defined as one compartment, actually is subdivided into multiple compartments. This changes the L/W ratio and possibly in such a way that the L/W ratio becomes smaller. Thus the hypothesis of seismicity occurrence with L/W ratios close to 1 still remains correct. It must however be taken into account that this explanation for seismicity and a high L/W ratio also depends on the behavior between compartments (i.e. pressure communication), which is hard to predict. Starting with the Bedum field, this field is localized next to and even partly above the Groningen gas field. The Groningen gas field has a low L/W ratio of 1.61 and could therefore be causing the seismicity in the Bedum field, that has a higher L/W ratio. The Witterdiep field shows a similar relation, where the neighboring Eleveld field has a L/W ratio close to 1 and high seismicity, which may have caused the seismicity in the high L/W ratio Witterdiep field. This is illustrated in figure 23. Information supporting the interpretation above is given in the 'Production Time' section, whereby it was interpreted to be unlikely that the Witterdiep field generated an induced seismic event after only one year of production. The previously discussed relation is not applicable in the Norg UGS and the Boerakker fields. However, looking at the structural maps, these fields are largely compartmentalized. The seismicity in the Norg UGS field seems to be centralized around only one compartment. Taking the L/W ratio of only this compartment lowers the ratio from 7.69 to 2.29. Thus, relatively high seismicity may be found in a relatively low L/W ratio, which is conform the hypothesis. Two compartments can also be observed looking at the structural map of the Boerakker field, which decreases the L/W ratio from 7.69 to 4.19. The structural map is shown together with the location of seismicity in figure 24.

Another feature shown in figure 22 is low or no seismicity at a low L/W ratio (1-2). Two explanations can be suggested for this relation, namely 1) due to the presence of small fields or 2) other factors, i.e. reservoir characteristics or parameters, are involved, causing the fields to lack of seismicity. To examine the possibility of small fields causing no seismicity and a low L/W ratio, again total seismic moment versus L/W ratio is plotted using equal definitions for small fields as in the vertical strain discussion. Each field with an area below $1.2 \cdot 10^7\ m^2$ and a volume below $1.3 \cdot 10^9\ m^3$ is defined as small. Only fields with a depletion of zero are further excluded and the Tietjerksteradeel RO and KNNS fields are included, resulting in a total number of large fields of 21. In this configuration about $\frac{2}{3}$ of the fields are hence defined as small. The results of the small field elimination are illustrated in figure 25. The observation is made that, similar to the vertical strain discussion, a rough trend appears to be conform hypothesis with larger strains occurring at relatively low L/W ratios and vice versa. Excluding small fields does remove a significant amount of fields with zero seismicity. However, even in this case no seismicity occurs at a low L/W ratio, suggesting that other field characteristics, e.g. porosity or depth, must be involved.

Since the Tietjerksteradeel Rotliegend (RO) and Vlieland (KNNS) fields are located above each other at the same location it could be interesting to examine the occurrence of seismicity in these fields. The main difference between these fields is the depth at which the reservoir is located (2400 and 1940 m for the RO and KNNS field respectively). In both fields the present depth of reservoir top represents the maximum burial depth. Also, the thickness of the KNNS field is much smaller than the RO field (30 m compared to 140 m). Apart from the depth of both fields the Tietjerksteradeel RO and KNNS fields are mostly similar, having a porosity and depletion of 19 and 15 % and 23.7 and 20.1 MPa, respectively. Both fields are also defined as large, using both the area and volume definition of a small or large field. From earlier results and discussion it is expected that larger strains occur at 2400 m compared to 1940 m at a large reservoir thickness and high porosity. The Tietjerksteradeel RO field is thus expected to have the largest seismic potential. However, one seismic event with a seismic magnitude of 1.8 on the Richter scale occurs in the KNNS field, approximately 5 km laterally from the Tietjerksteradeel RO field. Since other reservoir parameters indicate a higher seismic potential for the Tietjerksteradeel RO field, a large influence of geometry, namely L/W ratio is proposed. The length and width data of both fields do not differentiate much, with approximate values of 10400, 4000 and 12000, 5250 and corresponding L/W ratios of 2.6 and 2.3 for the RO and KNNS fields, respectively. The L/W ratio of the Tietjerksteradeel KNNS field is somewhat smaller, suggesting a higher seismic potential. However, the difference in L/W ratio of both fields is 0.3 only, which is possibly to small to influence seismic potential. The structural maps of both fields indicate that the Tietjerksteradeel KNNS field is not compartmentalized, while the Tietjerksteradeel RO field is, increasing its L/W ratio due to the geometry of the compartments. Hence, induced seismicity generated due to a large influence of geometry (L/W ratio) is inferred to be a reasonable explanation for the occurrence of seismicity in the Tietjerksteradeel KNNS field. Nevertheless, the explanation above is based on one seismic event, having a relatively large lateral (500 m) and vertical (1-2 km) uncertainty. Additionally, the Opeinde field, which is not considered within the 68 examined onshore gas fields, is positioned at lower depth than the Tietjerksteradeel KNNS field. The induced seismic event was not been located in the Opeinde field, but this field is located close to the lateral uncertainty range with a distance of 576 m from the seismic event.

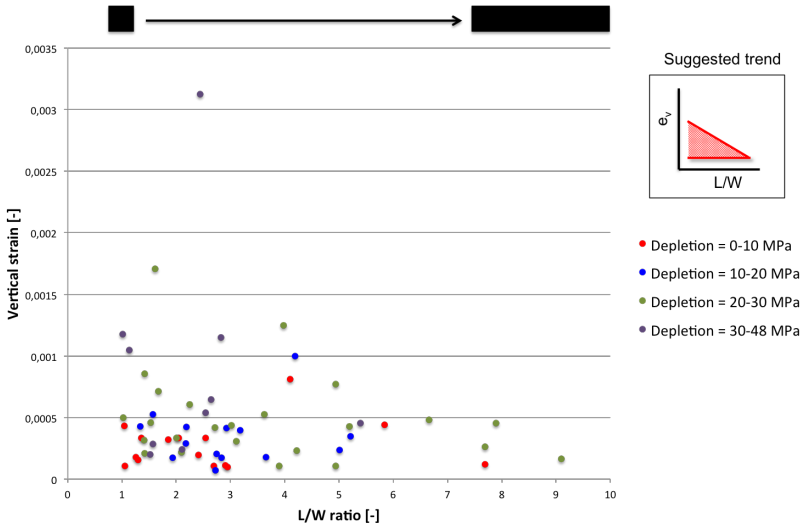

Figure 20: *Vertical strain versus L/W ratio for 63 onshore gas fields.*

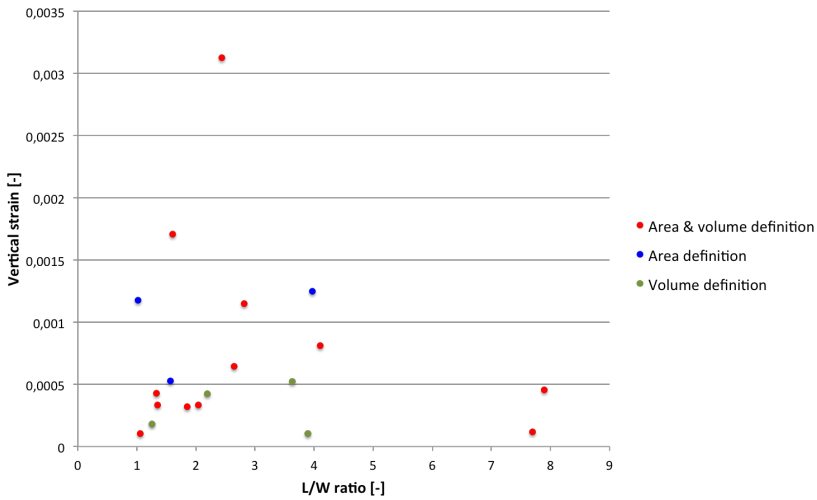

Figure 21: *Vertical strain versus L/W ratio for 19 large onshore gas fields, excluding small fields by using the area and volume definition (see table 4).*

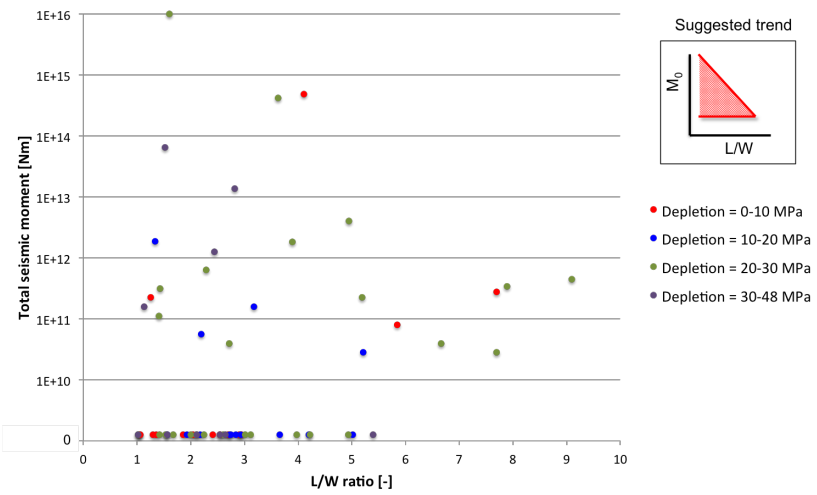

Figure 22: *Total seismic moment versus L/W ratio for 65 onshore gas fields.*

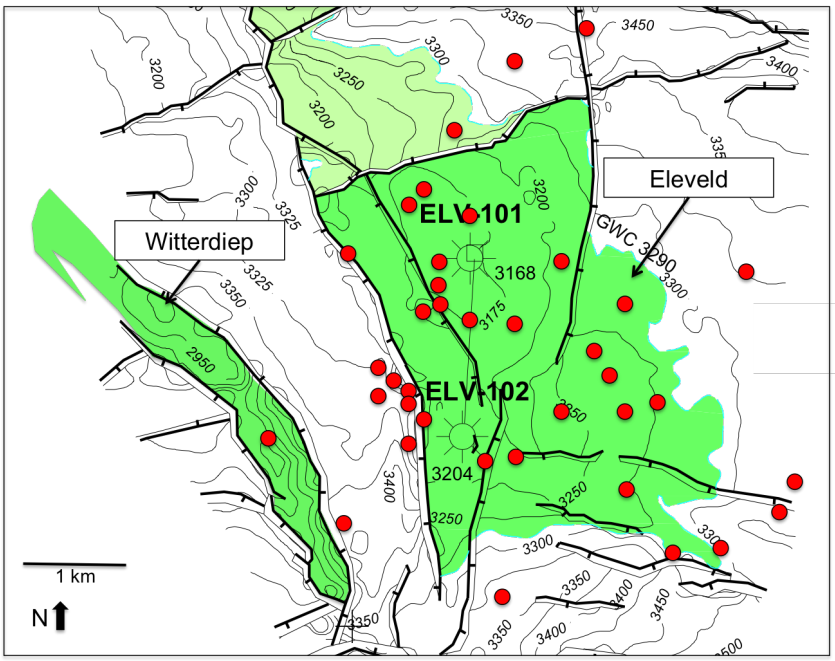

Figure 23: *An example of seismicity in a high L/W ratio field (Witterdiep) possibly due to a low L/W ratio neighboring field (Eleveld). The red location points represent the locations of seismic events with a maximum lateral uncertainty of 500 m (adapted from KNMI (2015); NLOG (2005)).*

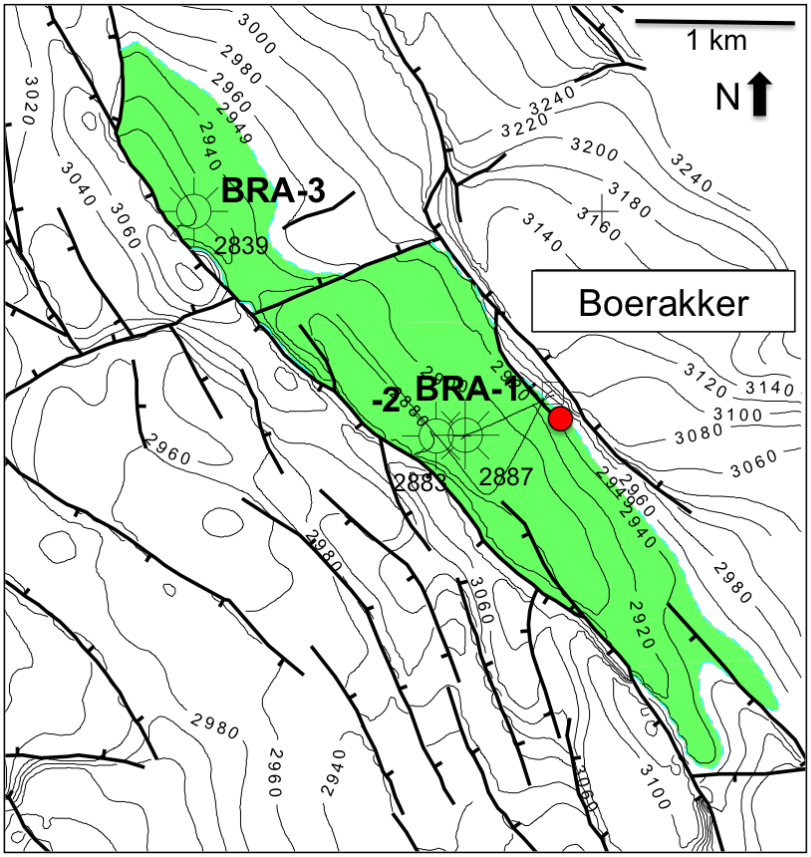

Figure 24: *An example of seismicity in a high L/W ratio field (Boerakker) possibly due to field compartmentalization. The red dot illustrates the location of a seismic event with a maximum lateral uncertainty of 500 m (adapted from KNMI (2015); NLOG (2005)).*

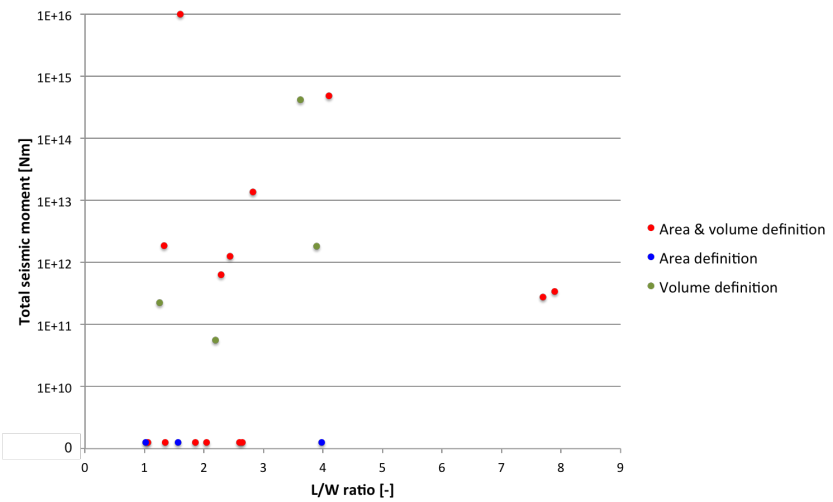

Figure 25: *Vertical strain versus L/W ratio for 21 large onshore gas fields, excluding small fields by using the area and volume definition (see table 4).*

5.7.2 Length versus Thickness

Since a higher reservoir thickness may enhance the ability of the reservoir to accommodate compaction this is considered as an important parameter. Reservoir thickness is discussed in Chilingarian et al. (1995), that states that significant compaction can occur if a reservoir has a significant thickness (>50 m). The hypothesis is that *a larger reservoir thickness will accommodate larger vertical strains and thus increases seismic potential.* Consequential, *an increase in vertical strain and induced seismicity is expected with a decrease of the ratio between length and thickness (L/t ratio).* In this section firstly vertical strain and seismicity is plotted against reservoir thickness. Subsequently, the ratio between length and thickness, vertical strain and seismicity is examined.

A side note considering the reservoir thickness parameter is required. As mentioned in earlier sections the increase in vertical effective stress during depletion causes compaction in the reservoir (Doornhof et al. (2006)). Since a producing reservoir is partly water-bearing and partly gas-bearing, this may effect pressure communication. During depletion of a field the water-bearing interval of the reservoir may equal the gas pressure. However, due to residual gas in reservoir pores some fields do not have complete pressure communication (Holtz (2002)). Without pressure communication no change in vertical effective stress occurs in the water-bearing interval and the compacting thickness is the thickness of the gas column. Since no information on pressure communication per field for the 68 examined gas fields is available, the complete thickness of the reservoir is used as a parameter in this study. Taking two extremes; both plotting complete reservoir thickness and thickness of the gas-bearing interval versus vertical strain and total seismic moment is considered. Since the determination of trends is difficult using one parameter only (as illustrated in previous sections) it is assumed that taking both the complete reservoir thickness and the thickness of the gas-bearing interval will lead to highly scattered data, in which the range is too large to determine a trend. Hence, this study focuses on the complete reservoir thickness only.

Figure 26 illustrates the vertical strain versus the reservoir thickness for 63 onshore gas fields, subdivided per depletion intervals of 0.1-10, 10-20, 20-30 and 30-48 MPa. No clear evidence for an increase in vertical strain with increasing reservoir thickness can be observed. A very rough decrease in vertical strain may be seen with an increase in reservoir thickness, which does not correspond to the hypothesis. Most fields that are thin and have relatively large vertical strain (>0.0005) are depleted severely (>20 MPa). It is inevitable that the vertical strain versus reservoir thickness relation, which is not conform hypothesis, influences the results when computing the vertical strain versus L/t ratio.

Core observations from NAM along with Nichols (2009) imply that thick sedimentary formations consist of higher porosity rock e.g. aeolian dune depositions. Most reservoirs examined in this study are Rotliegend sandstones with a predominantly aeolian depositional environment and are therefore expected to have a relatively high thickness. Figure 27 illustrates the relation between reservoir thickness versus porosity, indicating a rough trend of increasing porosity with increasing thickness.

Total seismic moment is plotted against reservoir thickness in figure 28. A rough trend conform hypothesis appears to be present, with increasing total seismic moments at increasing reservoir thicknesses. In addition, seismicity occurs at relatively low reservoir thickness in severely depleted fields (20-48 MPa) and vice versa, indicating that reservoir depletion is important for the occurrence of seismicity. No distinguishing capacity for the occurrence of only seismic or aseismic fields at a certain thickness range can be observed, indicating that other parameters (e.g. porosity or L/W ratio) are involved as well. The observation that vertical strain versus thickness is not conform hypothesis but seismicity versus vertical strain is, implies that induced seismicity is not generated solely as an effect of vertical strain.

Figure 29 illustrates the vertical strain versus L/t ratio for 63 onshore gas fields, again subdivided into depletion intervals. Since most data is clustered in a L/t ratio between 0-100, a general trend is difficult to observe. A very rough trend may be observed where an increase in L/t ratio shows an increase in vertical strain as well. This is not conform hypothesis, since a negative relation between vertical strain and L/t ratio was expected. This may be due to inaccurate strain data or because both the numerator (length) and denominator (thickness) are very small, giving both a small L/t ratio (<100) and vertical strain. Figure 26 roughly illustrated large vertical strains at relatively low reservoir thicknesses, a trend which may have influenced the L/t ratio results, since the results of 26 and 29 are in agreement with each other. However, to fully exclude the possibility of length influencing the results, vertical strain versus length of the reservoir is plotted (appendix 3, figure 100), from which can be seen that an increase in reservoir length roughly increases vertical strain. It is thus interpreted that the rough increase in vertical strain with increasing L/t ratio (not conform hypothesis) is caused by the correlation of thickness and vertical strain (not conform hypothesis) rather than the correlation of length and vertical strain (conform hypothesis).

Figure 30 shows the total seismic moment versus the ratio between the length and thickness of a field. It can be seen that in general all large seismic events are at a relatively low L/t ratio, which is conform expectation since for a seismic field both the length and the reservoir thickness are expected to be large. The limited availability of data at a L/t ratio >100 however makes it difficult to indicate trends.

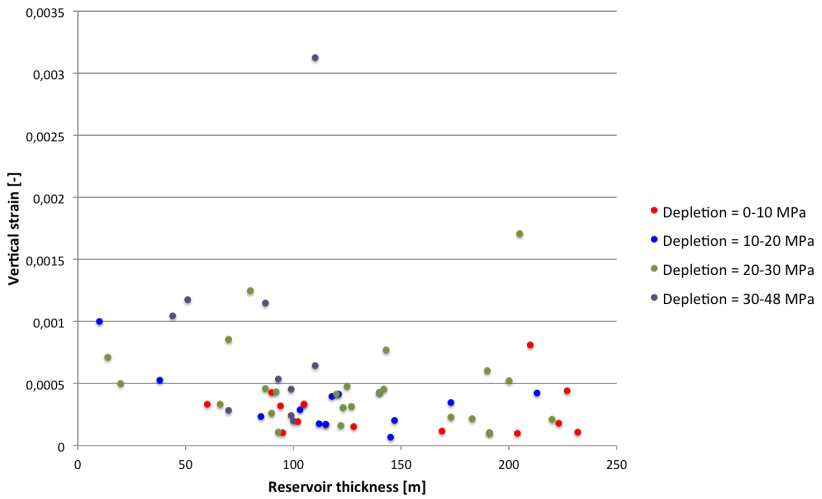

Figure 26: *Vertical strain versus reservoir thickness for 63 onshore gas fields.*

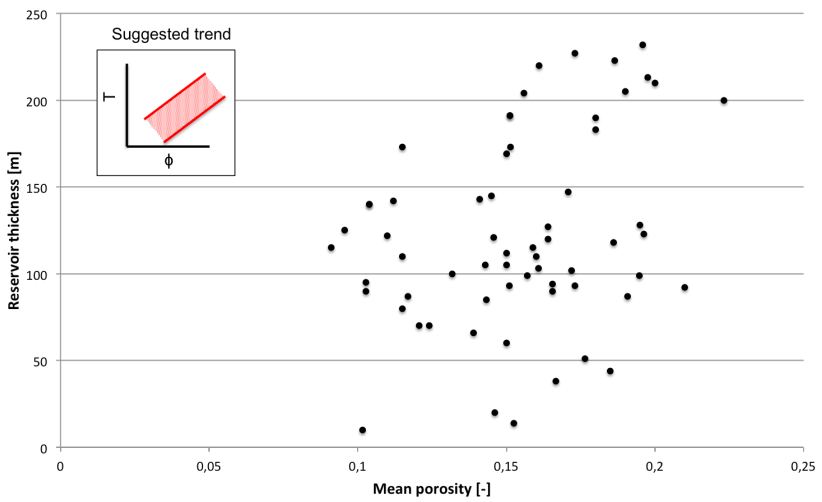

Figure 27: *Reservoir thickness versus porosity for 63 onshore gas fields.*

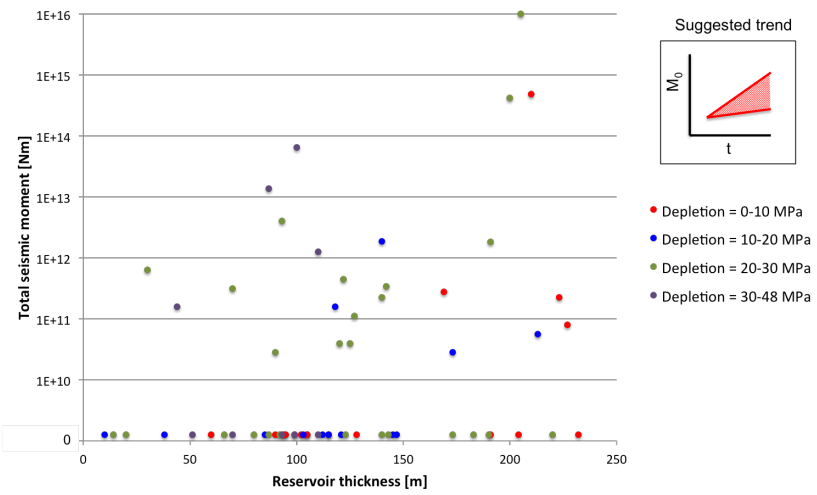

Figure 28: *Total seismic moment versus reservoir thickness for 65 onshore gas fields.*

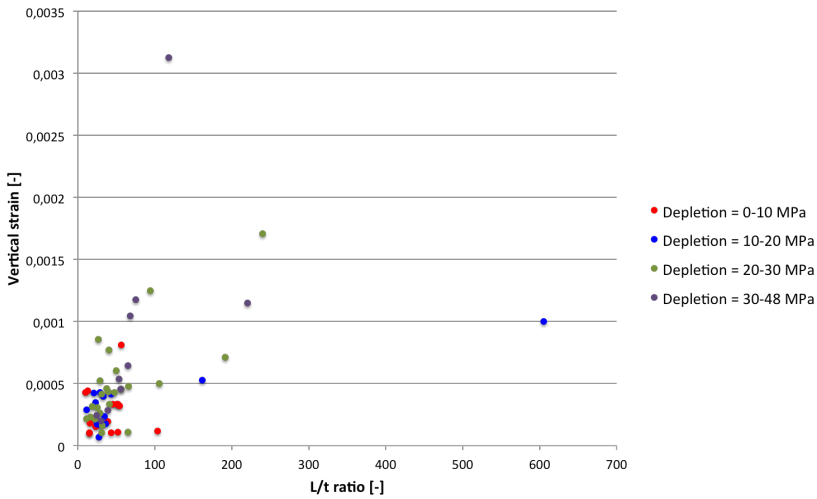

Figure 29: *Vertical strain versus L/t ratio for 63 onshore gas fields.*

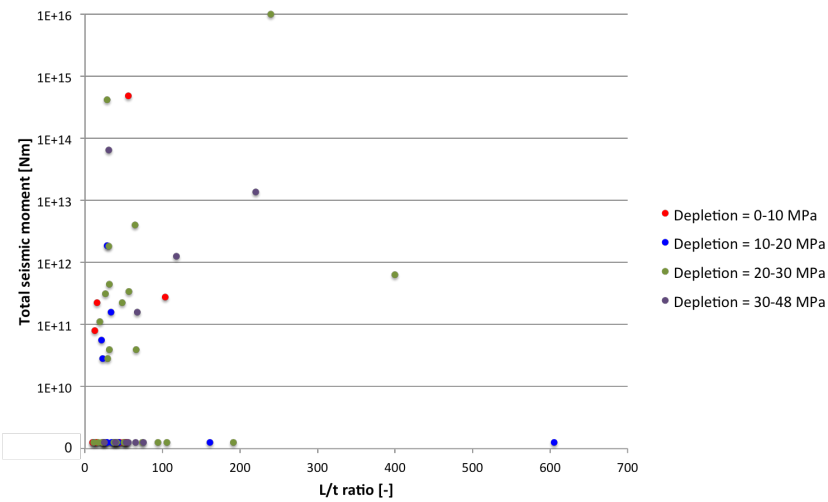

Figure 30: *Total seismic moment versus L/t ratio for 65 onshore gas fields.*

5.7.3 Length versus Present Depth of Reservoir Top

The relation between vertical strain, total seismic moment, maximum seismic magnitude and the depth of reservoir top is discussed in previous sections (figure 18) illustrating large strains and induced seismic events around a reservoir depth of approximately 2900-3000 m. Additionally figure 100 illustrates an increase in vertical strain with an increase in length. This section describes the relation between reservoir length and depth, thereby combining both parameters. Considering the relation between vertical strain and both parameters, *length/depth (L/d) ratio is expected to have low vertical strain values initially, continuing with a steep increase in vertical strain and seismicity with increasing L/d ratio.*

Vertical strain versus L/d ratio for 63 onshore gas fields is illustrated in figure 31, divided into depletion intervals. A large number of fields can be observed initially with a relatively low vertical strain and low L/d ratio (<0.0005 and <1.7 respectively), from which subsequently a weak increase in vertical strain with L/d ratio can be seen. This very weak trend is conform hypothesis. However the majority of fields have a present depth to reservoir top similar to the length of the field, thereby making it difficult to distinguish between different L/d ratio values. A few fields with a low L/d ratio and a strain >0.0005 can be seen, which are mainly fields that are severely depleted. Several fields distinct in figure 31, namely the Ameland-Oost, Annerveen, Groningen and Norg UGS fields having a vertical strain and L/d ratio of 0.0031 and 3.93, 0.0012 and 6.90, 0.0017 and 17.42, 0.00012 and 6.59, respectively. The distinctive position of the Ameland-Oost field in figure 31 can be explained by its larger vertical strain, as earlier discussed possibly due to its severely overpressured state. The Groningen and Annerveen fields both are very large compared to their depth and hence have higher L/d ratios. The Norg UGS field outlies with a noticeably low vertical stain with a relatively high L/d ratio. This may be explained since the Norg UGS field is highly compartmentalized, thus possibly reducing the length and the L/d ratio of each compartment.

Figure 32 illustrates the total seismic moment versus the ratio between the length and depth of a field (L/d ratio) for 65 onshore gas fields, thus including the Tietjerksteradeel RO and KNNS fields. It can be observed that L/d ratio may have some distinguishing capacity for seismicity, with seismic fields only occurring from a ratio of 4.33. Before a L/d ratio of 4.33 both seismic and aseismic fields occur. However, the limited amount of data points from a ratio of 4.33 (4) inhibit statistical relevance.

The L/d ratio of 4.33 ratio belongs to the relatively long and shallow-positioned Tietjerksteradeel RO field (present depth of reservoir top of 2400 m), thereby increasing the L/d ratio value. However, this field is compartmentalized and hence the L/d value of each compartment decreases. Without the Tietjerksteradeel RO field the distinguishing capacity for seismicity would be observed from a L/d ratio value of 2.35, slightly increasing statistical relevance. It appears from figure 32 that the seismic moment increases with an increasing L/d ratio, with aseismic fields occur almost solely at low L/d ratios. This may be explained since very large depths give relatively small strains, partly because of high initial compaction. The interpretation can be made that from a L/d ratio of 2.35 seismicity always occurs. Below a L/d ratio of 2.35 both seismic and aseismic fields occur and other parameters may be involved, e.g. the L/W ratio.

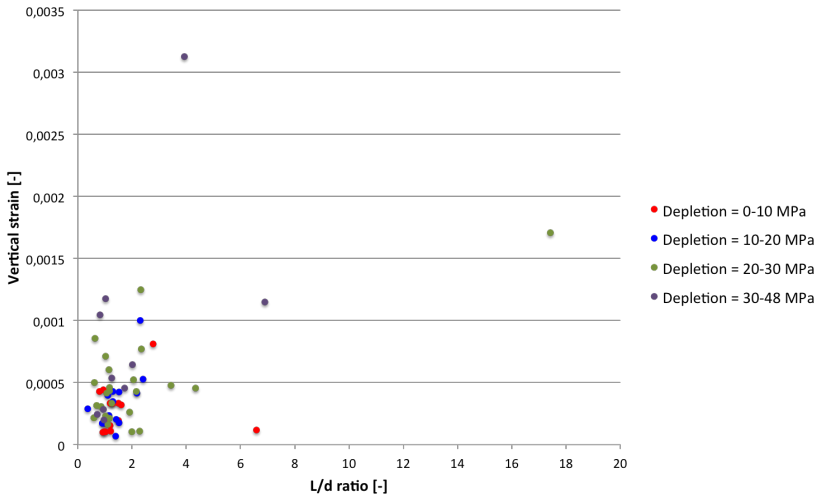

Figure 31: *Vertical strain versus L/d ratio for 63 onshore gas fields.*

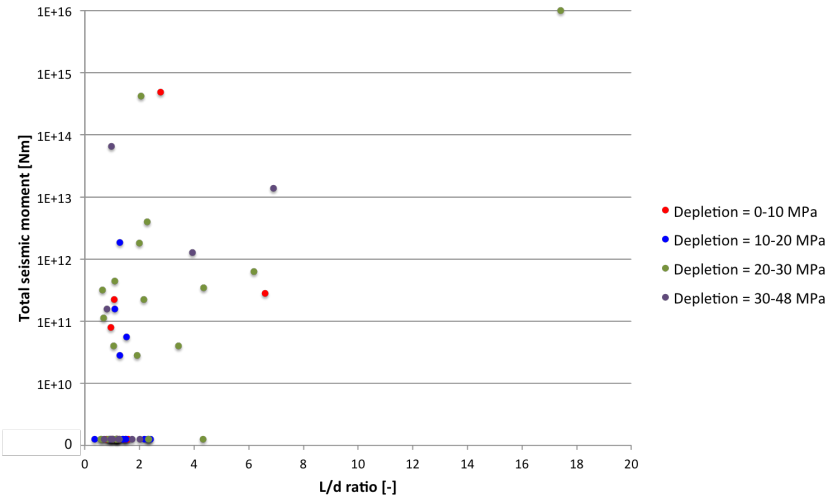

Figure 32: *Total seismic moment versus L/d ratio for 65 onshore gas fields.*

5.7.4 Width versus Thickness

This section describes the relation between vertical strain, seismicity and the ratio between width and thickness of a field. Field width, vertical strain and total seismic moment are plotted first. The relation between reservoir thickness, vertical strain and seismicity is already defined in a previous section. The hypothesis from literature is that a larger thickness can accommodate more compaction and hence strain. A larger width would, conform the L/W ratio hypothesis, imply larger vertical strains as well. The hypothesis hence is that *an increase in W/t ratio gives a decrease in vertical strain and seismic potential.*

Figure 33 illustrates the vertical strain versus the field width for 61 onshore gas field, subdivided into depletion intervals of 0.1-10 MPa, 10-20 MPa, 20-30 MPa and 30-48 MPa. The Groningen (width = 30640 m) and Ameland-Oost (vertical strain = 0.0031) fields are omitted from the plot to improve visibility of the figure, but their positions are in line with the suggested trend. From figure 33 the observation can be made that, conform hypothesis, the vertical strain increases roughly with field width.

The relation between total seismic moment and field width is illustrated in figure 34. In this figure only the Groningen field is removed for visibility improvement. Yet, the position is in line with the suggested trend. Similar to figure 33 the total seismic moment increases roughly with field width. Most seismic fields with relatively low field widths (<1500 m) are severely depleted (ΔP_f >20 MPa). At larger widths, both severe and mildly depleted fields show seismicity. Fields that have a very large width (>5000 m) are severely depleted as well, possibly due to their large reservoir volume and associated gas in place. Since exclusively seismic fields occur from a width of 4000 m, field width can be interpreted to have distinguishing capacity for seismicity. However, only 3 fields occur with a width larger than 4000 m, thus the interpretation yields uncertainty.

By knowing the behavior of field width regarding vertical strain and seismicity, the relation between width/thickness ratio versus vertical strain and total seismic moment can be examined. Vertical strain versus W/t ratio for 63 onshore gas fields is illustrated in figure 35.

A large strain of 0.0031 can again be observed in the Ameland-Oost field. As most data is clustered between a L/t ratio between 0-30, a general trend is difficult to observe. Roughly, an increase in W/t ratio illustrates an increase in vertical strain. As a decrease in vertical strain was expected at increasing W/t ratios, this observation is not conform hypothesis. This may be due possibly inaccurate strain data. Reservoir thickness plotted against vertical strain resulted in a rough trend of decreasing vertical strain with increasing thickness, a relation that could also explain the observed trend in figure 35. Another explanation could be that both width and thickness of a field are very small, thereby resulting in low vertical strains at low W/t ratios. It is interpreted to be most likely that the rough trend that is not conform hypothesis is caused by a combination of the factors above.

At last, figure 36 illustrates the total seismic moment versus the W/t ratio for 65 onshore gas fields subdivided per depletion interval. The observation can be made that, different from figure 35, a relatively large number of seismic fields occur with a low W/t ratio (<20). On the other hand, from a W/t ratio of approximately 45 severely depleted fields occur only. A rough increase in seismic moment can be observed with increasing W/t ratio. The figure is thus interpreted to be partly conform hypothesis. Both seismic and aseismic fields occur within almost the complete W/t ratio range, thus no distinguishing capacity for seismicity can be interpreted.

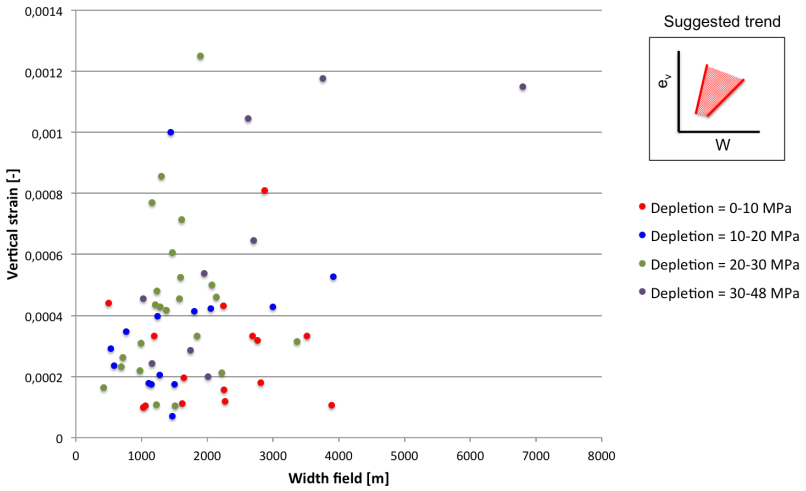

Figure 33: *Vertical strain versus field width for 61 onshore gas fields.*

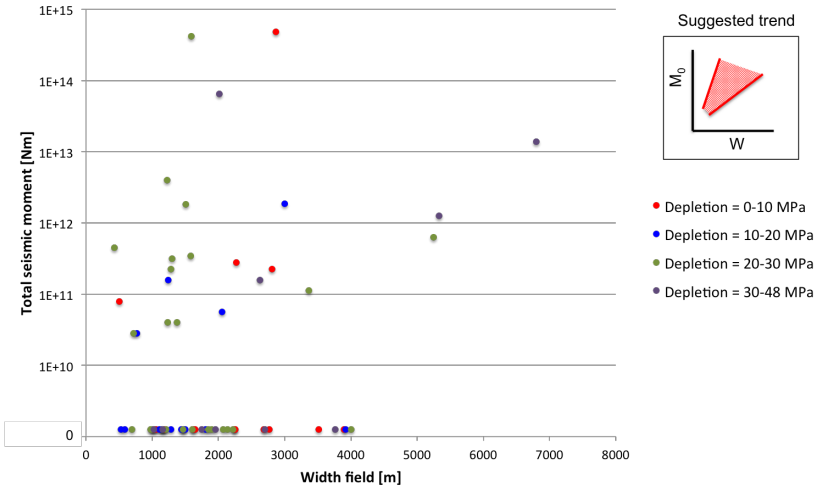

Figure 34: *Total seismic moment versus field width for 64 onshore gas fields.*

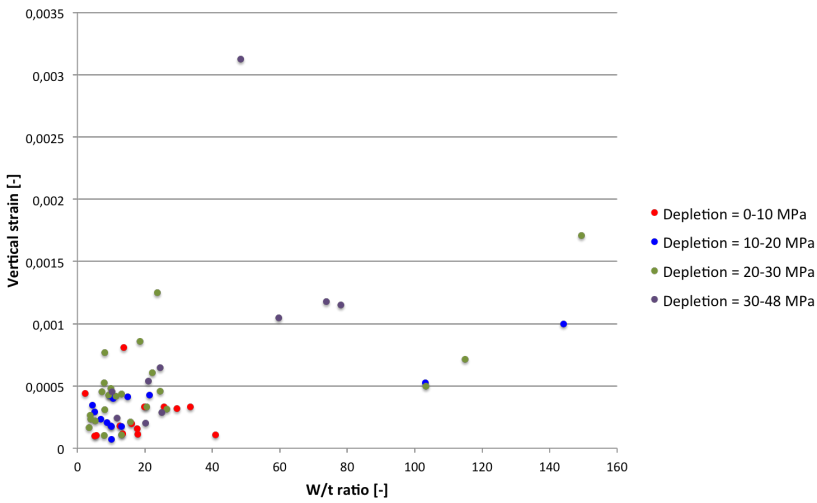

Figure 35: *Vertical strain versus W/t ratio for 63 onshore gas fields.*

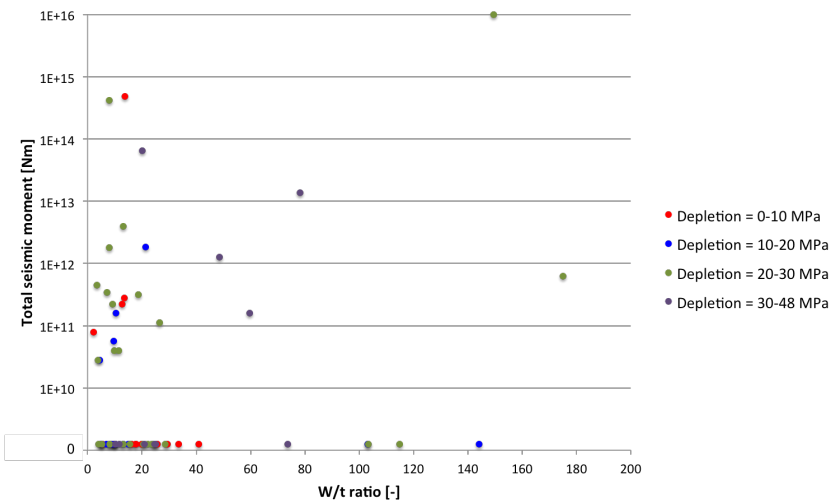

Figure 36: *Total seismic moment versus W/t ratio for 65 onshore gas fields.*

5.7.5 Area and Volume

Literature, e.g. Orlic (2013) and Chilingarian et al. (1995), describes areal extent and thickness of a reservoir in relation to the degree of compaction, in which *larger compaction and stress changes are expected in fields with a large areal extend and thickness.* Field area and volume in relation to vertical strain and seismicity are described in this section.

Vertical strain versus reservoir area is illustrated in figure 37, divided per depletion interval. The high-strain Ameland-Oost field is omitted from this figure. The Annerveen and Groningen fields, having an approximate area of respectively $1.3 \cdot 10^8$ and $1.5 \cdot 10^9$ m^2 are removed from figure 37 as well, improving visualization of results. From figure 37 three different clusters of fields are observed, with firstly a cluster with low vertical strains (<0.0005) and small areas ($<10 \cdot 10^6$ m^2), which is conform hypothesis. Secondly, a cluster with high vertical strains (>0.0005) at relatively small field areas. Most of these fields are largely depleted, which could explain the observed behavior. An increase of vertical strain with increasing area can be observed as well, occurring in fields of all depletion ranges. It is interpreted that both depletion and area of a field can be predominant; small-area fields can generate large strains if they are severely depleted and large-area fields can generate large vertical strains within all depletion ranges.

The Norg UGS field illustrates a low vertical strain at a large area (vertical strain = 0.00012, area = $40 \cdot 10^6$ m^2). This behavior is interpreted to be due to a large L/W ratio of 7.69, i.e. a large length and a small width of the field, thereby unable to accommodate large compaction. An important side note is that area is determined by taking the length times the width of the particular field. Ergo, the area defined in this study is an approximate value and, if a field is irregularly shaped, may be overestimated.

Figure 38 illustrates the total seismic moment versus the field area for 61 onshore gas fields (including the Ameland-Oost and Tietjerksteradeel fields). A weak trend conform hypothesis appears to be present, where higher total seismic moments occur at larger field areas. The majority of seismic moments of small field areas occurs in fields that have been depleted between 20-48 MPa.

To examine whether an increasing field volume increases vertical strain and total seismic moment as well, these parameters are plotted in figure 39 and 40, subdivided per depletion interval. Figure 39 illustrates the vertical strain versus the reservoir volume, whereby the Ameland-Oost, Groningen, Tietjerksteradeel KNNS and RO and Annerveen and the three fields with zero depletion are not incorporated into the figure. The different clusters observed when looking only at reservoir area appear to be less clear in figure 39. Conform hypothesis, a cluster with low vertical strains (<0.0005) and low field volumes ($<1.3 \cdot 10^9$ m^3) can be observed. Also, a cluster with relative high vertical strains, low field volumes and a high degree of depletion (>20 MPa) can be seen (with the Een field as a high-strain ,i.e. 0.001, exception due to its very small initial thickness). This may be due to the thickness parameter considered when the volume of a field is determined. The thickness parameter has illustrated a relation with vertical strain not conform hypothesis, thereby effecting the results when plotting reservoir volume. This relation also accounts for figure 40, where total seismic moment is plotted against reservoir volume. The interpretation is made that although the thickness parameter alters the results and no strong correlation is seen, for both computing seismicity and strain versus reservoir volume the hypothesis is roughly correct.

Since is it preferable to compare parameters with similar units, figure 41 illustrates the relation between total seismic moment and reservoir volume $\cdot$ ΔP_f. A total of 25 of the 68 onshore examined onshore gas fields is seismic. In figure 41 very large fields, such as Groningen, Annerveen, Tietjerksteradeel KNNS and Ameland-Oost, are omitted. From the figure a positive linear relation can be observed between total seismic moment and reservoir volume times depletion. This is conform expectation, since the hypothesis is that with an increasing areal extend, thickness and degree of depletion the total seismic moment of a field increases as well. Due to its very large thickness and fairly large area and amount of

depletion the Bedum field is an outlier relative to the rest of the data in figure 41 (total seismic moment = $3.44 \cdot 10^{11}$ Nm, ΔP_f·reservoir volume = $9.85 \cdot 10^{10}$ m^3). Another explanation for the large ΔP_f·reservoir volume of the Bedum field is an overestimation of its volume since the field is compartmentalized and the compartments may not be in pressure communication with each other.

Appendix 3 illustrates figure 101, separating figure 41 for the volume definition of small and large fields. Using this definition, a field with a larger volume than the mean volume ($1.3 \cdot 10^9$ m^3) is defined as large. No conclusive results can be interpreted from this figure, since both field defined as small and large occur in the whole ΔP_f·reservoir volume range. However, small fields appear to roughly occur in the low seismic moment - low ΔP_f·reservoir volume range.

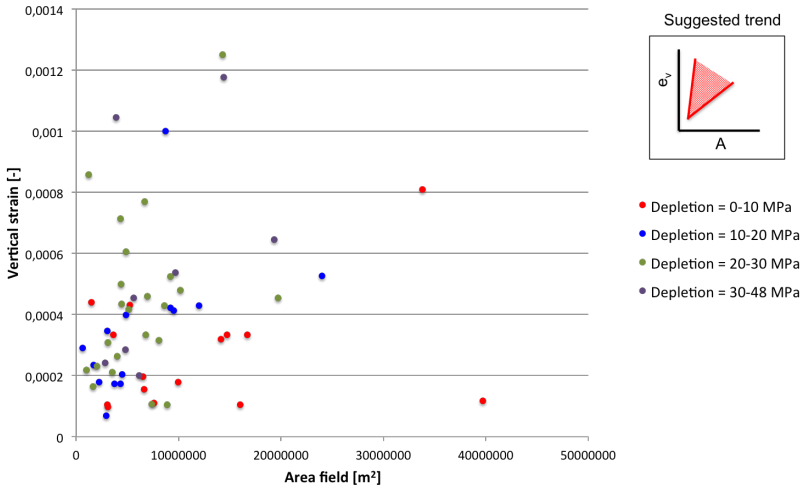

Figure 37: *Vertical strain versus field area for 60 onshore gas fields.*

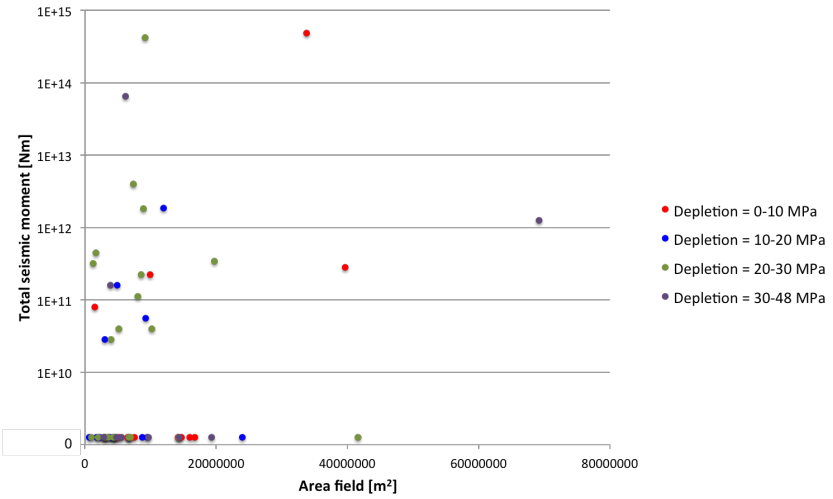

Figure 38: *Total seismic moment versus field area for 63 onshore gas fields.*

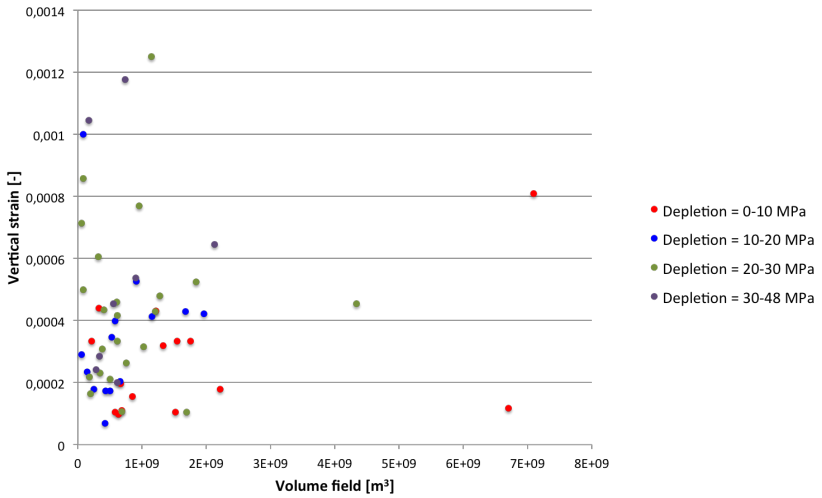

Figure 39: *Vertical strain versus field volume for 60 onshore gas fields.*

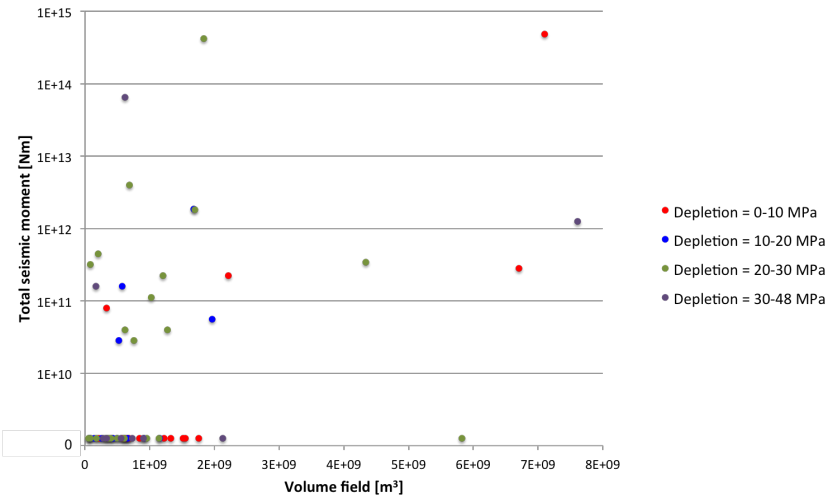

Figure 40: *Total seismic moment versus field volume for 63 onshore gas fields.*

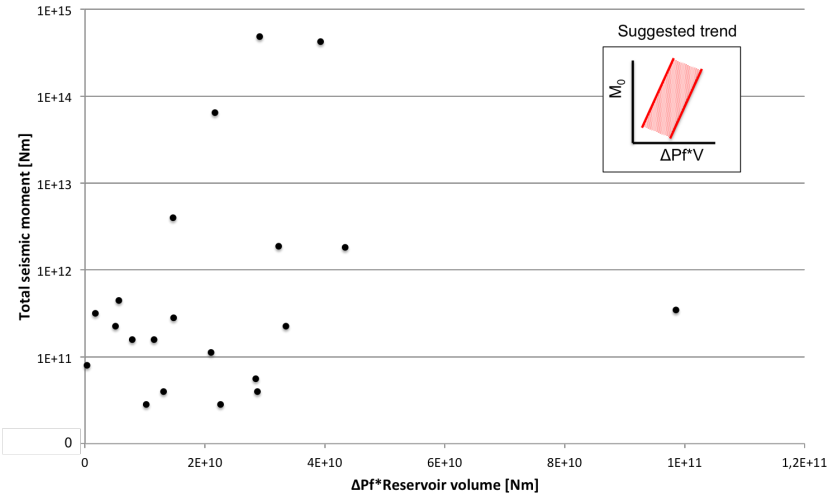

Figure 41: *Total seismic moment versus reservoir or field volume times ΔP_f for 21 seismic onshore gas fields.*

5.7.6 Area versus Thickness

The relation between vertical strain and seismicity versus area and thickness aside from each other is determined in previous sections. This section describes the relation between the area/thickness (A/t) ratio, vertical strain and total seismic moment. From literature it is expected that an increase in areal extent and thickness entails an increase in vertical strain and total seismic moment. *An increase in A/t ratio would thus imply a decrease in vertical strains and seismic potential.*

Vertical strain versus A/t ratio for 60 gas fields is illustrated in figure 42, subdivided into depletion intervals of 0.1-10, 10-20, 20-30 and 30-48 MPa. As in the discussion of area and width, this figure contains 60 onshore gas field to improve visibility of the results. A region of relatively low A/t ratio (<100 000) and low vertical strain, not conform hypothesis, can be observed in figure 42. High vertical strain (>0.0005) at low A/t ratios can also be observed, in which the fields are severely depleted (ΔP_f >20 MPa). Furthermore the observation is made that a rough increase in vertical strain appears with increasing A/t ratio.

In an attempt to explain this behavior several interpretations are made. The low vertical strain-low A/t ratio region may occur since in this region both area and thickness are small and the field is therefore unable to accommodate a large amount of compaction. In addition, the vertical strain-field thickness relation examined in previous sections relation was not conform hypothesis and hence possibly effects figure 42. This may explain the rough increase in vertical strain with increasing A/t ratio as well. The observation of large A/t ratio and vertical strain (conform hypothesis) may additionally be dominated by the large degree of depletion of those particular fields rather than by the low A/t ratio. Depletion is hence interpreted to significantly effect vertical strain.

To confirm the difference between fields that have a low A/t ratio and low vertical strain and a small or large areal extent, large and small fields are separated in figure 43. The small field definition based on area is used, thus defining fields smaller than $1.2 \cdot 10^7\ m^2$ as small. From figure 43 can be observed that at low A/t ratios (<100 000 m) both small and large vertical strains occur, but all fields in this range are defined as small. At larger A/t ratios (>100 000 m), the majority of fields is defined as large and both low and high vertical strains occur. A subdivision between low A/t ratio-low vertical strain at small fields and low A/t ratio-high vertical strain at large fields (thereby able to accommodate more compaction) thus cannot be clearly distinguished.

Due to its small thickness and relatively large areal extend, the Tietjerksteradeel KNNS field is removed from figure 44, improving visibility of the results. The figure illustrates the total seismic moment versus the A/t ratio for 62 onshore gas fields. From this figure a weak trend of increasing seismic moment with increasing A/t ratio can be observed, which is not conform hypothesis. However due to the limited amount of seismic fields a trend is difficult to distinguish. Aseismic and aseismic fields are present in the whole A/t ratio range, thus no distinguishing capacity for seismicity can be seen and other parameters (e.g. porosity) are interpreted to influence vertical strain and total seismic moment as well.

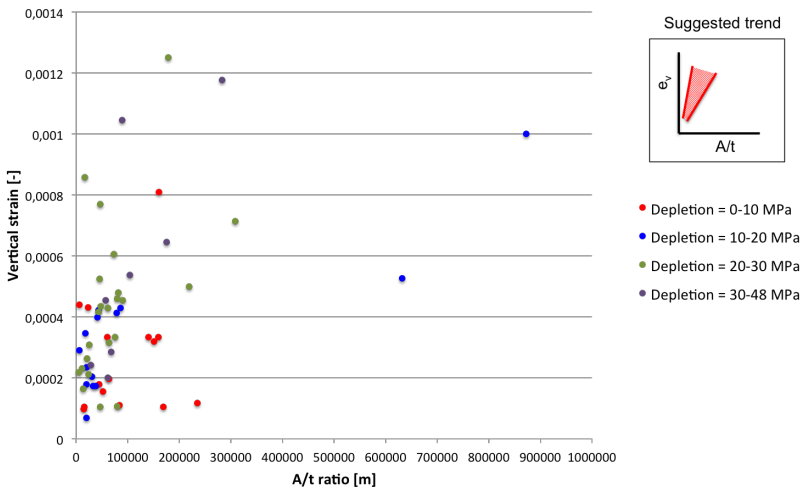

Figure 42: *Vertical strain versus A/t ratio for 60 onshore gas fields.*

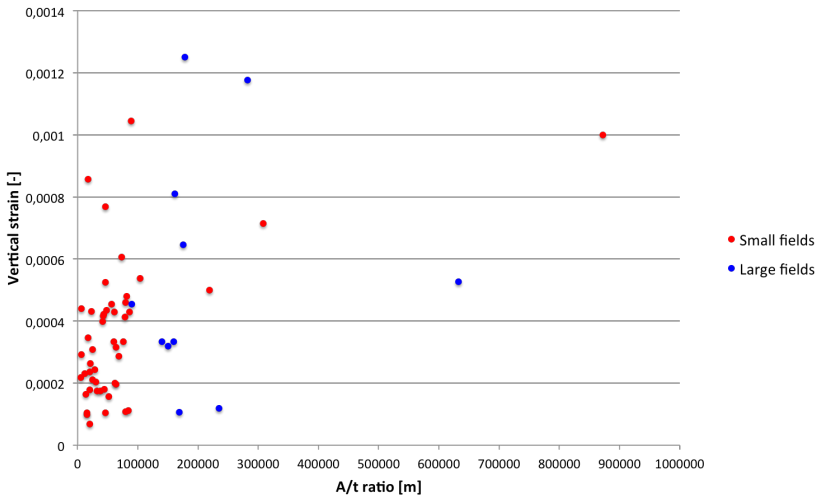

Figure 43: *Vertical strain versus A/t ratio for 60 onshore gas fields, subdivided on the basis of small and large fields.*

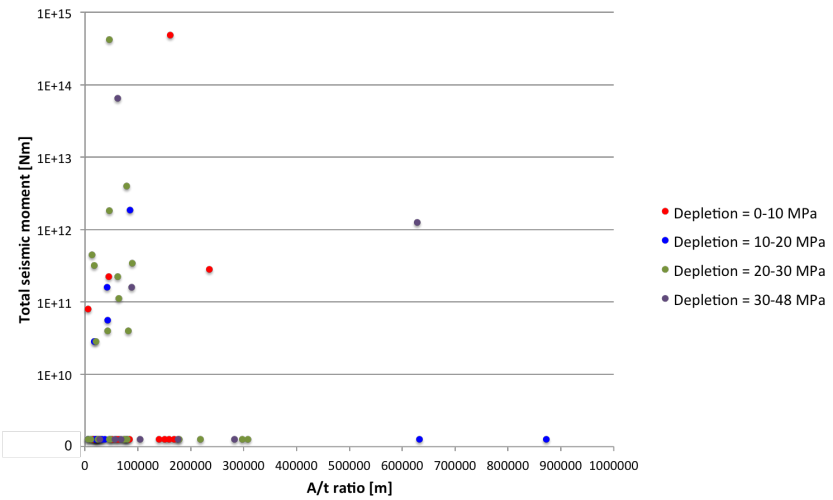

Figure 44: *Total seismic moment versus A/t ratio for 62 onshore gas fields.*

5.8 Correlation of Vertical Effective Stress, Compaction & Seismicity

Pore fluid exerts pore pressure that inhibits compaction, since the vertical stress on the reservoir is lowered by pore fluid pressure (equation 2). The effect of pore pressure depletion is discussed in the 'Depletion' subsection, yet other factors in equation 2 are density of the overburden and depth, varying per reservoir. This section determines the relation between vertical strain, seismicity and vertical effective stress, thus including P_f, overburden density and depth as variables. Initial and current (since the majority of fields is currently in production) vertical effective stress are hereby both plotted against vertical strain, total seismic moment and maximum seismic magnitude. It is expected that *an increase in current vertical effective stress on the reservoir top increases vertical strain and total seismic moment as well.*

Figure 45 illustrates the initial and current vertical effective stress versus the vertical strain for 63 onshore gas fields. The Tietjerksteradeel KNNS and RO fields are omitted from the dataset since it is not possible to determine whether the KNNS or RO field contributes to the observed strain. The fields that experienced a pore pressure depletion of zero MPa are eliminated from this section as well, since the observed surface subsidence above these fields is not caused by compaction in the fields itself, but due to compaction in neighboring fields. The initial vertical effective stress ranges from 13.9-44.0 MPa and the current vertical effective stress ranges from 18.0-80.1 MPa. From figure 45 a strong trend neither in the initial vertical stress nor in the current vertical stress versus strain can be observed. However, an increase in current vertical effective stress appears to increase the vertical strain. Stress-strain curves are further described in a following section.

From figure 46 it can be observed that roughly an increase in current vertical effective stress shows an increase in total seismic moment. The Roswinkel field lies out, having a rather small vertical effective stress relative to the other fields. No distinguishing capacity can be seen in initial and current vertical effective stress, since both seismic and aseismic fields

occur in the complete vertical effective stress ranges. Appendix 2 shows the maximum seismic magnitude versus the initial and current vertical effective stress.

As a complement to figure 7, where the initial gas pressure and depletion, i.e. ΔP_f, was illustrated versus the present depth of the reservoir top, figure 47 illustrates the initial and vertical effective stress versus present depth to reservoir top. The linear trend in especially the initial vertical effective stress appears since with an increasing depth the vertical effective stress also increases. However, the difference between the linear trend in the current vertical effective stress and initial vertical effective stress seems to increase with a higher present depth to reservoir top. In other words, generally the initial and current vertical effective stress can be observed to be non-parallel to each other. This may imply that with a larger present depth to the reservoir top ΔP_f increases, which is illustrated by figure 7 as well.

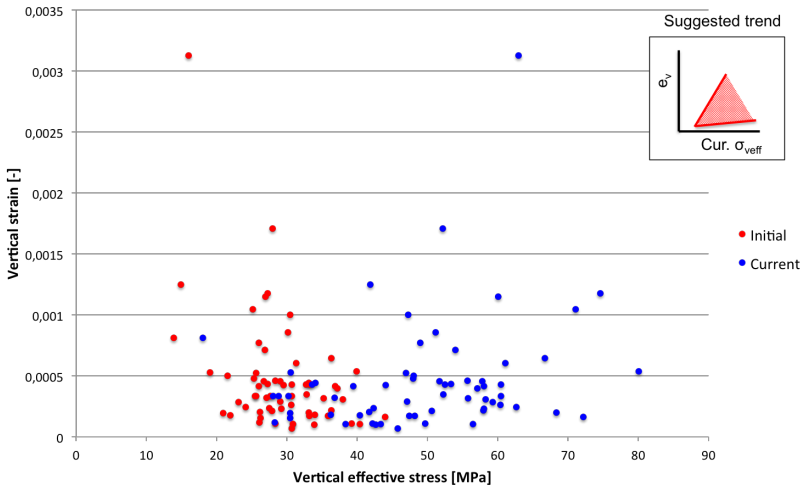

Figure 45: *Vertical strain versus the vertical effective stress (initial and current) of 63 onshore gas fields.*

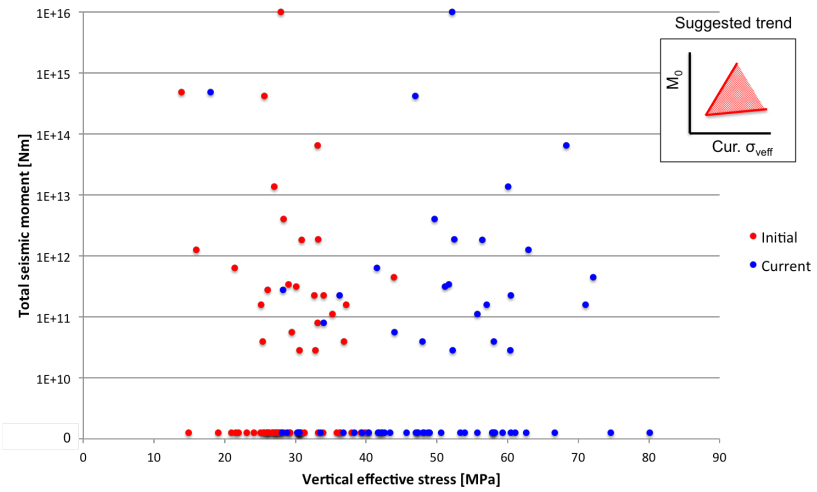

Figure 46: *Total seismic moment versus the vertical effective stress (initial and current) of 65 onshore gas fields.*

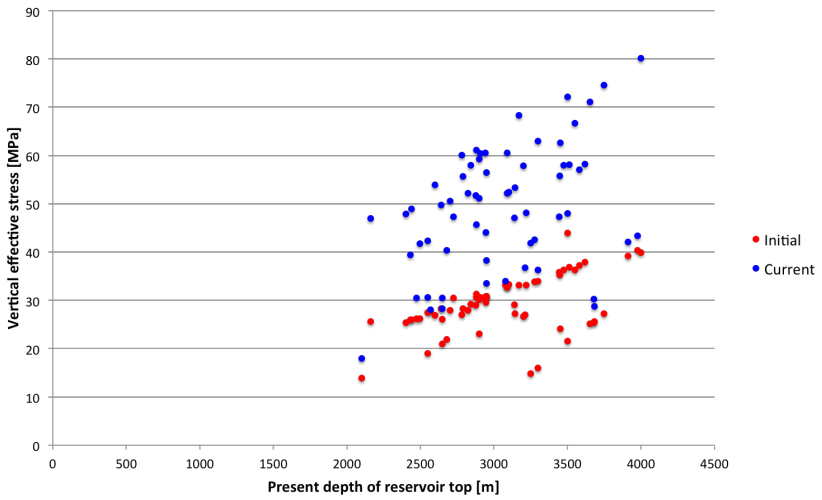

Figure 47: *Vertical effective stress (initial and current) versus present depth of reservoir top for 65 onshore gas fields.*

5.9 Correlation of Compaction Coefficient, Compaction & Seismicity

In this section the relation between vertical strain, total seismic moment, maximum seismic magnitude and compaction coefficient is determined. Since compaction coefficient gives the degree of compressibility as a material property, the hypothesis is that *the compaction coefficient is directly related to vertical strain, and hence compaction and induced seismic potential increase with increasing compaction coefficient.* Equation 3 relates the compaction coefficient to elastic modulus and Young's modulus, showing that the compaction coefficient is inversely related to the Young's modulus or stiffness. This implies that a small compaction coefficient gives a large stiffness and will therefore have the tendency to compact less, causing less vertical strain and thereby diminishing the seismic potential. A higher compaction coefficient is reached with a lower elastic modulus or stiffness, causing reservoirs to be more prone to compaction due to depletion. An increase both vertical strain and total seismic moment hence is expected.

The relation between vertical strain and compaction coefficient for 63 onshore gas fields, divided by amount of depletion in a field with pore pressure decline intervals of 0.1-10, 10-20, 20-30 and 30-48 MPa, is illustrated in figure 48. The compaction coefficient values range from 0.19 (Saaksum East and West fields) to 1.50 $\cdot 10^{-5} bar^{-1}$ (Roswinkel field). Most compaction coefficients can be observed to be between 0.40 and 0.70 $\cdot 10^{-5} bar^{-1}$, which is common for semi to well-consolidated sandstones with a mean porosity of 15 % at a depth of approximately 3000 m (Geertsma (1973)). A rough trend appears to be present conform hypothesis, where an increase in compaction coefficient causes an increase in vertical strain as well. The Roswinkel field has a high compaction coefficient compared to vertical strain. The high compaction coefficient may be interpreted to be related to production from the Main Buntsandstein Formation while most reservoirs of the 68 examined onshore gas fields are positioned in the Upper Rotliegend Group. A difference in reservoir formation may thus imply a difference in rock properties, thereby increasing or decreasing the compaction coefficient. Also other parameters may be involved, for example the relatively low depletion of the Roswinkel field. Since most reservoirs are positioned in the Rotliegend Group, material properties are likely to be similar, explaining the cluster of compaction coefficients between 0.40 and 0.70 $\cdot 10^{-5} bar^{-1}$.

Figure 49 illustrates the total seismic moment versus the compaction coefficient for 65 onshore gas fields, again divided by pore pressure decline intervals of 0.1-10, 10-20, 20-30 and 30-48 MPa. Roughly, increasing compaction coefficient causes an increase in total seismic moment. Since in almost the whole range of compaction coefficients (except for the two compaction coefficients <0.30 and >1.05) both seismic and aseismic fields occur, no distinguishing capacity can be observed. The interpretation is thus made that other parameters are needed to explain this behavior (e.g. geometry), and seismic potential cannot be determined solely on the compaction coefficient. The weak trend is interpreted to be conform expectation for both vertical strain total seismic magnitude.

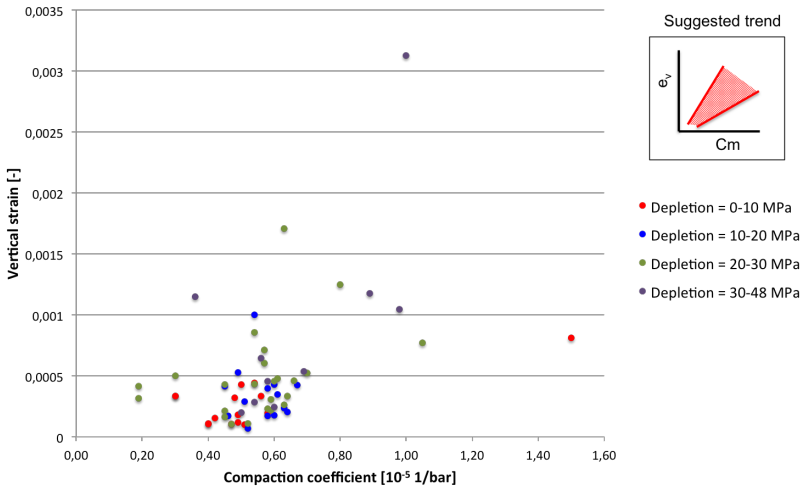

Figure 48: *Vertical strain versus the uniaxial compaction coefficient for 63 onshore gas fields.*

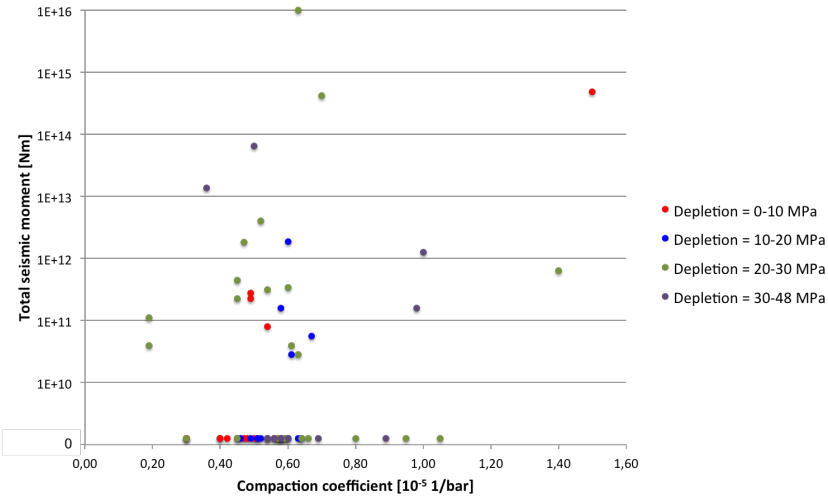

Figure 49: *Total seismic moment versus the uniaxial compaction coefficient for 65 onshore gas fields.*

5.10 Correlation of Zechstein Group Thickness, Compaction & Seismicity

The primary caprock for most of the 68 onshore gas fields is the Zechstein evaporite, which has a large influence on the overburden density calculations since evaporite density differs from the density of sandstones. The ductile nature of evaporites possibly influences the seismic potential and translation of compaction to the surface, which is discussed in this section. An important note is that the Zechstein caprock thicknesses are based on the thickness maps of the Zechstein Group. It is hereby assumed that the caprock thicknesses above the onshore gas fields can be determined sufficiently by using the Zechstein Group thicknesses, since the gas fields are examined *relative* to each other.

From figure 4 fields with larger vertical strains roughly appear to have a larger total induced seismic moment. However, several fields are present with a relatively high total seismic moment ($>\cdot 10^{12}$) and low vertical strain (<0.0005). The possibility arises that a large Zechstein thickness increases lateral movement of the overburden and thus gives a lower surface subsidence than actual compaction in the reservoir. The compaction in the reservoir is hence not completely translated to the surface. Additionally, as proposed in Hettema et al. (2000), the ductile Basal Zechstein could balance the stress path created by reservoir compaction and thereby the translation of reservoir compaction to the surface is not completely accurate. Marketos et al. (2015) describe induced ground motions below a producing reservoir, concluding that a larger surface subsidence is predicted as the evaporite layer is smaller.

Hence, for five fields that fall in the low vertical strain - high seismicity range it is determined whether this corresponds to a large Zechstein thickness in those particular fields. The five fields are: Appelscha, Eleveld, Roden (block 1), Roswinkel and Vries (Noord), with a Zechstein thickness of 800, 800, 1050, 1200 and 900 m, respectively. The Roswinkel field is overlain by Zechstein Group deposits, however the reservoir caprock is the Middle Triassic Sölling Claystone. All fields have a relatively large thickness of the Zechstein Group, which does not contradict that a large Zechstein thickness may change the translation of compaction in a reservoir to the surface. Nevertheless, due to the complexity of the problem also

other options need to be considered. For example, the mean thickness of the Zechstein Group in the northern Netherlands is relatively large, giving a mean value of approximately 900 m. Also, several fields are present with both a large Zechstein thickness and large vertical strains. At last, uncertainty regarding the accuracy of the strain data makes it difficult to confirm the hypothesis. A more likely scenario is hence that other parameters, such as geometry or porosity, explain the relation between vertical strain and induced seismicity.

From the hypothesis that *an increase in Zechstein thickness decreases surface subsidence* it is expected that vertical strain, calculated on the basis of surface subsidence, decreases within increasing Zechstein thickness as well. To illustrate this relation, figure 50 shows a plot of the vertical strain versus the thickness of the Zechstein Group for 63 onshore gas fields, divided per depletion interval. Although for all 68 gas fields examined in this study the thickness of the primary caprock is determined, this section only describes the gas fields that have the Zechstein Group either as a caprock, or as a unit positioned higher in stratigraphy. The reason for this is that when no expansion of the overburden (i.e. lateral movement) is present, the compaction in the reservoir is equal to the surface subsidence (Doornhof et al. (2006)). Thus, the presence of Zechstein evaporites is essential and the positioning as a caprock or a unit higher in stratigraphy is assumed to be of less relevance. Figure 50 illustrates a rough increase in vertical strain with an increase in the thickness of the Zechstein Group, which is not conform hypothesis.

Since creep of the ductile Zechstein may induce stress change near a pre-existing fault and the vertical margin of error of the locations of induced seismic events do not rule out the possibility of seismicity occurrence in the Zechstein Group, a hypothesis is proposed, where *an increase in Zechstein thickness increases total seismic moment.* Figure 51 illustrates the total seismic moment versus the thickness of the Zechstein Group. Seismicity appears to increase roughly with increasing Zechstein Group thickness. The Bergermeer field is notable, having a large seismic magnitude but small thickness of the superposed Zechstein Group (250 m). No distinguishing capacity for the thickness of the Zechstein Group in terms of seismic or aseismic fields can be observed.

For both vertical strain and total seismic moment a rough increase appears with increasing Zechstein Group thickness. This relation may be attributed to other factors. For example, an increase in Zechstein Group thickness may represent an increase in accommodation space, which may have been present during the deposition of the underlying Rotliegend as well. This geological interpretation implies that an increase of Zechstein Group thickness may represent an increase of Rotliegend thickness well, which from literature, can accommodate more compaction compared to thin reservoirs.

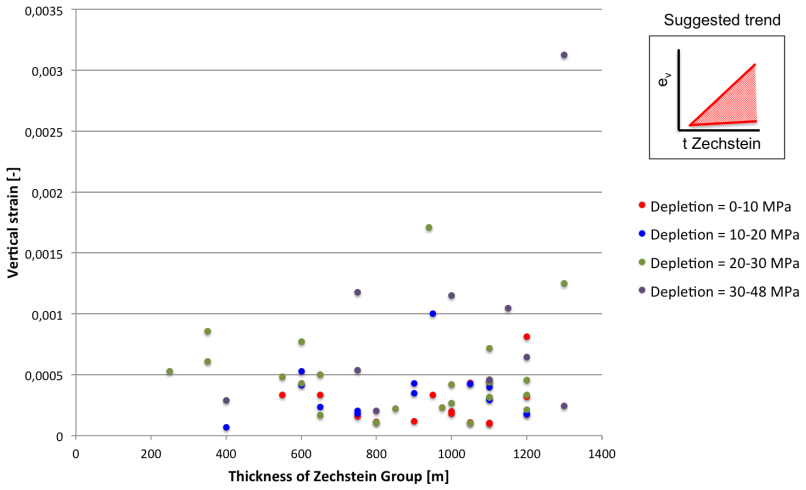

Figure 50: *Vertical strain versus Zechstein Group thickness for 63 onshore gas fields.*

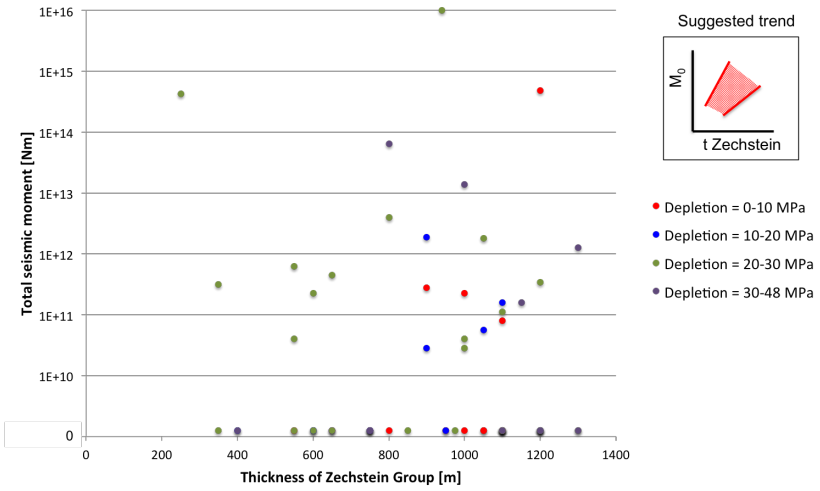

Figure 51: *Total seismic moment versus Zechstein Group thickness for 65 onshore gas fields.*

5.11 Seismicity near Fault Zones

To determine whether seismicity occurs near fault zones, recent seismicity data and structural map overlays in Google Earth are used (KNMI (2015); NLOG (2005)). The seismicity data has a lateral uncertainty of 500 m (NAM (2013)) and the vertical location contains a large uncertainty of 1-2 km. This imposes a high uncertainty, since it is not definite if the seismicity actually occurs in the reservoir. The analysis whether seismicity occurs near fault zones can however laterally be defined. A distance of the seismicity occurrence of 500 m is defined as 'near' a fault zone. Another uncertainty occurs due to the fact that the faults on structural maps are interpreted from seismic profiles; smaller-scale faults could be present and not be interpreted. The hypothesis is that *seismicity occurs near a fault zone, since the fault accommodates seismogenic slip.* All seismic fields had an occurrence of seismicity within 500 m of a fault zone. Only one field illustrates data disconform hypothesis; the Metslawier field. The seismicity in the Metslawier field is actually 770 m from a fault zone and thus falls outside the 500 m distance. This may be due to uninterpreted faults that were not (clearly) visible on seismic or due to the lateral uncertainty of the location of seismic events. It can be possible however that the reason a fault cannot be interpreted on seismic is that the fault itself is to small and maybe not significant enough to induce seismicity. Considering only one seismic field was not located 'near' a fault zone, it is interpreted that in general in seismic fields the seismic events are located near fault zones.

5.12 Field Data Correlation Summary

This section illustrates a visual summary of the field data correlation, listing all parameters and their correlation with vertical strain, total seismic moment, porosity and depth. Green, yellow and red present good, moderate and no correlation, respectively.

Table 5: *A summary of the field data correlation.*

Parameter	Correlation											
	ϵ_v			M_o			ϕ			d		
Vertical strain												
Depletion												
Porosity												
Temperature												
Current Production Time												
(Burial) depth												
Length/Width												
Thickness												
Length/Thickness												
Length/Depth												
Width												
Width/Thickness												
Area												
Volume												
Area/Thickness												
Vertical effective stress												
Compaction coefficient												
Zechstein thickness												

Good correlation
Moderate correlation
No correlation

6 Results & Discussion - Stress-Strain Curves

This section describes the stress-strain curves that can be obtained from field data. Both current vertical effective stress and the change in pore fluid pressure, i.e. ΔP_f, are plotted with vertical strain. The ΔP_f is equal to the loading in uniaxial compaction experiments and is therefore important to eventually make a comparison between lab experiments and field data. All stress-strain curves represent 63 onshore gas fields, with the Tietjerksteradeel KNNS, Tietjerksteradeel RO, Ameland-Noord, Lauwersoog-C and Vierhuizen-Oost fields eliminated. To determine whether gas fields show a linear or non-linear relation for certain parameters, data is subdivided by seismicity, porosity, depth and location of the examined gas fields. Non-linearity in a stress-strain curve could imply that a relatively small stress change generates a significantly larger change in strain. The stress-strain curves without subdivision are illustrated in figure 52 and 53. An increase in current vertical effective stress and ΔP_f appears to roughly increase the vertical strain. Non-linearity may roughly be observed from a yield point of $\Delta P_f =$ 25 MPa, yet this relation is difficult to determine since the stress-strain curve data is relatively scattered. The results for computing current vertical effective stress and ΔP_f are similar. This can be explained considering vertical effective stress is partly dependent on ΔP_f (equation 2).

A general yield point seems to be present at a depletion (ΔP_f) of approximately 25 MPa

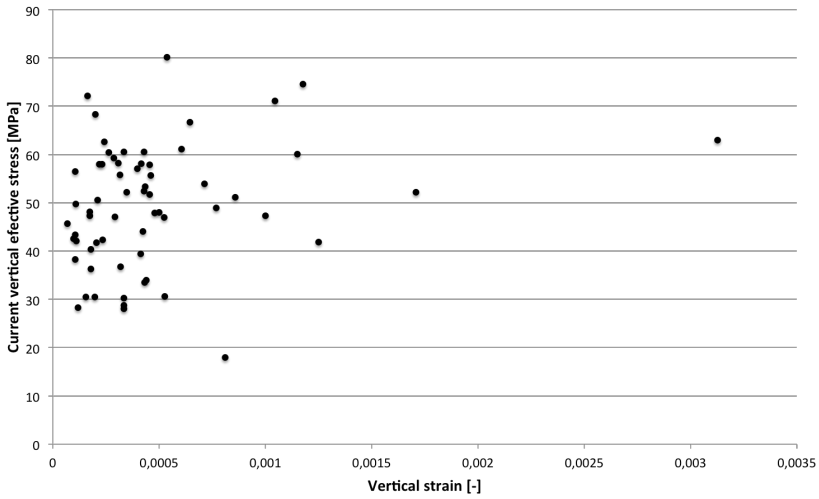

Figure 52: *Current vertical effective stress versus vertical strain for 63 onshore gas fields.*

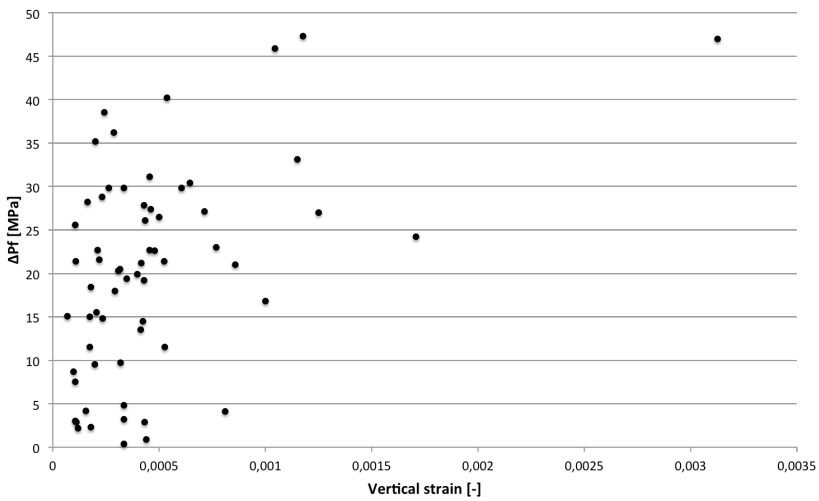

Figure 53: ΔP_f *versus vertical strain for 63 onshore gas fields.*

6.1 Subdivision by Total Seismic Moment

To further examine the relation between current vertical effective stress, degree of depletion and vertical strain, the data illustrated in figure 52 and 53 is subdivided by total seismic moment. The subdivision includes: aseismic fields and fields with a total seismic moment of $\cdot 10^{10/11}$, $\cdot 10^{12/13}$ and $> \cdot 10^{14}$ Nm, resulting in figure 54 and figure 55. The total seismic

moments approximately coincide with maximum seismic magnitudes of 0.9-2.0, 2.0-3.0 and 3.0-3.6 on the Richter scale, resulting in figure 91 and 92 in appendix 2. For current vertical effective stress and especially ΔP_f, fields that are aseismic appear to be clustered in a low-strain range (<0.0005) compared to seismic fields. Spread appears to be larger looking at seismic fields than in the aseismic fields. It can also be seen that highly seismic fields, with a total seismic magnitude larger than $\cdot 10^{14}$ do not necessarily have the largest strains.

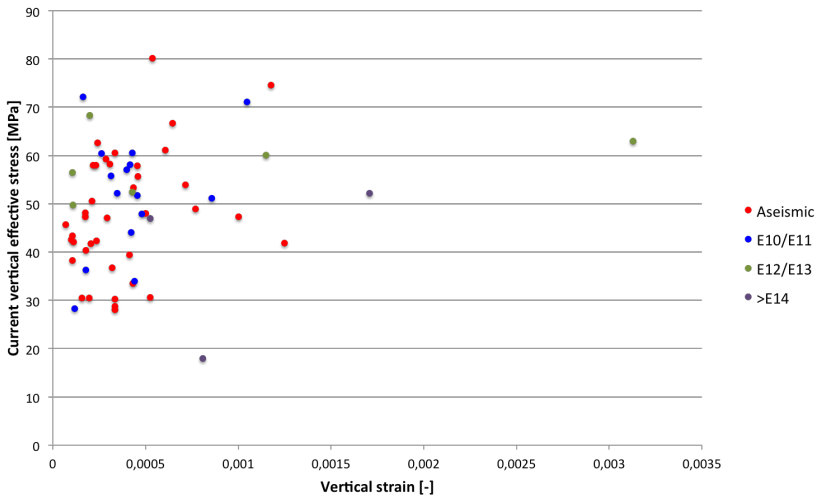

Figure 54: *Current vertical effective stress versus vertical strain for 63 onshore gas fields, subdivided by total seismic moment interval.*

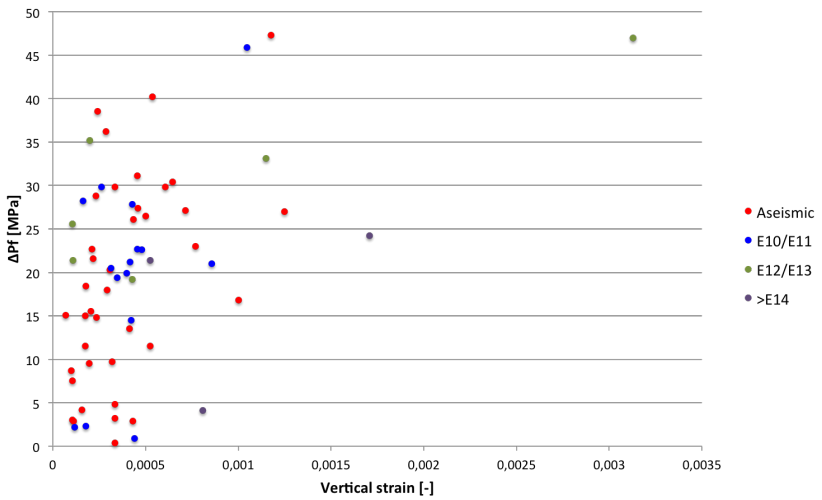

Figure 55: ΔP_f *versus vertical strain for 63 onshore gas fields, subdivided by total seismic moment interval.*

6.2 Subdivision by Porosity

Figure 56 and 57 illustrate the current vertical effective stress and ΔP_f, divided into porosity intervals of 9-12, 12-15, 15-17, 17-19 and 19-23 %. Larger porosity intervals, i.e. 17-19 and 19-23 % and to a lesser extend 15-17 %, illustrate a higher degree of non-linearity comparing to lower porosities. The relation is however not completely conclusive, since no perfectly non-linear or linear behavior can be seen.

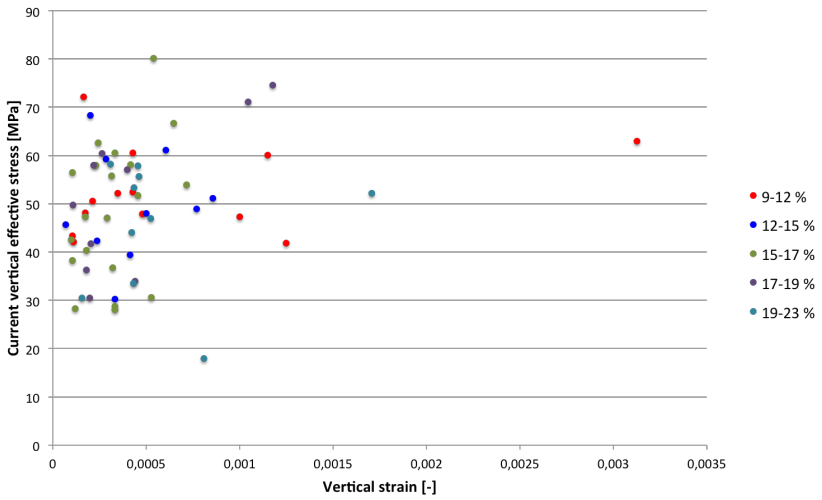

Figure 56: *Current vertical effective stress versus vertical strain for 63 onshore gas fields, subdivided by porosity interval.*

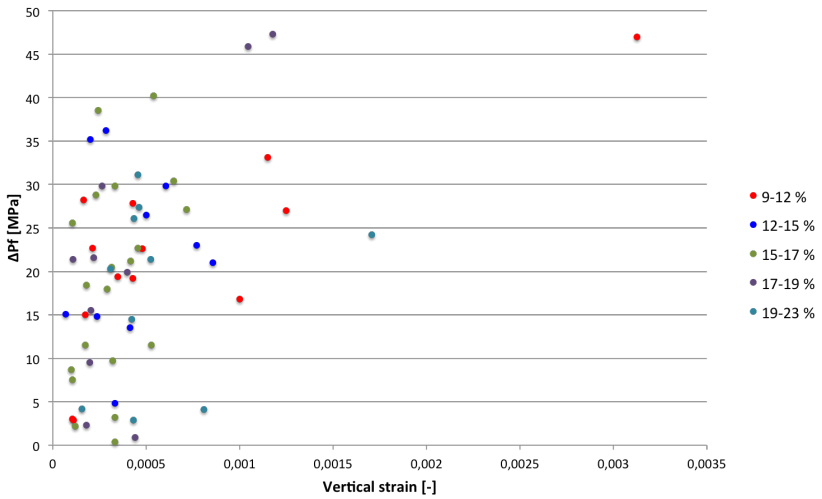

Figure 57: ΔP_f *versus vertical strain for 63 onshore gas fields, subdivided by porosity interval.*

6.3 Subdivision by Depth

Current vertical effective stress and ΔP_f are illustrated versus vertical strain and subdivided into present reservoir depths of 2000-2500, 2500-3000, 3000-3500 and 3500-4000 m in figure 58 and 59. Once more it is complicated to observe a general trend. Some non-linearity appears to occur in al depth ranges at increasing vertical strain, where the depth range of 3000-3500 m appears to have a lower degree of non-linearity compared to a depth range of 3500-4000 m.

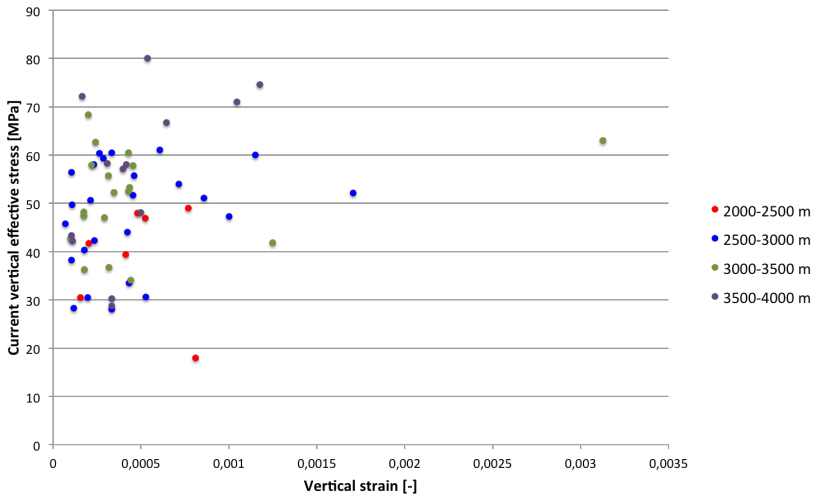

Figure 58: *Current vertical effective stress versus vertical strain for 63 onshore gas fields, subdivided by depth interval.*

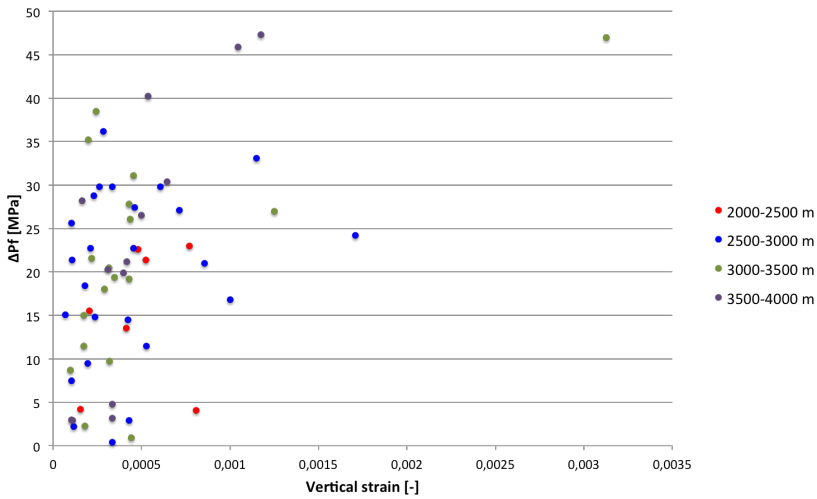

Figure 59: ΔP_f *versus vertical strain for 63 onshore gas fields, subdivided by depth interval.*

6.4 Subdivision by Location - Adjacent Field Proximity

Strain in one field can possibly be influenced by strain in another, larger and laterally extensive field with a length versus width ratio close to 1, providing a large subsidence bowl. It is thus expected that *clusters can be observed of fields that are located in a similar area.* To examine this hypothesis, the current vertical effective stress and ΔP_f versus strain curves are subdivided by area. Several areas are taken in this separation, namely the Groningen area (Groningen Platform), the Friesland area (Friesland Platform and Lauwerszee Trough/Ameland Platform) and the Drenthe area (Lower Saxony Basin). The Bergermeer field in the Central Netherlands Basin is not taken into account due to limited data availability. The relation between vertical effective stress and vertical strain per area is illustrated in figure 60. The relation between ΔP_f and vertical strain per area is illustrated in figure 61. A roughly linear relation appears to be present in both figures for the Friesland Platform and Lower Saxony Basin areas. The Groningen Platform and Ameland Platform/Lauwerszee Trough areas both illustrate rough non-linearity, with yield points of approximately 24 and 42 MPa in figure 61. The Groningen Platform data hence appears to become non-linear in an earlier stage of depletion compared to the Ameland Platform/Lauwerszee Trough data. Clustering of fields cannot be evidently observed.

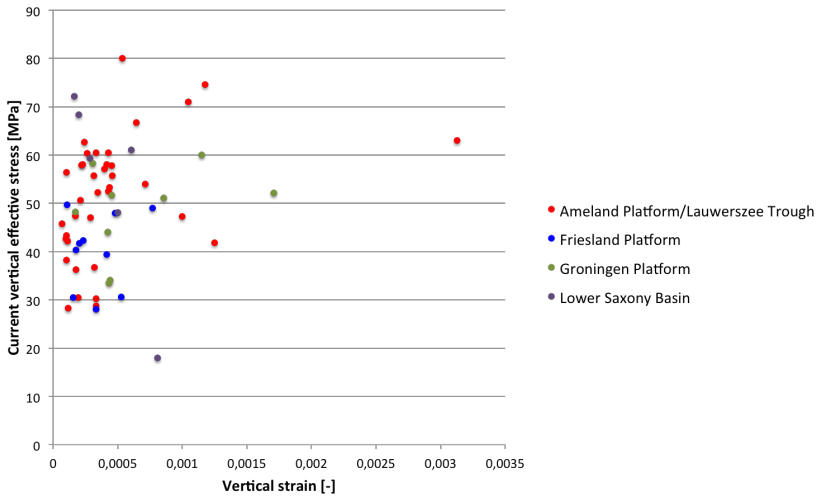

Figure 60: *Current vertical effective stress versus vertical strain for 62 onshore gas fields, subdivided by area.*

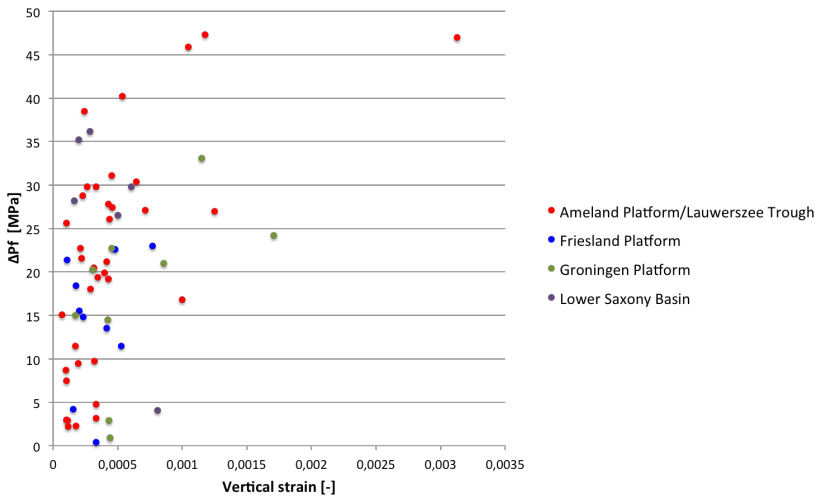

Figure 61: ΔP_f *versus vertical strain for 62 onshore gas fields, subdivided by area.*

7 Laboratory Experiments versus Field Data

This section considers the comparison between field data involved in this study to laboratory data from a recent study by Hol et al. (2015), that experimentally considers the long-term reservoir compaction generated by depletion for Permian sandstones. The uniaxial pore pressure depletion (UPPD) experiments performed in Hol et al. (2015) are assumed to approach the conditions occurring during field depletion, as uniaxial strain conditions are simulated. The purpose of this section is to acquire new insights in the translation between laboratory and field data, as this is essential for an accurate prediction of reservoir compaction.

7.1 Data Comparison

To compare the laboratory data from Hol et al. (2015) to the field data acquired in this study properly, multiple aspects must be considered, e.g. magnitude of depletion, duration of depletion, axial strain, porosity, compaction coefficient and scale.

Looking at the magnitudes of depletion in the laboratory experiments of Hol et al. (2015), UPPD experiments were performed from the reservoir pressure before production (57 MPa) to the maximum depletion (3 MPa), resulting in a ΔP_f range of 0-54 MPa. The field data represent reservoirs that were produced to a depletion, i.e. ΔP_f, of 47.3 MPa. The maximum depletion in the laboratory experiments is hence somewhat higher than the maximum depletion as seen in the field data.

Considering the duration of depletion, naturally the reservoirs considered in the field data are depleted on a much larger time-scale, namely from 0 to 52 years. The depletion in the UPPD tests of Hol et al. (2015) is relatively long-term, with a depletion of 87 hours from in-situ conditions, followed by a creep stage where no further depletion was executed.

Continuing with axial strain magnitude, from in-situ conditions to full depletion and creep stage in the laboratory experiments conducted by Hol et al. (2015) a strain increase of 0.76 % can be observed. The field data of 63 onshore gas fields illustrate a vertical strain range of 0.0069 to 0.31 %. The total strain increase from initial to current depletion is hence 0.0069 to 0.31 %. Comparing the increase in strain due to depletion in laboratory experiments and field data, the increase in strain of 0.76 % in the laboratory experiments is approximately twice as large as the maximum strain increase of 0.31 in the field data. Considering the mean vertical strain increase in the field data of 0.047 %, this value is an order of magnitude smaller than the strain increase in the laboratory experiments.

Hol et al. (2015) illustrate the general stress-path of several UPPD experiments, wherefrom the amount of depletion versus the axial strain using laboratory data can be observed. Plots illustrating ΔP_f versus vertical strain of field data for 63 onshore gas fields are presented in figure 53. These data are illustrated together with the data of one UPPD experiment from Hol et al. (2015) in figure 62. The increase in axial strain with increasing depletion can be observed to be less in the field data. The yield point, indicating non-linearity, appears to be at a lower ΔP_f but less clear in the field data compared to the laboratory data (yield point at $\Delta P_f = 54$ MPa) due to the high degree of scatter in the field data.

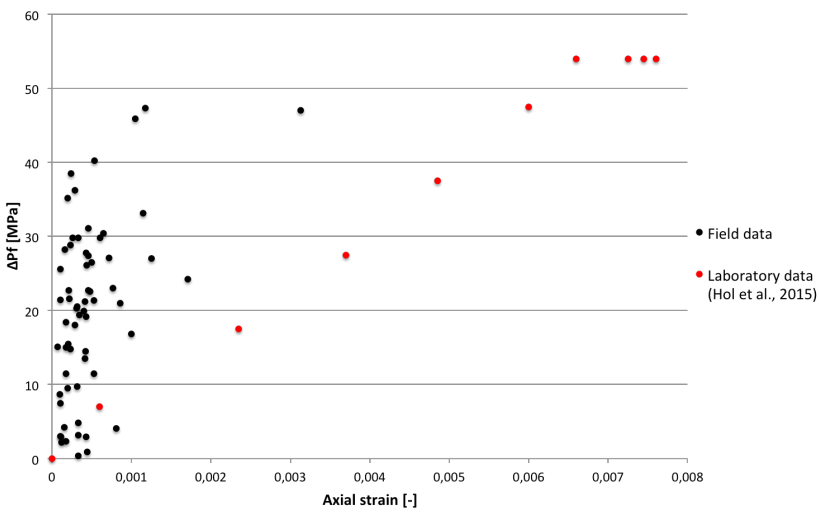

Figure 62: *ΔP_f versus vertical strain for field data of 63 onshore gas fields (black dots) and for an UPPD test performed in Hol et al. (2015) (red dots).*

Figure 63 compares compressibility, i.e. compaction coefficient, and porosity data from field and laboratory. The laboratory data from Hol et al. (2015) are used, representing ΔP_f ranges of 0-10 (low depletion) and 50-54 MPa (high depletion). In order to compare these experimental data with field data, compaction coefficient versus porosity is required for field data in the same ΔP_f ranges as well. However, no fields occur with a ΔP_f between 50 and 54 MPa in the field data

of 63 onshore gas fields (excluding the Tietjerksterdadeel RO, Tietjerksteradeel KNNS, Vierhuizen-Oost, Ameland-Noord and Lauwersoog-C fields). To yet compare the data in the large ΔP_f ranges, the range is extended to 33-54 MPa (high depletion).

Hol et al. (2015) describe two main observations of the laboratory data, namely 1) A reduction in uniaxial compressibility occurs when a large amount of depletion is realized and 2) At a large depletion, an increase in porosity shows an increase in uniaxial compressibility. Focusing on the first observation of Hol et al. (2015), the field data illustrate an increase of the uniaxial compressibility at a high amount of depletion. The second observation of Hol et al. (2015) however coincides with the field data, since at a high depletion a positive linear relation can be observed between uniaxial compressibility and porosity. The magnitudes of uniaxial compressibility and porosity are compared as well. Both uniaxial compressibility and porosity values can be observed to be larger in the laboratory data than in the field data. The porosity and uniaxial compressibility ranges in the samples of Hol et al. (2015) are approximately 0.14 to 0.27 and 0.44 to $1.3 \cdot 10^{-10}\text{Pa}^{-1}$ respectively, while the mean values in the field data are on the low side of these ranges (mean porosity is 0.15 and mean compressibility is 0.55 $1.3 \cdot 10^{-10}\text{Pa}^{-1}$ for the fields in figure 63).

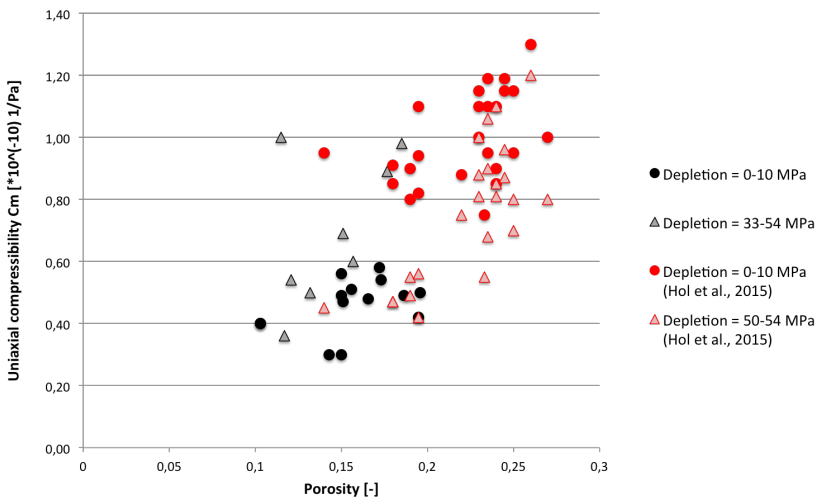

Figure 63: *Uniaxial compressibility versus porosity adapted from Hol et al. (2015) and from field data of 63 onshore gas fields for ΔP_f of 0-10 MPa, 33-54 MPa (field data) and 50-54 MPa (laboratory data).*

Lastly focusing on scale, the difference is evident. Triaxial and UPPD tests in Hol et al. (2015) were conducted on a core sample from the Nes field, which was included in the field study as well. Thus, the laboratory experiments focus on small-scale detailed strain response to change in stress, while the field data focuses on large-scale fields at different locations and depths. The field data acquisition required to average the information from all wells in one field, whereby sparse sampling density results in inevitable uncertainty. The averaged reservoir data is however assumed to be representative for the field. To apply the experimental results to the field-scale, upscaling is required. Hol et al. (2015) performs upscaling of the experimental data to the field scale by calculating the total shortening of a reservoir, using $\Delta L = \varepsilon_{total} \cdot L_0$ whereby the total average strains are 0.4 % to 1.2 % for a 20 to 60 cm compaction of a 50 m reservoir. The surface subsidence is considered 0 to 40 cm locally and thus it is concluded that the upscaling of experimental results is representative for the surface subsidence (Hol et al. (2015)). Looking into the field data, two different depleting thicknesses for the Nes field can be found, namely 40 m (Winningsplan Moddergat, Lauwersoog en Vierhuizen (2011)) and 105 m (NAM (2010)). ΔL for these different reservoir thicknesses are computed in table 6. The resulting reservoir shortening ranges from 16 to 126 cm, which is a relatively large amount compared to the average surface subsidence of 5.3 cm of 63 onshore gas fields examined in this study (excluding the gas fields with no depletion and the Tietjerksteradeel RO and KNNS fields). Looking at the Nes field specifically the surface subsidence in 2008 was 3.5 cm (NAM (2010)) and the prognosis for the period of 2011-2050 is a surface subsidence of 14 cm (Winningsplan Moddergat, Lauwersoog en Vierhuizen (2011)). Hence, experimental data results in slightly larger values of reservoir shortening compared to surface subsidence measured in the field.

Table 6: *ΔL values in cm for different total average strains and reservoir thicknesses.*

		L_0 [m]		
		40	50	105
ε_{total} [-]	0.004	16	20	42
	0.012	48	60	126

7.2 Data Interpretation

The observations that 1) axial strain magnitude after depletion is larger in laboratory data compared to field data and 2) the field data illustrates a smaller increase in strain with an equal increase in depletion compared to laboratory data, may suggest that predicted subsidence based on lab data is overestimated.

Hettema et al. (2000) explains this discrepancy in terms of stress path ($\gamma = \Delta\sigma_H/\Delta P_f$). Laboratory experiments indicate a large influence of stress path on compaction due to depletion (Hettema et al. (2000)). Hettema et al. (2000) focuses on the difference in laboratory (uniaxial compaction experiments) and field stress paths of the Groningen field specifically. The stress path determined from uniaxial laboratory experiments is approximately twice as large than the stress path in the field for the Groningen gas field, increasing compressibility (Hettema et al. (2000)). Hettema et al. (2000) proposes two explanations for this observation. Firstly, the occurrence of frictional sliding along normal faults near the field may result in a higher stress path in uniaxial experiments compared to the reservoir field data. Secondly, the occurrence of thick Zechstein caprock may explain the difference in stress path of laboratory experiments versus field data, since the ductile Zechstein balances the stress changes in the field (Breckels and Van Eekelen (1982); Hettema et al. (2000)). Both stress-redistribution of Zechstein caprock and the occurrence of frictional sliding along normal faults are not taken into account in uniaxial laboratory experiments and may therefore be a plausible explanation for the observed differences.

The temporal delay in translation between depletion of a field and the subsidence at the surface as described by Hettema et al. (2002) is important to keep in mind as well. The possibility occurs that due to this delay, the current surface subsidence does not yet represent compaction in the reservoir. As no surface subsidence values over time are available in this study, this effect is not assessed.

The above may explain the larger axial strain magnitude after depletion in laboratory experiments compared to field data. Yet, the discrepancy between laboratory and field data is explained by looking from a field perspective. Mechanisms operating on micro-scale in laboratory experiments, such as localized deformation, decreasing horizontal stress and increasing the stress path, may provide an explanation for the larger stress path in laboratory experiments as the radial strains are measured only in the center of the sample in the UPPD experiments described in Hol et al. (2015).

The laboratory experiments and the field data in figure 63 illustrate contrasting results. The observation is that in the laboratory data a low compressibility occurs at a large ΔP_f while in the field data a large ΔP_f shows a high uniaxial compressibility as well. Larger compressibility values in the field data at a large ΔP_f (33-54 MPa) compared to a small ΔP_f (0-10 MPa) may be explained since high-compressibility reservoir rocks are less stiff and may compact more during production compared to low-compressibility reservoir rocks. This possibly results compaction drive in high-compressibility fields, ultimately leading to large magnitudes of depletion. The laboratory experiments represent uniaxial compressibility values throughout the experiment (for a low and high depletion) per sample for multiple samples. During the experiment compressibility decreases at larger ΔP_f (50-54 MPa compared to 0-10 MPa). Comparison between the experimental and field data is not possible on the basis on compressibility, since the laboratory experiments illustrate the change in compressibility during depletion, while the field data illustrates compressibility values per field for different amounts of depletion. In the laboratory experiments as well as in the field data a rough positive linear relation between compressibility and porosity is observed at a large depletion. Due to the inverse relation of uniaxial compressibility and stiffness, a high uniaxial compressibility is expected at a large porosity, as the rock is less stiff.

Additionally, the difference in magnitude of both the uniaxial compressibility and porosity makes it difficult to compare the results, since the laboratory data span a range that is much larger than compressibility and porosity ranges of field data. It can be concluded that although comparing laboratory experiments with the field data in this study is difficult, the increase in vertical strain magnitude during depletion is significantly larger in laboratory experiments compared to the field data. During upscaling of laboratory results it is important to keep this discrepancy beween laboratory and field data in mind.

8 Theoretical Model - Reservoir Bending During Depletion

The 'Results and Discussion' sections for both the field data correlation and stress-strain curves covers many aspects regarding the parameters or reservoir characteristics examined in this study. Most interpretations consider rough trends, and for several examined field characteristics the interpretation was made that other parameters must be involved. Since most reservoir parameters are influenced by each other as well, correlating field data is complicated and uncertainties occur. Ergo, it is desirable to approach the problem from a different perspective. The purpose of this section is to make a simple model for the behavior of a caprock and reservoir during depletion, thereby testing field geometry hypotheses. The main focus will be on the ratio between length and width (L/W ratio), as this geometry hypothesis appeared to correlate relatively well in section 5.7.1.

Although assumptions will be necessary, it is thought that a simple analytical model is able to comprise the main mechanisms and thus provides knowledge that will help solving the main problems in this study, namely: *1) Can subsidence and hence ultimately seismic potential of Dutch onshore gas fields be correlated with and understood from field data?, and 2) Is there any predictive potential from such an approach?.*

Similar to the method used in Hangx et al. (2010) it is attempted to calculate the changes in stress during depletion. The mechanics of a bending beam fixed on both sides and an ellipse, clamped or fixed at all edges, are used as an analogue for a caprock or reservoir. The beam configuration is incorporated only to understand the bending mechanism; since this geometry is fixed at 2 sides only, a geometry that is fixed on all sides must be examined as well. The clamped ellipse configuration is most likely to approximate an actual reservoir or caprock, where the clamped edges represent the fault-bounding edges of the reservoir or caprock. A rectangular plate, fixed on all sides, was considered as well. This configuration however provided difficulties at the edges and no equation for amount of deflection and bending stress at a certain location in the rectangular plate for varying Poisson's ratios is provided (Imrak and Gerdemeli (2007); Young and Budynas (2002)).

It is expected that during depletion, i.e. the lowering of the pore fluid pressure, gradual compaction occurs in a reservoir. The caprock response to the depletion is bending and the incremental top part of the depleting reservoir is assumed to bend as well. As the vertical uncertainty of the seismicity occurrence is 1-2 km, both caprock and reservoir may contribute to the seismic potential of a field. Hence, the stress changes are calculated for the caprock and reservoir.

Several steps are necessary in order to determine a theoretical model for stress change in a depleting reservoir and caprock due to bending. The main focus is on horizontal stress change, since both Hangx et al. (2010) and Hettema et al. (2000) indicate that the vertical stress change in a depleting and/or bending reservoir is minor. An equation relating deflection in a beam and ellipse to force exerted on these configurations is determined first. From this equation the expected force exerted on a reservoir or caprock can be calculated, since the field data provides information about mean subsidence values. Secondly, equations are determined for the horizontal stress and shear stress change at the end of the beam as a function of depth in the beam. The importance of shear and horizontal stress can subsequently be examined by investigating the magnitude and orientation of both stresses. The development of shear and horizontal stress as a function of depth in the beam can thus be computed.

In the elliptical plate configuration equations for horizontal stress are provided for several locations. Additionally, it is crucial to determine the magnitude of total shear and horizontal stress, assuming a normal regime before production. The stress changes due to compaction of a field will be assessed separately. At last, a Mohr envelope involving the failure criterion of anhydrite (caprock) and sandstone (reservoir) is determined from literature. Following the steps above, an attempt is made to determine whether a fault can be reactivated assisted by a certain geometry and thus whether a certain geometry generates a larger seismic potential. From the sections covering field data correlation two main hypotheses are inferred, which are attempted to be examined: *1) A L/W ratio close to one gives a larger deflection at a constant force compared to a larger L/W ratio ($\sim >5$) and 2) A larger deflection at a L/W ratio close to one thus increases the horizontal stress change.*

8.1 Beam - Model Configuration and Assumptions

Young and Budynas (2002) describe the behavior of straight beams that are stressed elastically, from which several starting formulas are adopted. These formulas, based on assumption 1-12 (adopted from Young and Budynas (2002)), are listed in table 7. Two beam configurations are examined, namely 1) both ends fixed with a concentrated load (i.e. point load in the middle) and 2) both ends fixed with an uniform load. The fixed ends of a beam represent faults, bounding the reservoir or caprock at both sides. Table 8 illustrates the different symbols used in the equations involved in the model, which is based on the following assumptions:

1) The beam is homogeneous, thereby having an equal elastic modulus in both tension and compression.
2) The beam is initially straight.
3) The cross-section of the beam is uniform in all directions.
4) A minimum of one longitudinal plane of symmetry is present in the beam.
5) The loads and reactions exerted on the beam are positioned in the longitudinal plane of symmetry, perpendicular to

the beam's axis.
6) The beam is significantly long compared to its thickness.
7) The width of the beam is not disproportional.
8) The stress which is maximally applied does not surpass the proportional limit of the beam.
9) The in-situ stress regime is normal.
10) Bending of the incremental top part of a reservoir occurs.
11) Both longitudinal fiber stress (σ) and longitudinal shear stress (τ) are uniform along the width of the beam.
12) The fixed beam ends represent impermeable faults.

An important side note is necessary considering assumption 7. In order to determine whether a certain geometry is assisted by a larger seismic potential, reservoir width variation is required, as presumably length versus width ratio may be a dominant factor in determining seismic potential. Young and Budynas (2002) state that as consequence of a disproportional beam width a stiffening effect occurs. The formulas for deflection (table 7) hence need adjustment, where the elastic modulus, E, is replaced by $\frac{E}{(1-v^2)}$ to take the stiffening effect into account. Following NAM (2013), the Upper Rotliegend and Zechstein Group have a Poisson's ratio of 0.20 and 0.25, respectively. Even though Young and Budynas (2002) does not specify disproportionality, the stiffening effect is assumed to be small and hence negligible. Another side note regarding assumption 12 is that assuming the fixed beam ends represent impermeable faults is necessary, since this ascertains that no pore pressure depletion occurs outside the reservoir, represented as a beam. Assuming that the reservoir is isotropic and homogeneous implies that a stress rotation during depletion is not anticipated. Lastly it is assumed, as in Roest and Kuilman (1994), that tectonic stresses and induced seismicity due to salt activity can be disregarded.

From Young and Budynas (2002) it is adopted that two stress types are applicable at any point in the beam, namely the longitudinal fiber stress, σ, and the longitudinal shear stress, τ. Equations for both stresses are

$$\sigma = -\frac{My}{I} \tag{6}$$

where M represents the bending moment in the point of interest, y the vertical distance from the neutral axis to the point of interest, I is the moment of inertia, and

$$\tau = \frac{VA'\bar{y}}{Ib} \tag{7}$$

where V is the vertical shear at the section of the point of interest, A' is the cross-sectional area above or below the point of interest to the outer side of the beam, $\bar{y}$ is the distance from the centroid of A' to the neutral axis and b is the breadth, i.e. width, of the section.

Table 7: *Starting formulas adopted from Young and Budynas (2002).*

Beam configuration	Representation	Starting formulas
Concentrated load	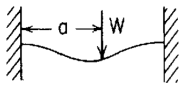	$y_{max} = \frac{-Wl^3}{192EI}$ when $a = \frac{1}{2}l$ $V = R_A - W\langle x-a\rangle^0$ $M = M_A + R_A x - W\langle x-a\rangle$ $R_A = \frac{W}{l^3}(l-a)^2(l+2a)$ $M_A = \frac{-Wa}{l^2}(l-a)^2$
Uniform load	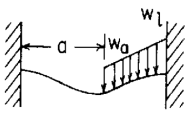	$y_{max} = \frac{-w_a l^4}{384EI}$ when $x = \frac{1}{2}l$ $V = R_A - w_a\langle x-a\rangle - \frac{w_l - w_a}{2(l-a)}\langle x-a\rangle^2$ $M = M_A + R_A x - \frac{w_a}{2}\langle x-a\rangle^2 - \frac{w_l-w_a}{6(l-a)}\langle x-a\rangle^3$ $R_A = \frac{w_a}{2l^3}(l-a)^3(1+a) + \frac{w_l-w_a}{20l^3}(1-a)^3(3l+2a)$ $M_A = \frac{-w_a}{12l^2}(l-a)^3(l+3a) - \frac{w_l-w_a}{60l^2}(l-a)^3(2l+3a)$

Table 8: *Symbols used in starting formulas adopted from Young and Budynas (2002).*

Symbol	Description	Unit
E	Elasic or Young's modulus	Pa
v	Poisson's ratio	-
σ	Longitudinal fiber stress	Pa
M	Bending moment	Nm
y	Vertical distance from the neutral axis to the point of interest	m
I	Moment of inertia	$kg \cdot m^2$
τ	Longitudinal shear stress	Pa
V	Shear force	N
A'	Cross-sectional area above or below the point of interest to the outer side of the beam	m^2
$\bar{y}$	Distance from the centroid of A' to the neutral axis	m
b	Width beam	m
y_{max}	Maximum deflection	m
W	Load (force)	N
l	Length beam	m
R_A	Vertical end reaction	N
x	Distance from the left end of the beam to any section	m
a	Distance from the left end of the beam to the location of applied force	m
w	Unit load	Nm
t	Thickness beam	m

8.2 Beam - Relating Deflection to Geometry

Using the starting formulas from table 7, the relation between vertical deflection and applied force can be calculated for both a concentrated load and uniform load. The applied force at a certain deflection is calculated for Zechstein evaporite caprock first. For calculating the force at a certain deflection for a certain beam configuration and rock type, width, thickness, length and elastic modulus of the beam must be considered.

Length and width of the beam are taken equal for both reservoir and caprock, while the elastic modulus and thickness differ in both cases. The resulting values are 1960 and 5060 m for width and length, representing the mean width and length of the 67 onshore gas fields examined in this study (excluding the Groningen field). The mean Rotliegend reservoir thickness is 120 m, while the average thickness of Basal Zechstein, i.e. the portion of the Zechstein Group containing anhydrite, is 50 m (NAM (2013)). The elastic modulus of sandstone differs from the elastic modulus of anhydrite. NAM (2013) describes the elastic or Young's modulus as a function of porosity, illustrating an elastic modulus of 15 GPa at a porosity of 0.15 (mean porosity of 68 onshore gas fields) for the Slochteren Formation. Following literature, a Young's modulus for anhydrite is suggested at 5 GPa, which is the Young's modulus upscaled for the presence of imperfections (Hangx et al. (2010)). This value is an order of magnitude lower than in NAM (2013), suggesting a Young's modulus of 30 (halite) - 70 (anhydrite) GPa for the Zechstein Group. This study considers both Young's moduli (i.e. 5 and 70 GPa).

The different input parameters result in separate values for force accompanying a certain deflection for caprock and reservoir. Since the assumption is made that a reservoir is only bended incrementally at the top, a very low thickness of 0.05 m for this top zone is selected. In first instance the focus will be on anhydrite caprock and depending on this behavior, incremental bending of Rotliegend reservoir is eventually assessed. The results are illustrated in table 9. Since the average subsidence from the field data is 5.5 cm, but presumably not fully representing the compaction in the reservoir, the most realistic deflection is assumed to be 0.1 m. It is noted that, as expected, the uniform load per meter is lower than the point load at an equal deflection.

The uniform load configuration, as uniform load is assumed to be representative for the situation in a reservoir (i.e. constant overburden pressure), is used to test the first hypothesis and is thus used to determine whether a ratio between length and width that is close to one gives a larger deflection at a constant force compared to a larger L/W ratio. Looking at the equation relating deflection to geometry, $y_{max} = \frac{-w_a l^4}{32Ebt^3}$, it can immediately be seen that a large length/width ratio, i.e. the beam is long and thin, provides a large deflection. This relation is not conform hypothesis, which is due to the fact that the beam is clamped at two sides only. The beam configuration is hence not an appropriate analogue for the bending mechanism of a reservoir or caprock. The behavior at the edges of a beam clamped at two sides is still examined in the following section, as this provides insight in the mechanics and directions of stress during bending before examining the more complex clamped elliptical plate configuration.

Table 9: *The relation between deflection and force for Zechstein evaporite caprock.*

Beam configuration	Equation	y_{max} (m)	W/w_a (N/Nm^{-1}) Anhydrite E = 5 GPa	W/w_a (N/Nm^{-1}) Anhydrite E = 70 GPa
Concentrated load	$W = -\frac{16 y_{max} b t^3 E}{l^3}$	0.05	$-7.550 \cdot 10^6$	$-1.060 \cdot 10^8$
		0.1	$-1.510 \cdot 10^7$	$-2.120 \cdot 10^8$
		0.2	$-3.020 \cdot 10^7$	$-4.240 \cdot 10^8$
		0.3	$-4.530 \cdot 10^7$	$-6.350 \cdot 10^8$
Uniform load	$w_a = -\frac{32 y_{max} b t^3 E}{l^4}$	0.05	$-2.990 \cdot 10^3$	$-4.190 \cdot 10^4$
		0.1	$-5.970 \cdot 10^3$	$-8.370 \cdot 10^4$
		0.2	$-1.190 \cdot 10^4$	$-1.670 \cdot 10^5$
		0.3	$-1.790 \cdot 10^4$	$-2.510 \cdot 10^5$

8.3 Behavior at a Clamped Beam Edge

After determining the force that is presumably applied when approaching realistic input values, the behavior at the edge of a beam for anhydrite caprock is examined. Focusing on the mechanisms only, the influence of bending for Rotliegend reservoir will be assessed when a clamped elliptical plate configuration is examined. Firstly, equations are determined for the longitudinal fiber stress (σ) and longitudinal shear stress (τ) at the end of the beam, as a function of depth in the beam. In the previous equations (sections 8.1 and 8.2) the x direction was assumed to be parallel to the length of the beam, the y-direction parallel to the depth or thickness of the beam and perpendicular to the length of the beam and the z-direction was assumed to be parallel to the width of the beam. The origin was assumed to be at the left end of the beam at the neutral axis or surface, which is normal to the load. For determining the longitudinal fiber and shear stresses as a function of x or depth within the beam, the axes are rotated, whereby now the x-, y- and z-axes are parallel to the thickness, length and width of the beam respectively. This gives the configuration illustrated in figure 64.

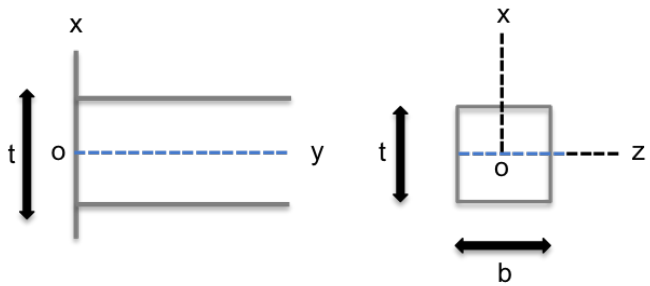

Figure 64: *The configuration of the x-, y- and z-axis, whereby x represents the depth in the beam. The dotted blue line depicts the neutral surface.*

Using equations 6 and 7 and the starting formulas of table 7, general formulas representing the behavior of σ and τ as a function of beam depth are determined for both concentrated and uniform load. These equations are demonstrated below (equations 8 to 11). The longitudinal fiber stress for concentrated load is defined as

$$\sigma = \frac{3Wlx}{2bt^3} \tag{8}$$

where W represents the point load applied on the beam, l the length of the beam, x the distance in depth or thickness of the beam, b the width of the beam and t the beam thickness. For uniform load the longitudinal fiber stress is defined as

$$\sigma = \frac{w_a l^2 x}{bt^3} \tag{9}$$

where w_a represents the unit load. The longitudinal shear stress for concentrated load is defined as

$$\tau = \frac{6W(\frac{1}{8}t^2 - \frac{1}{2}x^2)}{bt^3} \tag{10}$$

and for uniform load as

$$\tau = \frac{6w_a l(\frac{1}{8}t^2 - \frac{1}{2}x^2)}{bt^3} \tag{11}$$

The magnitude and direction of both σ and τ at the beam edge is examined, as this can influence fault reactivation. Understanding the orientations of stresses hence is crucial. In the center of a symmetrical beam the following applies; when a load is applied, the fibers on the concave side of the beam shorten, while the fibers on the convex side of the beam lengthen (Young and Budynas (2002)). This provides a tensile longitudinal fiber stress at the interval between the neutral surface and the lower, i.e. convex, side of the beam, and compressive longitudinal fiber stress at the interval between the upper, i.e. concave, side of the beam and the neutral surface (Young and Budynas (2002)). Considering the fixed ends of the beam the orientations of stresses are oppositely, with the fibers on the concave side lengthening and on the convex side shortening (Young and Budynas (2002)). Longitudinal fiber stress equals the horizontal stress in the beam. Longitudinal shear stress is caused by the difference in forces due to the bending moment where the horizontal shear stress is equal to the vertical shear stress, with shear stress acting both horizontally and vertically on each incremental stress element (Young and Budynas (2002)). The stress orientations at the left end of the beam are illustrated in figure 65. The orientations of stresses described above are thus expected when subsequently plotting the change in magnitude of σ and τ within the beam for anhydrite caprock.

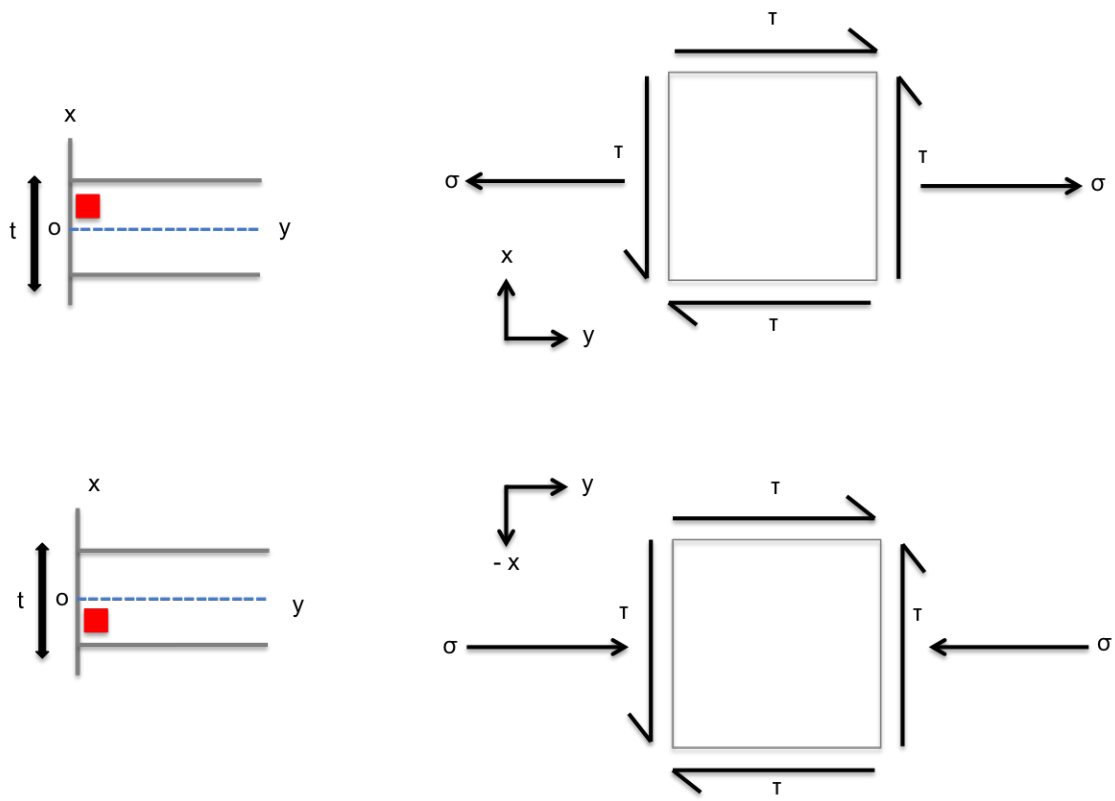

Figure 65: *The orientations of longitudinal fiber stress (σ) and longitudinal shear stress (τ) at the left end of the beam. The dotted blue line depicts the neutral surface and the red dot represents a stress element.*

To illustrate the change in magnitude of σ and τ with beam depth (x), equations 8 to 11 are filled in, only varying x. The values for length, width and thickness for anhydrite caprock discussed in the previous section are used. In addition, load (i.e. force) for anhydrite caprock at a deflection of 0.1 m and a Young's modulus of 5 GPa is used, resulting in 4 different equations (table 10).

Table 10: *Equations used in determining the change in magnitude of σ and τ in beam depth (x) for Zechstein evaporite caprock for a deflection of 0.1 m.*

Beam configuration	Longitudinal fiber stress	Longitudinal shear stress
Concentrated load	$\sigma = -469x$	$\tau = 0.19x^2 - 116$
Uniform load	$\sigma = -625x$	$\tau = 0.37x^2 - 232$

The change in stress magnitude within the beam at the beam's edge due to a force is subsequently visualized in figure

66. Since the stress magnitudes are obtained using the mean values for 67 onshore gas fields, the magnitudes may variate when other input parameters are used. However, other input parameters will not alter the shape of the change in stress magnitude within a beam. From figure 66 it can be observed that, when using a beam which is fixed at the edges, conform expectation the fibers on the concave side, between the neutral surface and the top part of the beam, are extended and on the convex side, between the neutral surface and the bottom part of the beam, are compressed.

The magnitude using an uniform load is observed to be larger than when a point load is applied. This observation is plausible since per meter length of the beam a force is applied applying uniform load instead of only at one point in the case of concentrated load. The longitudinal fiber stresses for concentrated and uniform load are compared to the longitudinal shear stresses for both load configurations, by computing σ and τ in figure 66. The longitudinal fiber stress can be observed to be linear, while the longitudinal shear stress is parabolic. Additionally, σ reaches a maximum value at the top and bottom of the beam and τ at the neutral surface, which is conform Young and Budynas (2002). The last important observation from figure 66 is that the magnitude of shear stress is approximately 2 orders in magnitude smaller than the magnitude of fiber stress. Since for anhydrite caprock the magnitude of τ is significantly smaller than the magnitude of σ, it is interpreted that shear stress has minimal influence and can thus be disregarded. Ergo, τ will not be considered further in this analysis.

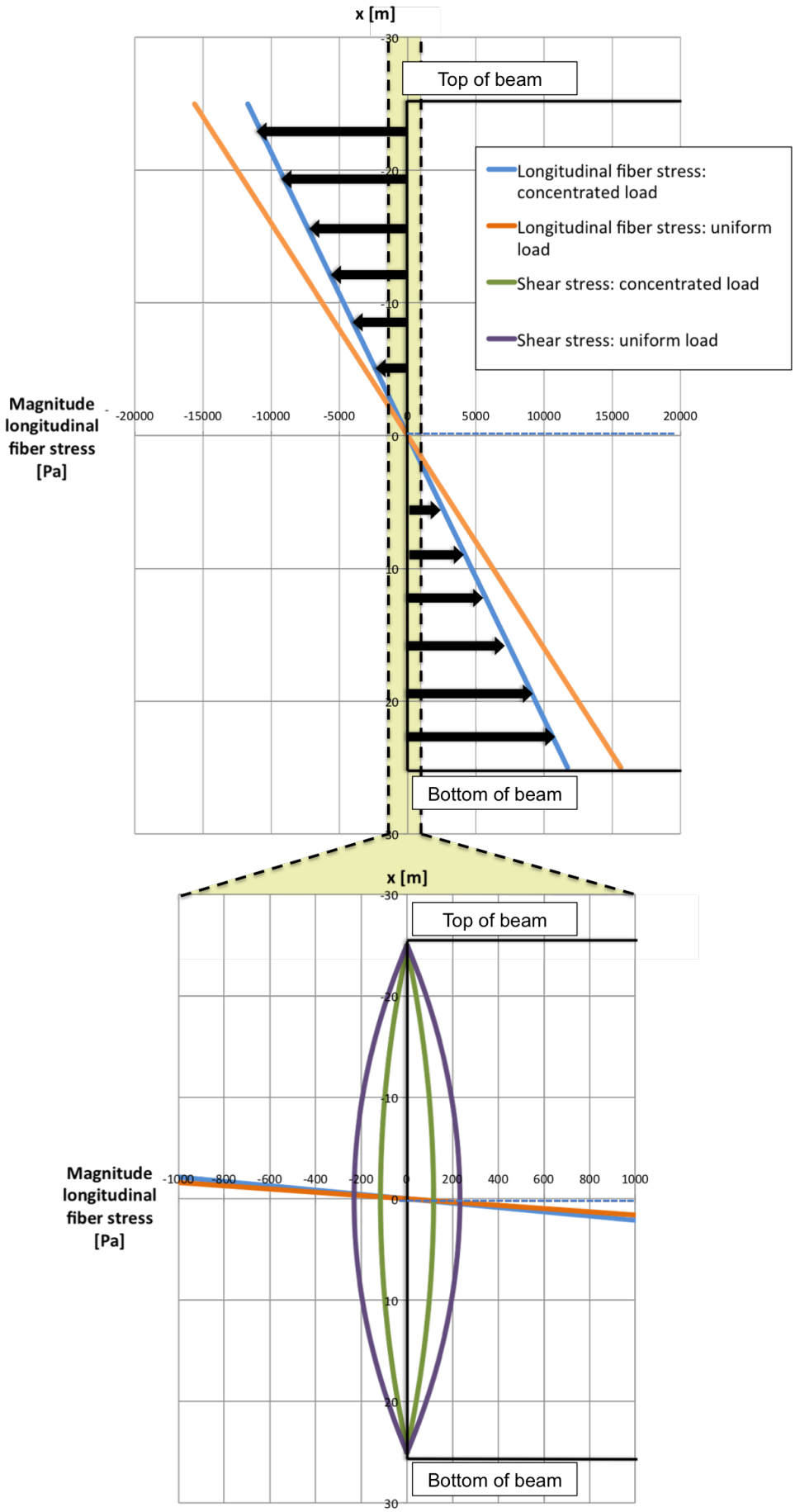

Figure 66: *The orientation and magnitude of longitudinal fiber stress (σ) and longitudinal shear stress (τ) at the left end of the beam for Zechstein evaporite caprock for a deflection of 0.1 m. The dotted blue line depicts the neutral surface.*

8.4 Ellipse - Model Configuration and Assumptions

Similar to the equations representing beam behavior, Young and Budynas (2002) describe bending of elastically stressed flat plates. This section focuses on a special configuration of a flat plate, namely an elliptical plate fixed or clamped at all sides that is subjected to an uniform pressure, as described in Nash and Cooley (1959), Young and Budynas (2002) and Wei-zang et al. (1992). The following assumptions apply to the equations in this section (Young and Budynas (2002)):
1) The flat plate consists of a horizontal plane and has an uniform thickness, which is smaller than $\frac{1}{4}$ of the transversal direction.
2) The elastic limit of the plate is not exceeded.
3) The maximum deflection does not exceed $\frac{1}{2}$ of the thickness.
4) The plate consists of material that is homogeneous and isotropic.
5) All forces are normal to the plate's horizontal surface.
6) The in-situ stress regime is normal.
7) Bending of the incremental top part of a reservoir occurs.
8) The fixed beam ends represent impermeable faults.

As a uniform load is subjected to the clamped ellipse, deflection occurs (Young and Budynas (2002); Wei-zang et al. (1992)). The surface in the middle between the upper and lower plane of the plate represents an unstressed neutral surface and the magnitude of stress away from the neutral surface in the plane of the clamped ellipse corresponds to the distance from the neutral surface (Young and Budynas (2002)). These stresses are biaxial; a condition where two perpendicular principal stresses act in the same plane and one perpendicular principal stress, in this situation the vertical stress, equals zero (McGraw-Hill Education (2003); Young and Budynas (2002)). The maximum stresses occur at the outer edges of the upper and lower plane of the ellipse (Young and Budynas (2002)). The change in stress due to an uniform load varies at different locations on the plane's edge. Young and Budynas (2002) define different equations for these varying locations, used as starting formulas (table 11). The symbols used in the equations of table 11 are shown in table 12. It is important to note that the equations in table 11 only consider bending stresses. Shear stress is hereby assumed to only have a minor magnitude and can hence be neglected (Young and Budynas (2002)). This is in line with the small values of stress magnitude as found in the earlier description of the behavior at the edge of a beam. To illustrate the behavior of an elliptical plate under uniform pressure, figure 67 demonstrates a compilation of the stress directions and magnitudes as a result of an uniform load (q) from an (oblique) side view (A), a top view of the upper plane of the plate (B) and a top view of the lower plane of the plate (C), both top views illustrating maximum stresses. Tensile stresses occur at the upper part of the ellipse around the edges, while compressive stresses are present in the center. The maximum tensile stresses thus occur at the edge of span b in the upper part of the clamped elliptical plate. In the lower plane of the elliptical plate the stress directions are vice versa, with the compressive stresses at the edges (maximum compressive stress at the edge of span b) and tensile stresses at the center. Focusing on the stress magnitudes at different locations along the edges of the ellipse, it is determined that $\sigma_{z(edge)} > \sigma_{z(center)} > \sigma_{x(center)} > \sigma_{x(edge)}$.

Table 11: *Starting formulas adopted from Young and Budynas (2002).*

Configuration	Location	Equation
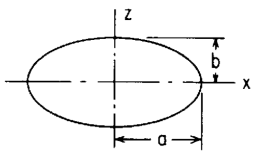	At the edge of span a	$\sigma_x = \frac{6qb^2\alpha^2}{t^2(3+2\alpha^2+3\alpha^4)}$
	At the edge of span b	$\sigma_{max} = \sigma_z = \frac{6qb^2}{t^2(3+2\alpha^2+3\alpha^4)}$
$\alpha = \frac{b}{a}$	At the center	$\sigma_z = \frac{-3qb^2(1+v\alpha^2)}{t^2(3+2\alpha^2+3\alpha^4)}$ $\sigma_x = \frac{-3qb^2(\alpha^2+v)}{t^2(3+2\alpha^2+3\alpha^4)}$ $y_{max} = \frac{-3qb^4(1-v^2)}{2Et^3(3+2\alpha^2+3\alpha^4)}$

Table 12: *Symbols used in starting formulas adopted from Young and Budynas (2002).*

Symbol	Description	Unit
E	Elasic or Young's modulus	Pa
v	Poisson's ratio	-
σ	Bending stress	Pa
b	Inner radius of the ellipse	m
a	Outer radius of the ellipse	m
y_{max}	Maximum vertical deflection	m
q	Uniform load (force) per unit area	Pa
α	$\frac{b}{a}$	$-$
t	Thickness ellipse	m

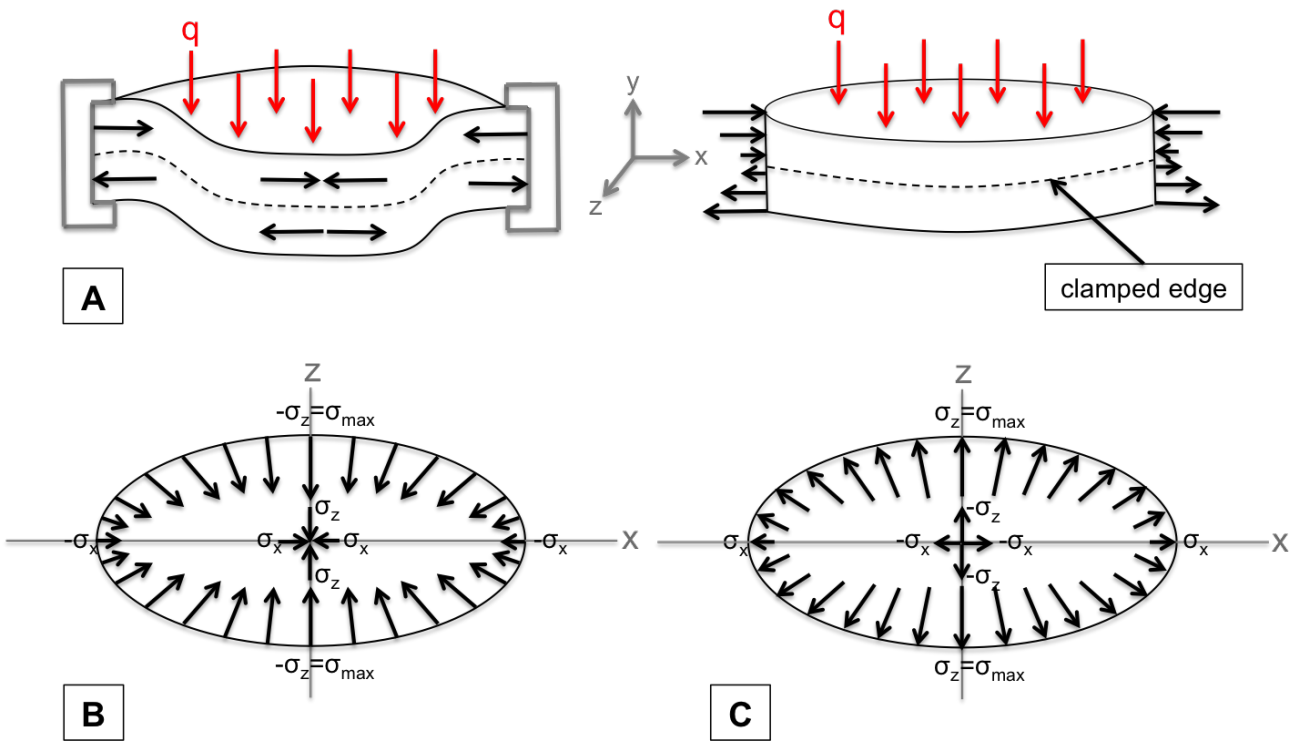

Figure 67: *A compilation of the stress directions and magnitudes in a clamped elliptical plate due to an uniform load (q). A) A cross-section (left) and an oblique side view of a clamped elliptical plate. The dotted line represents the unstressed neutral surface. B) A top view of the upper plane of the plate. C) A top view of the lower plane of the plate.*

8.5 Ellipse - Relating Deflection to Geometry

The first hypothesis of this section, namely *a L/W ratio close to 1 (i.e. a circular ellipse) gives a larger deflection at a constant force compared to a larger L/W ratio (i.e. a thin, long ellipse)*, can be examined by relating deflection to L/W ratio. Timoshenko and Woinowsky-Krieger (1959) state that the $\frac{b}{a}$ ratio and the magnitude of q affects the amount of deflection. A close relation between these parameters hence is expected. To determine a reasonable constant value of the uniform load, a 'standard situation' is implemented, where a = $\frac{1}{2}$L = 2530 m (the mean length of 67 onshore gas fields, excluding the Groningen field is 5060 m), b = $\frac{1}{2}$W = 978 m (the mean width of 67 onshore gas fields, excluding the Groningen field is 1956 m), the Poisson's ratio for anhydrite is 0.25 (NAM (2013)) and the thickness is 50 m (equal to the thickness of the basal Zechstein, NAM (2013)). Young's moduli of E = 5 GPa and E = 70 GPa are used (Hangx et al. (2010); NAM (2013)). Table 13 illustrates the resulting load per unit area for different deflections as calculated by a rewritten equation that relates uniform load to deflection (Young and Budynas (2002)):

$$q = -\frac{y_{max} 2Et^3(3 + 2\alpha^2 + 3\alpha^4)}{3b^4(1 - v^2)} \tag{12}$$

Table 13: *Standard situation for Zechstein anhydrite caprock, relating deflection to force.*

y_{max} [m]	q [Pa], E = 5 GPa Anhydrite	q [Pa], E = 70 GPa Anhydrite
0.05	-80	-1140
0.1	-160	-2290
0.2	-330	-4580
0.3	-490	-6870

Similar to the section focusing on the behavior of a beam, the values of q at a deflection of 0.1 m at elastic moduli of 5 and 70 GPa are selected as constant values. The ratio between a and b ($\frac{a}{b}$), i.e. L and W (L/W), is varied between a value of 1 to 10, by a stepwise increase of the length, i.e. outer radius of the ellipse, and decrease of the width, i.e. inner radius of the ellipse, whereby the area is kept constant. Three different values for area (small, medium and large) are implemented to ultimately compare the trends to the field data.

As in earlier sections an area $>1.2 \cdot 10^7$ m^2 is interpreted to be a large area, which is based on the mean area of 67 onshore gas fields, excluding the Groningen field. An area between $0.625 \cdot 10^7$ to $1.2 \cdot 10^7$ m^2 is interpreted to be a medium sized area, and a low area is defined as an area $<0.625 \cdot 10^7$ m^2.

The surface subsidence above a field is assumed to be similar to the amount of deflection in the model, and the outcome of plotting the surface subsidence and deflection versus the ratio between length and width is illustrated in figure 68. Figure 68 A illustrates all surface subsidence field data, while figure 68 B illustrates the field data divided in terms of field size, whereby the areas used in the model are approaching the mean of the division of area ranges used in the field data. A small, medium and large area in the model equals an area of $0.4 \cdot 10^7$, $0.9 \cdot 10^7$ and $1.4 \cdot 10^7$ m^2, upon a length increase of 2260-7120, 3380-10680 and 4220-13320 m respectively. A summary of the input data in figure 68 is illustrated in table 14.

Table 14: *Summary of the input data in figure 68.*

Area	Field Data $[m^2]$	Model $[m^2]$	Length Increase $[m]$
Small	$<0.625 \cdot 10^7$	$0.4 \cdot 10^7$	2260-7120
Medium	$0.625 \cdot 10^7$ - $1.2 \cdot 10^7$	$0.9 \cdot 10^7$	3380-10680
Large	$>1.2 \cdot 10^7$	$1.4 \cdot 10^7$	4220-13320
Area Equation	$A = L \cdot W$	$A = \pi ab$ $a = \sqrt{\frac{A}{\pi} \cdot \frac{a}{b}}$	

Firstly focusing on 68 A, the general observation can be made that in all cases of the model the amount of deflection decreases as a larger L/W ratio is reached. This observation is interpreted to be conform hypothesis. From a L/W ratio of approximately 5-6 the ratio can be interpreted to have only a small influence on the amount of deflection or surface subsidence. This coincides with the field data correlation section, where the observation was made that at L/W ratios larger than approximately 5 low vertical strain occurs (<0.0005). Additionally it can be interpreted that the area has a large influence on deflection as well, as an equal increase in area results in a non-linear increase in surface subsidence.

Continuing with the field data, the same trend appears to be present as in the model, where the surface subsidence increases with approaching a L/W value closer to 1. However, a large amount of data with a low L/W ratio and relatively low surface subsidence is present, resulting in limited data availability with larger surface subsidence (>0.05 m).

Significant differences in the composition of field data compared to the model are present. Area and load are in the model both taken as a constant and the L/W ratio varies, while in the field data the overburden pressure varies slightly per field and the area as well as the L/W ratio varies significantly. Figure 68 B accordingly illustrates the field data divided per area range (i.e. small, medium and large area). Using this configuration it is inferred that a reasonable comparison between the model and the field data of 63 onshore gas fields (excluding the Tietjerksterdadeel RO, Tietjerksteradeel KNNS, Vierhuizen-Oost, Ameland-Noord and Lauwersoog-C fields) is provided. It can be observed that the field data of small area fields appear to follow the trend of the model for a small area. An obvious outlier, with a relatively large magnitude of surface subsidence and a small area, is positioned at a L/W ratio of 5.84. This field is the Rodewolt field, located in close proximity of the Groningen field. It is hence interpreted that the large amount of surface subsidence in the Groningen field sources the relatively large surface subsidence in the Rodewolt field. Since medium and large area fields both occur at a L/W ratio close to one with a small surface subsidence, this observation is more difficult to explain. The occurrence of medium and large fields at a L/W ratio close to one may be interpreted to be related to other factors influencing the field data, such as a low amount of depletion and a high field compartmentalization. In addition, inaccuracy of the surface subsidence data may provide uncertainty.

The observation is made that fields surrounding the model for a medium or large area, are mostly medium or large fields, thereby following the trend set out by the model. It is hence interpreted that the model and the field data roughly coincide, but other aspects are influencing the field data as well. Considering large area field data and the trend set out by the model for a large area, it can be observed that the deflection in the model is larger than the surface subsidence in the field data. This may be explained since the model is not accounting for resistance of the underburden, while this is affecting the field data.

From the observations above the main result is that the model of a clamped ellipse confirms the hypothesis that at a thin, long ellipse gives a larger maximum deflection (i.e. surface subsidence) compared to a more circular ellipse. In addition, the amount of deflection increases with increasing area as well.

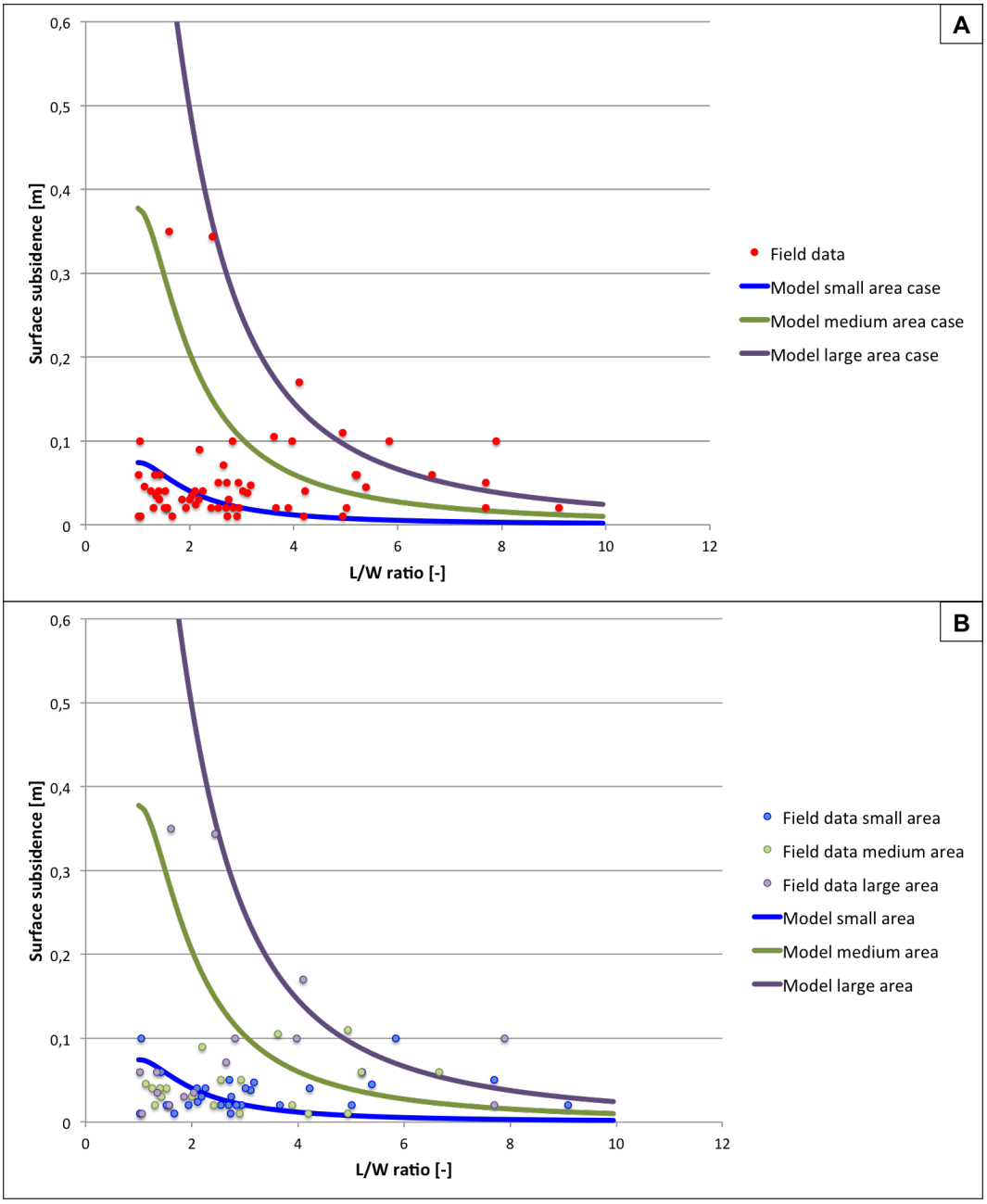

Figure 68: *Surface subsidence versus L/W ratio including the results of the modeled and the field data of 63 onshore gas fields. A) illustrates field data without division per area range, B) illustrates the field data divided into small, medium and large area ranges.*

8.6 Behavior at the Edges of the Ellipse

From the first hypothesis a second hypothesis can be formulated, namely *a L/W ratio close to 1, resulting in a larger deflection at a fixed load and area, causes a larger horizontal stress change as well.* This section attempts to test the

second hypothesis, focusing on the position on the edge of the ellipse where a maximum decrease in horizontal stress occurs. Situated at the edge of span b in the top plane of the ellipse, the change in horizontal stress may or may not result in the occurrence of failure.

Three equations, mentioned in previous sections, apply to this hypothesis. These equations are: $y_{max} = -\frac{3qb^4(1-v^2)}{2Et^3(3+2\alpha^2+3\alpha^4)}$, $q = -\frac{y_{max}2Et^3(3+2\alpha^2+3\alpha^4)}{3b^4(1-v^2)}$ and $\sigma_{max} = \sigma_z = \frac{6qb^2}{t^2(3+2\alpha^2+3\alpha^4)}$, defining the maximum deflection, the uniform load per unit area and the maximum bending stress at the edge of span b, respectively. Since one parameter needs to be fixed in order to define the influence of the other parameter, two analyses are performed: 1) The deflection, y_{max} is fixed. The value of q is able to vary for different L/W ratios and implemented in the equation for maximum bending stress and 2) The uniform load, q, is fixed. Both y_{max} and maximum bending stress are assessed separately for different L/W ratios.

Starting at the first analysis, a fixed value of 0.1 m for deflection is used, the Poisson's ratio for anhydrite is 0.25, the Young's modulus is selected at 70 GPa and the thickness is 50 m (NAM (2013)). Since this section focuses on the bending behavior at the edges of the ellipse, which is equal regardless of the magnitude of Young's modulus, the results for a Young's modulus of 5 GPa are not illustrated in this section. A Young's modulus of 5 GPa is considered again in the next section, defining the implications for total horizontal and shear stress.

The L/W ratio is varied from a value of 1 to 10 and the mean area for the model ($0.9 \cdot 10^7\ m^2$) is used. The results are illustrated in figure 69. Uniform load (q) increases exponentially at an increase in L/W ratio. This can be translated to a larger uniform load or force needed for the same amount of deflection to be reached at a large L/W ratio. On the other hand this implies that less force is needed for a L/W ratio that is close to one to reach a certain amount of deflection. The resulting values of q can be implemented as the maximum bending stress is calculated for equal L/W ratios. It can be observed that the maximum bending stress in figure 69 increases linearly with increasing L/W ratio. It is hence interpreted that a larger maximum bending stress is needed for an equal deflection (0.1 m) at a higher L/W ratio. As q is substituted in the equation for σ_z stated before, the following equation remains: $\sigma_{max} = \sigma_z = \frac{-y_{max}4Et}{b^2(1-v^2)}$. It can thus be observed that b is the only parameter that is varied, and as L/W increases b decreases and hence the maximum bending stress increases.

Continuing with the second analysis, a Poisson's ratio for anhydrite of 0.25, a Young's modulus of 70 GPa, an area of $0.9 \cdot 10^7\ m^2$ and a thickness of 50 m is used. The uniform load, q, is fixed, while the maximum deflection can vary. The value of q at a deflection of 0.1 m at an elastic modulus of 70 GPa is selected as a constant value (table 13, q = -2290 Pa). These results are discussed in the section 'Ellipse - Relating Deflection to Geometry'. Additionally the maximum bending stress is plotted for the corresponding L/W ratio ranges, in which q is fixed. The maximum bending stress and maximum deflection for an increasing L/W ratio of 1 to 10 are illustrated in figure 70.

Bending stress is not influenced by deflection in this figure, since the uniform load (q) is fixed. A small increase in maximum bending stress is observed at an L/W ratio between 1 and approximately 1.5. From a L/W ratio of 1.5, a decrease in maximum bending stress with increasing L/W ratio can be observed. Considering the equation for bending stress ($\sigma_{max} = \sigma_z = \frac{6qb^2}{t^2(3+2\alpha^2+3\alpha^4)}$) it is observed that over the whole L/W ratio range q and t remain constant and b and $\frac{b}{a}$ decrease. The maximum bending stress increase in the L/W ratio range from 1 to 1.5 can only be achieved when the relative decrease in the numerator is less than the decrease in the denominator of the equation for bending stress.

In order to asses the effect of area on the maximum bending stress in the model versus L/W ratio the results for a small, medium and large area ($0.4 \cdot 10^7$, $0.9 \cdot 10^7$ and $1.4 \cdot 10^7\ m^2$) are illustrated in figure 71. From this figure it is observed that the trend in maximum bending stress is equal for all areas, namely with a peak at a L/W ratio of approximately 1.5.

In an attempt to determine whether the field data illustrate a peak as well, the data for a L/W ratio between 1 and 2.3 is plotted versus the total seismic moment. It is hereby assumed that bending stress is related to total seismic moment, since a change in bending stress may lead to fault reactivation, as discussed in the following section. It is important to notice that, since two vertical axes are used in the figure, the focus is on the observed trends rather than the magnitudes. The observation is made that the trend is roughly followed, with an apparent peak at approximately 1.5. It is interpreted that bending stress and total seismic moment are closely related to L/W ratio due to the similarity of the observed trends. It must however be taken into account that the data is relatively sparse and other important influencing factors, such as amount of depletion and porosity, are interpreted in the 'field data correlation' section to have a large influence as well. From the observed trends it can be interpreted that the maximum change in stress occurs around a L/W ratio of 1.5. From a L/W ratio of 1.5 the results are conform hypothesis, illustrating that a decrease in maximum bending stress occurs while L/W ratio increases at an equal load. Yet, the reason why a peak occurs in the model is not understood.

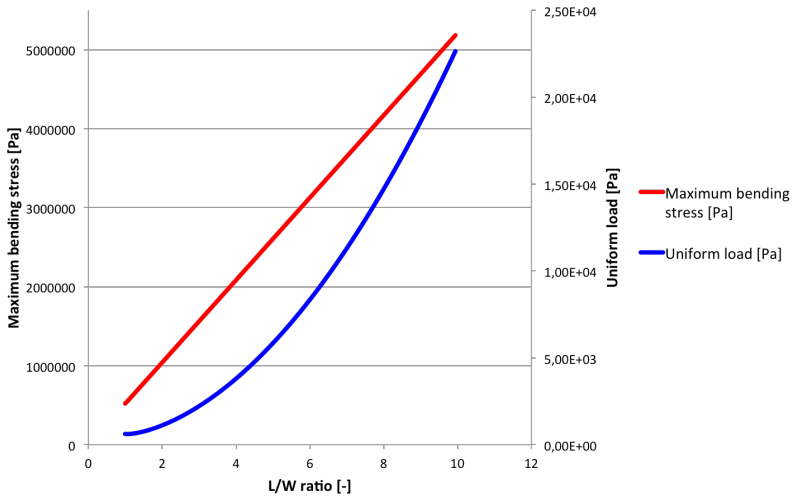

Figure 69: *The maximum bending stress and uniform load versus the L/W ratio. The maximum deflection is constant.*

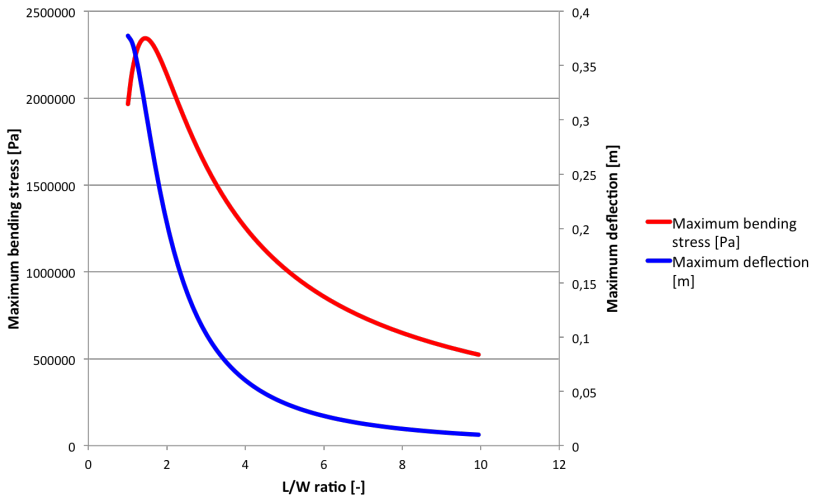

Figure 70: *The maximum bending stress and maximum deflection versus the L/W ratio. The uniform load is constant.*

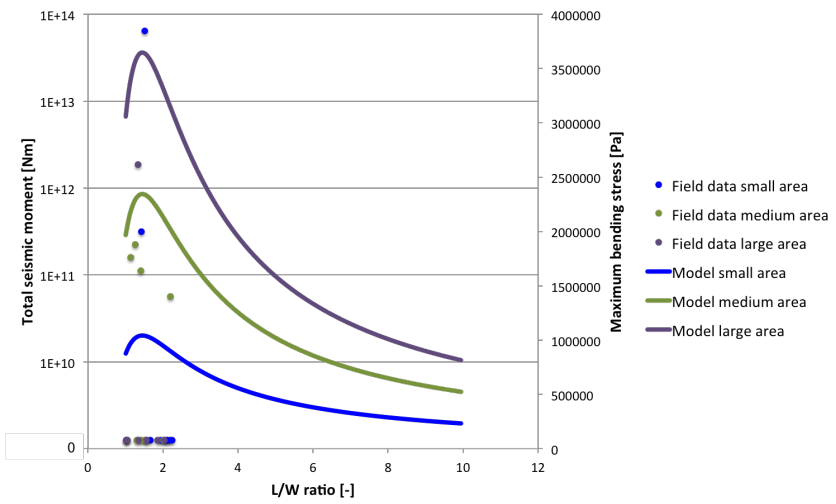

Figure 71: *The maximum bending stress and maximum deflection versus the L/W ratio for a small, medium and large area of* $0.4 \cdot 10^7$, $0.9 \cdot 10^7$ *and* $1.4 \cdot 10^7$ m^2. *The uniform load is constant. The total seismic moment versus L/W ratio is illustrated for field data occurring in a L/W ratio range of 1-2.3.*

8.7 Implications for Total Horizontal and Shear Stress

This section describes the effect of the stress change on the frictional behavior of sandstone reservoirs and anhydrite caprock for a clamped elliptical plate configuration. Since the previous sections only describe the *changes* in stress, this section describes the implications for the total horizontal and shear stress at a fault-bounded side of a reservoir or caprock.

The initial in-situ stress is determined first. σ_1 is determined by subtracting the hydrostatic pressure from the lithostatic stress, from which σ_2 and σ_3 are assumed on the basis of literature. At a general hydrostatic pressure gradient of 1 bar per 10 m and a mean depth of 3000 m for 68 onshore gas fields, the hydrostatic pressure is 30 MPa. The lithostatic stress is defined by using $\rho_{rock} \cdot 9.81 \cdot h$, where ρ_{rock} is the overburden density and h the depth at which the rock is positioned. Since the Zechstein Group overlies the Rotliegend reservoirs, the overburden density for reservoir and caprock will slightly differ. However, since all data of the 68 onshore gas fields is averaged in the model, the difference is assumed to be trivial. The mean overburden density of 68 fields is taken of 2264 kg/m^3 for both reservoir and anhydrite caprock. The lithostatic stress becomes 67 MPa, which gives a $\sigma_{veff} = \sigma_1 = 37$ MPa. The vertical overburden stress of 67 MPa at a depth of 3000 m is similar to the vertical overburden stress in Hol et al. (2015), giving a stress of 80 MPa at a depth of 3700 m. The value corresponds to the initial stress state of 2.14 bar/10 m in NAM (2013) as well, where this would imply a σ_v of 64.2 MPa at a depth of 3000 m.

After the determination of σ_1, this value is related to σ_2 and σ_3. An extensional in-situ stress regime gives $\sigma_2 = \sigma_3$, which is determined by different authors as $0.6 \cdot \sigma_1$, $0.67 \cdot \sigma_1$ and $0.7 \cdot \sigma_1$ (Hangx et al. (2010); Rutqvist et al. (2008); Zoback (2010)). In this study $0.67 \cdot \sigma_1$ is chosen as a value for σ_2 and σ_3, thereby having a value of 24.8 MPa. Subsequently the linearized Mohr-Coulomb failure lines for anhydrite caprock and sandstone reservoir are determined, which is written as (Byerlee (1978))

$$\tau = S_0 + \mu\sigma_n \tag{13}$$

where τ represents the shear stress on the failure plane, S_0 and μ are material properties, namely the is the cohesive shear strength and coefficient of internal friction and σ_n represents the normal stress on the failure plane. Combining the weakest Mohr-Coulomb failure criteria (i.e. worst-case scenario) of Pluymakers et al. (2014) for fractured, unhealed anhydrite gouge, both failure criteria involved are defined as

$$\tau = 0.53\sigma_n \tag{14}$$

and

$$\tau = 4.4 + 0.35\sigma_n \tag{15}$$

Combining the Drucker-Prager material model used in NAM (2013), with the comparison between the Mohr-Coulomb criterion and the Drucker-Prager model in Zoback (2010) and the Coulomb friction coefficient of 0.48 for reservoirs in the northern Netherland (NAM (2013)), the Mohr-Coulomb failure criterion for sandstone reservoir can be described as

$$\tau = 7.8 + 0.48\sigma_n \tag{16}$$

where the worst-case scenario (i.e. no cohesion) becomes $\tau = 0.48\sigma_n$. Standard equations for 2D stress on a pre-existing fault plane are (Zoback (2010))

$$\sigma_n = \frac{1}{2}(\sigma_1 + \sigma_3) + \frac{1}{2}(\sigma_1 - \sigma_3)cos2\theta \tag{17}$$

$$\tau = \frac{1}{2}(\sigma_1 - \sigma_3)sin2\theta \tag{18}$$

where θ represents the angle between the fault normal and σ_1. When a vertical fault configuration is used as described in this chapter, this implies θ has a value of 90°, thereby causing the shear stress on the failure plane to become zero an thus the Mohr circles for both sandstone reservoir and anhydrite caprock can not be computed. To overcome this problem an average normal fault is used for calculating τ and σ_n, having a dip of approximately 60° (Zoback (2010)). The angle between the fault normal and σ_1, θ, thus becomes 60°. The inevitable assumption is thereby made that the behavior of clamped ellipse bending is similar in the cases where the bounding fault at the edges is 1) vertical, i.e. 90° or 2) equal to an average normal fault, i.e. 60°.

Figure 72 illustrates the failure criteria for reservoir sandstone and caprock anhydrite. The Mohr circle for the initial in-situ stress state is computed as well. By substituting equations 17 and 18 in the worst-case failure criterion equations for anhydrite and sandstone and using the $\sigma_1 = 37$ MPa and $\theta = 60°$, the value of σ_3, i.e. horizontal stress needed for failure at a constant σ_1 can be calculated. Values of $\sigma_3 = 14.6$ MPa and $\sigma_3 = 13.4$ MPa can be found for reservoir sandstone and caprock anhydrite respectively, representing the σ_3 needed for failure. Considering the initial value for σ_3 of 24.8 MPa, the horizontal stress needs to be lowered 10.2 MPa for reservoir sandstone and 11.4 MPa for caprock anhydrite for the occurrence of failure. To define whether failure occurs, the approximate values of maximum horizontal stress change (at a L/W ratio of 1.5) for anhydrite caprock and sandstone reservoir are listed in table 15.

The values for Rotliegend sandstone reservoir are provided with a similar method compared to the values of anhydrite caprock. Since bending is assumed to be occurring incrementally only in Rotliegend reservoir, the thickness that is affected is assumed to be 0.05 m. Using an incremental thickness for the Rotliegend reservoir, the maximum bending stress is 4 orders in magnitude smaller compared to anhydrite caprock (E = 70 GPa). The difference can be attributed to the difference in thickness used for anhydrite caprock and Roliegend reservoir (50 versus 0.05 m) and to the difference in Young's modulus and Poisson's ratio. Using a Young's modulus of 70 GPa for anhydrite caprock, q (load or force) in the standard situation increases, since at a larger stiffness more load or force is needed for a certain deflection. The increased force increases the maximum bending stress, or maximum horizontal stress, as well.

Comparing the change in horizontal stress for anhydrite caprock to Hangx et al. (2010) (E = 5 GPa), the values of change in horizontal stress differ approximately 1 order of magnitude. This can be caused due to the different configuration used; a clamped circular plate in Hangx et al. (2010) and a clamped elliptical plate in this study. Additionally, area is taken constant during the analyses in this study. Focusing on the values of maximum magnitude of horizontal stress change in table 15, it is important to realize that these values are obtained while several significant assumptions were used. A realistic quantification of the resulting maximum horizontal stress is therefore difficult to obtain. Yet, using several assumptions, caprock bending or bending of the incremental top part of a field, presented as a clamped elliptical plate, will not contribute to the change in horizontal stress sufficiently for failure to occur. Additionally, due to the larger thickness and changes in horizontal stress of anhydrite caprock, horizontal bending stress change at the edges is more likely to enhance caprock failure than failure in the reservoir itself. The suggestion is made that other processes involved in depletion, such as an overall shrinkage or compaction of a reservoir, may provide larger stress changes and thus cause a lowering of the normal stress, resulting in failure.

Table 15: *The maximum horizontal stress changes in the model for areas defined as small, medium and large (*$0.4 \cdot 10^7$*,* $0.9 \cdot 10^7$ *and* $1.4 \cdot 10^7$ m^2*) for anhydrite caprock and sandstone reservoir.*

Area [m^2]	Maximum horizontal stress change [Pa] Anhydrite caprock, E = 5 GPa	Maximum horizontal stress change [Pa] Anhydrite caprock, E = 70 GPa	Maximum horizontal stress change [Pa] Sandstone reservoir, E = 15 GPa
Small ($0.4 \cdot 10^7$)	-74000	-1040000	-220
Medium ($0.9 \cdot 10^7$)	-167000	-2340000	-490
Large ($1.4 \cdot 10^7$)	-260000	-3640000	-760

8.8 Introducing Reservoir Compaction

Since compaction of a producing reservoir may provide larger stress changes than bending alone, it is important to assess this mechanism as well. Several models for the horizontal stress change within a reservoir can be found in literature. Engelder and Fischer (1994), Lorenz et al. (1991) and Zoback (2010) describe an equation that predicts the horizontal change in stress during depletion, assuming that the considered reservoir behaves elastically and has an infinite size (which according to Segall and Fitzgerald (1998) produces representative results if the size of the reservoir is larger than ten times the thickness), immediate loading by the overburden causing the change in stress, a high porosity and no occurrence of lateral strain (Zoback (2010)). This equation is

$$\Delta\sigma_h = \alpha \frac{1-2v}{1-v} \Delta P_f \tag{19}$$

where $\Delta\sigma_h$ is the change in horizontal stress, α represents Biot's coefficient, v is the Poisson's ratio and ΔP_f is the change in pore fluid pressure as a consequence of depletion (Engelder and Fischer (1994); Lorenz et al. (1991); Zoback (2010)). Implementing the values for a Rotliegend reservoir, namely a Poisson's ratio of 0.20 (NAM (2013) and assuming a Biot's coefficient of 1 (Zoback (2010)), the following equation remains:

$$\Delta\sigma_h = \frac{3}{4} \Delta P_f \tag{20}$$

As the mean ΔP_f in the dataset of 68 onshore gas fields is 20 MPa, the mean change in horizontal stress could be -15 MPa. The corresponding change in stress state is illustrated in figure 72. The observation can be made that the failure criterion is approached closer taking compaction into account, compared to only considering the bending mechanism.

While depletion shifts the Mohr circle and illustrates a larger amount of horizontal stress decrease compared to bending of a caprock and incremental part of a reservoir, bending does change horizontal stress and the corresponding Mohr circle. This effects shear potential and brings the state of stress closer to the failure envelope. If horizontal stress is significantly lowered due to compaction, hence positioning the Mohr circle close to the failure envelope, bending stresses may play an important role and can possibly be a determining factor for the occurrence of failure.

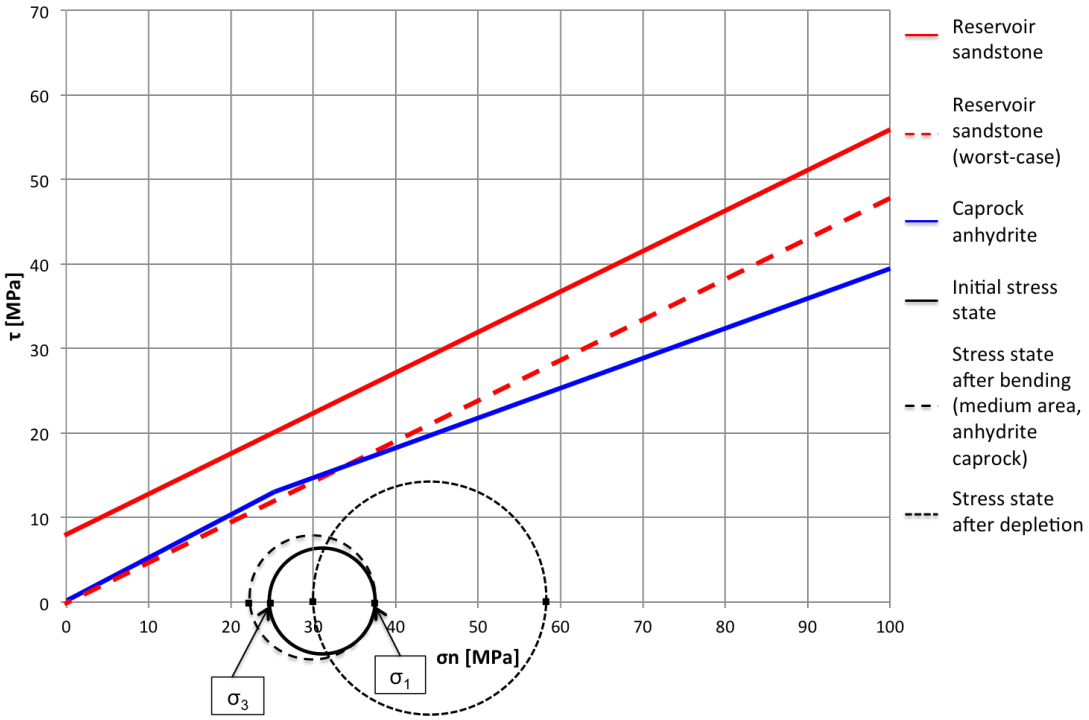

Figure 72: *The Mohr diagram, illustrating the failure criteria for both reservoir sandstone and caprock anhydrite and the Mohr circle for initial in-situ stress, the stress state after bending and the stress state after compaction.*

9 General Discussion and Conclusions

Providing a first level assessment of the complex mechanisms involved in reservoir compaction, surface subsidence and induced seismicity, this study attempts to clarify two main problems: *1) Can subsidence and ultimately seismic potential of Dutch onshore gas fields be correlated with and understood from field data?, and 2) Is there any predictive potential from such an approach?*

Reservoir compaction and induced seismicity are both complex problems influenced by field parameters that impact each other as well. This study thoroughly discusses the correlation of 18 field parameters with reservoir compaction, i.e. vertical strain, and seismicity occurrence, i.e. total seismic moment. As a consequence of the complexity of the problem one univocal answer is not obtained and no single reservoir parameter can be assigned to solely contribute to reservoir compaction and hence ultimately seismic potential. Yet, several field parameters are interpreted to correlate well (section 5.12, 'Field Data Correlation Summary') and confirm hypotheses (section 4.4, 'Hypotheses Summary') that are based on literature.

Some general discussion points are proposed. Literature illustrates that the generation of induced seismicity strongly depends on fault orientation and characteristics. Fault orientation and characteristics are not incorporated in the correlation of field parameters, which implies uncertainty on the interpretations regarding these parameters. Depending on fault characteristics and orientation, one fault bounding a reservoir may require a different horizontal stress change to reach the failure criterion and induce seismicity, compared to another fault. This may result in fields that generate induced seismicity at conditions that are, according to other field parameters, not favorable for induced seismicity to occur and vice versa. In addition, all induced seismic events assessed in this study occur within 500 m of a fault zone. Fields that have not generated induced seismicity yet, may become seismic in the future.

Another uncertainty arises regarding the collection of field data. Several field data, such as porosity (inferred from well data), are obtained from sparse data points. Heterogeneity in the reservoir combined with sparse density of samples taken from the field imposes uncertainty in these parameters. Most field characteristics are additionally averaged, thereby decreasing the variability in one parameter. The largest uncertainty is present considering the locations of the seismic events and the accuracy of surface subsidence and hence strain data.

Considering the translation between field data in this study and recent laboratory data (UPPD experiments), a contrast is evident, where experimental data results in values of one order of magnitude larger for vertical strain increase during depletion compared to field data. The difference in magnitude can possibly be assigned to the occurrence of Zechstein caprock and faults in the subsurface along which frictional sliding may occur. In addition, the discrepancy may be explained looking from the perspective of laboratory experiments, where localized deformation possibly increases the stress path. In order to make an accurate prediction of reservoir compaction by upscaling laboratory data, it is important to keep the discrepancy beween laboratory and field data in mind.

Illustrating field data stress-strain curves alone; in order to examine the simple mechanical response of different gas fields it is determined in this study whether permanent, inelastic deformation occurs in the northern Netherlands. When reservoir depletion causes the vertical effective stress to increase sufficiently, a yield point may be reached, representing the inelastic part of the stress-strain curve. Structural element in which the field is located is suggested to effect non-linearity, where the Groningen Platform data appears to become non-linear in an earlier stage of depletion compared to the Ameland Platform/Lauwerszee Trough data. When no subdivision is applied, non-linearity may roughly be observed from a yield point of $\Delta P_f =$ 25 MPa.

Since actual quantification of the results is difficult and it cannot be assumed that correlation is directly related to causation, the field data is coupled back to an analytical model (Aldrich (1995)). The model examines the geometry hypotheses considering length-to-width ratio from the field data correlation by assessing the bending mechanisms of a caprock and incremental top part of the reservoir. The generic model, representing a clamped elliptical plate, illustrates that similar to the surface subsidence field data, amount of deflection decreases as a larger length-to-width ratio is reached and that area influences the amount of deflection significantly. In both field data and model it is concluded that from a length-to-width ratio of 5-6 the ratio only has a small influence on the amount of vertical strain or deflection. In addition, from a length-to-width ratio of 1.5 a decrease in maximum horizontal bending stress occurs while length-to-width ratio increases. As maximum horizontal stress and seismic potential are coupled, field seismicity data illustrates a similar trend.

While depletion shifts the Mohr circle away from the failure criterion, but illustrates a larger amount of horizontal stress decrease compared to bending of a caprock and incremental part of a reservoir, bending changes horizontal stress and the corresponding Mohr circle as well. This effects shear potential and brings the state of stress closer to the failure envelope. If horizontal stress is significantly lowered due to compaction, hence positioning the Mohr circle close to the failure envelope, bending stresses may play an important role and can possibly be a determining factor for the occurrence of failure.

Considering the translation between laboratory experiments and field data and the simple model for the bending behavior of a caprock and reservoir, the results of these sections are coupled back to the field data, which in turn can be coupled back to geology. Integrating all aspects of this study field parameters can be subdivided into two groups; parameters that possibly can be eliminated in further research and parameters that correlate well with reservoir compaction and/or

induced seismicity, which therefore cannot be eliminated in further research. Simultaneously, integrating field parameters that correlate well with seismicity occurrence, a general outline of a field that would be prone to seismicity can be provided. Introducing a general outline of a field prone to seismicity can be useful for recently discovered fields that are considered for future production in the Netherlands and beyond.

Field parameters that cannot be eliminated in further research are field porosity, length-to-width ratio, temperature, production time and reservoir depletion. The degree of reservoir depletion itself appears to have a moderate correlation with reservoir compaction and no correlation with induced seismicity. However, during the discussion of several field parameters the degree of depletion came across as a determining factor. Hence, this study suggests a large dependence of the reservoir compaction and induced seismicity of reservoir parameters on degree of depletion in a field. As the surface subsidence in the field was successfully tested with length-to-width ratio in the model, it is concluded that this parameter is especially important. In addition, higher compressibility is assigned to high porosity samples compared to low porosity samples in the laboratory experiments, hence this increases confidence in the importance of the porosity parameter as well.

Taking into account a certain level of uncertainty, a reservoir prone to seismicity occurrence would then have a high porosity, a large degree of depletion and production time (where the mean time to an induced seismic event from the start of production is 16 years), a low reservoir temperature, a depth of 2900-3000 m and a length-to-width ratio close to one. This study suggests that porosity and depletion are related to reservoir depth. At a depth of approximately 2900-3000 m peak seismicity and high strains occur, at which reservoir depth is 1) shallow enough to cause the reservoir to remain a relatively large porosity and small initial compaction and 2) deep enough to have a large depletion due to high production rates.

Defining reservoir parameters that possibly can be eliminated for further research is difficult, as the reservoir parameters in first instance were selected because literature suggested an influence on reservoir compaction and seismic potential. All parameters are interpreted to impact reservoir compaction and seismic potential to some degree, however no correlation could be found with length-to-thickness, length-to-depth, width-to-thickness, area-to-thickness ratio and volume.

This study concludes that no field parameter examined in this study illustrates a distinguishing capacity for seismicity occurrence. In other words, no visual distinction is observed where a parameter above or below a certain value illustrates a substantial amount of seismic or aseismic fields only. This implies that other parameters apart from solely one parameter are involved as well, and strengthens the conclusion that no single reservoir parameter can be assigned to solely contribute to reservoir compaction and hence ultimately seismic potential.

Even though this study increases understanding about the complex mechanisms involved in reservoir compaction, surface subsidence and induced seismicity, the large amount of field parameters and associated uncertainties examined in this study encourage further research. Improved data, such as surface subsidence data and locations of seismic events, could additionally reduce uncertainties and thereby provide further understanding of the complex mechanisms associated with reservoir compaction and seismicity. In addition, after this first-level assessment considering qualitative correlation, using a quantitative approach involving statistics will improve further research.

10 Recommendations for Further Research

Since this study assesses field data that contribute, in some correlations, to ambiguous results, further research is necessary. This section describes the suggestions for continuing and improving this study, focusing on suggestions for the field data correlation, laboratory experiments and the analytical model.

10.1 Suggestions for Field Data Correlation

An important parameter that is not incorporated in this study is the thickness of the Ten Boer claystone, located above most reservoirs examined in this study. It could be interesting to determine the relation between induced seismicity and the Ten Boer claystone thickness, since this rock type possibly influences the results due to characteristics associated with clay (e.g. the ability to expand or swell) (Anderson et al. (2010)). Time limitations resulted in the decision to not incorporate this parameter in this study.

The field data that can be revised and thereby directly improve the results are the surface subsidence data and the data regarding the occurrence of seismic events. Since all reservoir parameters are plotted against vertical strain, new InSAR data will provide more accurate vertical strains and field data correlation could thus be improved. Additionally the location of seismic events is severely inaccurate vertically with a margin of error of 1-2 km. The lateral uncertainty is better, namely 500 m. Examining the exact locations at which the induced seismic events have occurred would significantly improve the correlation of field data. In this study it is assumed that induced seismic events that are positioned laterally in a field, also have occurred in the field itself. This assumption could be disregarded when revised induced seismicity locations are provided. If new or improved field data of any of the reservoir parameters is available this could alter the results and it is thus recommended to update the field data regularly.

To completely understand the translation between compaction in a reservoir and surface subsidence, porosity decrease during depletion and corresponding surface subsidence per field must be determined. This is not possible with the current data.

Additionally it could be interesting to investigate the relation between current vertical effective stress versus vertical strain in time for several fields (e.g. the high seismicity Roswinkel, Bergermeer and Groningen fields) to see whether the vertical effective stress versus vertical strain in time gives a linear or non-linear relation during the production of a field. The objective is hereby to determine whether a field has reached the inelastic part of the stress-strain curve. Vertical effective stress may be determined in time for some fields by using the production data of those fields. The change in vertical strain in time may however be difficult to obtain. This is because 1) current surface subsidence data may not be accurate and 2) no accurate surface subsidence data over time is publicly available.

An interesting further research topic would be to investigate the relation between fault characteristics and orientation and the occurrence of induced seismicity in higher detail for multiple fields. Detailed structural maps and accurate locations of seismic events are necessary to achieve an accurate result. In addition it could be interesting to examine whether clusters of seismic events occur at larger throw faults, that can be interpreted on seismic sections.

Since the thickness parameter provided non-conclusive results it would be useful to further examine this parameter with improved vertical strain data. In addition, with more information on pressure communication per field it can be determined whether to correlate the complete reservoir thickness or the thickness of the gas-bearing interval only. Following Van Eijs et al. (2006) and Holt et al. (2004) it could be worthwhile to determine the stiffness contrast for the 68 individual reservoirs and caprocks, since this contrast is thought to have a large influence on reservoir compaction and seismic potential.

A quantitative approach using statistical analysis is proposed for further research, such as logistic regression analysis and factor analysis. Logistic regression focuses on the effect of several independent variables upon one dependent variable, while factor analysis may detect latent variables.

10.2 Suggestions for Field Data Comparison with Laboratory Experiments

In an attempt to determine the translation between recent laboratory experiments and the field data in this study, a comparison between these data is made. To test the temporal delay in translation between the actual depletion of a field and the subsidence at the surface (Hettema et al. (2002)), surface subsidence data over time is essential. It is hence suggested to include the magnitude of surface subsidence in time for the 68 onshore gas fields examined in this study.

10.3 Suggestions for Analytical Model

The purpose of including a generic model for the behavior of a caprock and reservoir during depletion was to test hypotheses regarding field geometry and capture the mechanisms that operate during bending in a simple way. The aim was satisfied but several assumptions are involved and uncertainties occur. In order to reduce the uncertainty and improve the accuracy of the results by introducing a larger complexity, finite element modeling can be considered. Since several gas fields in the northern Netherlands are bounded at one or multiple sides by linear and perpendicular faults, it is suggested that

further analysis is performed on the configuration of a clamped rectangular plate. Additionally, the analytical model only describes the consequences for a variating length versus width ratio and area. It is hence suggested that thickness, for example, is assessed as well. At last, the assessment of length versus width ratio could not be performed in the literature assessment of equations representing reservoir compaction. It is suggested that an equation is constructed that includes the possibility of length versus width assessment, using thermal shrinkage as an analogue.

11 Acknowledgements

I would like to thank Prof. Dr. C.J. Spiers and Dr. S.J.T. Hangx for their help and guidance during this study, thereby helping me to pursue a steep learning curve regarding scientific research. Due to their effort I developed skills in data integration, time management, problem solving, pragmatical thinking and working independently.

12 References

Abdulaziz, M. (2014). Evaluation of microseismicity related to hydraulic fracking operations of petroleum reservoirs and its possible environmental repercussions. *Open Journal of Earthquake Research.*

Aldrich, J. (1995). Correlations genuine and spurious in Pearson and Yule. *Statistical Science*, (364-376).

Allen, D. R., Chilingar, G. V., Mayuga, M. N., and Sawabini, C. T. (1971). Study and prevention of subsidence. *Enciclopedia Delia Scienza E Delia Tecnica Mondadori.*

Anderson, R., Ratcliffe, I., Greenwell, H., Williams, P., Cliffe, S., and Coveney, P. (2010). Clay swelling - a challenge in the oilfield. *Earth-Science Reviews*, 98(3):201–216.

Athy, L. F. (1930). Density, porosity and compaction of sedimentary rocks. *American Association of Petroleum Geophysicists Bulletin*, 14:1–24.

Bonté, D., Van Wees, J.-D., and Verweij, J. (2012). Subsurface temperature of the onshore Netherlands: new temperature dataset and modelling. *Netherlands Journal of Geosciences, Geologie en Mijnbouw*, 91(4):491–515.

Bourne, S. J., Oates, S. J., Van Elk, J., and Doornhof, D. (2014). A seismological model for earthquakes induced by fluid extraction from a subsurface reservoir. *Journal of Geophysical Research: Solid Earth*, 119(12):8991–9015.

Breckels, I. M. and Van Eekelen, H. A. M. (1982). Relationship between horizontal stress and depth in sedimentary basins. *Journal of Petroleum Technology*, 34(9):2–191.

Breunese, J., Mijnlieff, H., and Lutgert, J. (2005). The life cycle of the Netherlands' natural gas exploration: 40 years after Groningen, where are we now? *Geological Society, London, Petroleum Geology Conference Series*, 6:69–75.

Brouwer, G. C. (1972). The Rotliegend in the Netherlands. *Rotliegend, Essays on European Lower Permian*, pages 34–42.

Bruns, B., Di Primio, R., Berner, U., and Littke, R. (2013). Petroleum system evolution in the inverted Lower Saxony Basin, northwest Germany: a 3D basin modeling study. *Geofluids*, 13(2):246–271.

Byerlee, J. (1978). Friction of rocks. *Pure and Applied Geophysicspplied geophysics*, 4-5(116):615–626.

Chilingarian, G. V., Donaldson, E. C., and Rieke, H. H. (1995). Subsidence due to fluid withdrawal. *Developments in Petroleum Science, 41. Elsevier Science.*

De Crook, T., Haak, H. W., and Dost, B. (1998). Seismisch risico in Noord-Nederland. *KNMI Technisch Rapport.*

Doornhof, D., Kristiansen, T. G., Nagel, N. B., Patillo, P. D., and Sayers, C. (2006). Compaction and subsidence. *Oilfield review*, 18(3):50–68.

Dost, B., Goutbeek, F., and Eck van T, K. D. (2012). Monitoring induced seismicity in the north of the Netherlands: status report 2010. vol. *WR.*

Duin, E. J. T., Doornenbal, J. C., Rijkers, R. H. B., Verbeek, J. W., and Wong, T. E. (2006). Subsurface structure of the Netherlands - results of recent onshore and offshore mapping. *Netherlands Journal of Geosciences, Geologie en Mijnbouw*, 85(4):245–276.

Engelder, T. and Fischer, M. P. (1994). Influence of poroelastic behavior on the magnitude of minimum horizontal stress, Sh, in overpressured parts of sedimentary basins. *Geology*, 22(10):949–952.

Fisher, Q. J., Casey, M., Clennell, M. B., and Knipe, R. J. (1999). Mechanical compaction of deeply buried sandstones of the North Sea. *Marine and Petroleum Geology*, 16(7):605–618.

Fisher, Q. J., Casey, M., Harris, S. D., and Knipe, R. J. (2003). Fluid-flow properties of faults in sandstone: the importance of temperature history. *Geology*, 31(11):965–968.

Fokker, P. A., Visser, K., Peters, E., Kunakbayeva, G., and Muntendam-Bos, A. (2012). Inversion of surface subsidence data to quantify reservoir compartmentalization: A field study. *Journal of Petroleum Science and Engineering*, 96:10–21.

Frohlich, C. (2012). Two-year survey comparing earthquake activity and injection-well locations in the Barnett shale, Texas. *Proceedings of the National Academy of Sciences*, 109(35):13934–13938.

Gaupp, R. and Okkerman, J. (2011). Diagenesis and reservoir quality of Rotliegend sandstones in the northern Netherlands - a review. *The Permian Rotliegend of the Netherlands. SEPM special publication, Tulsa*, 98:193–226.

Geertsma, J. (1973). Land subsidence above compacting oil and gas reservoirs. *Journal of Petroleum Technology*, 25(6):734–744.

Geluk, M. C. (1999). Late Permian (Zechstein) rifting in the Netherlands: models and implications for petroleum geology. *Petroleum Geoscience*, 5(2):189–199.

Geluk, M. C. (2007). Permian. *Geology of the Netherlands. Royal Netherlands Academy of Arts and Sciences*, pages 63–83.

Geluk, M. C., Wong, T. E., J, B. D. A., and De Jager, J. (2007). Geology of the netherlands: Triassic. *Royal Netherlands Academy of Arts and Sciences (KNAW)*, pages 85–106.

Hager, B. H. and Toksöz, M. N. (2009). Technical review of Bergermeer seismicity study.

Hangx, S. J. T., Spiers, C. J., and Peach, C. J. (2010). Mechanical behavior of anhydrite caprock and implications for CO_2 sealing capacity. *Journal of Geophysical Research: Solid Earth*, 115(B7):1978–2012.

Hantschel, T. and Kauerauf, A. (2009). Fundamentals of basin and petroleum systems modeling.

Herber, R. and De Jager, J. (2010). Oil and gas in the Netherlands: Is there a future? *Netherlands Journal of Geosciences, Geologie en Mijnbouw*, 89(2):119–135.

Hettema, M., Papamichos, E., and Schutjens, P. M. T. M. (2002). Subsidence delay: Field observations and analysis. *Oil & Gas Science and Technology*, 57(5):443–458.

Hettema, M. H. H., M, S. P. M. T., Verboom, B. J. M., and Gussinklo, H. J. (2000). Production-induced compaction of a sandstone reservoir: The strong influence of stress path. *SPE Reservoir Evaluation & Engineering*, 3(4):342–347.

Hol, S., Mossop, A. P., Van der Linden, A. J., Zuiderwijk, P. M. M., and Makurat, A. H. (2015). Long-term compaction behavior of Permian sandstones - An investigation into the mechanisms of subsidence in the Dutch Wadden Sea. *49th US Rock Mechanics/Geomechanics Symposium.*

Holt, R., Flornes, O., Li, L., and Fjær, E. (2004). Consequences of depletion-induced stress changes on reservoir compection and recovery. *Gulf Rocks 2004, the 6th North America Rock Mechanics Symposium (NARMS).*

Holtz, M. H. (2002). Residual gas saturation to aquifer influx: A calculation method for 3-D computer reservoir model construction. *SPE Gas Technology Symposium.*

Imrak, C. and Gerdemeli, I. (2007). A numerical method for clamped thin rectangular plates carrying a uniformly distributed load. *International Applied Mechanics*, 43(6):701–705.

Kanamori, H. (1983). Magnitude scale and quantification of earthquakes. *Tectonophysics*, 93(3):185–199.

KNMI (2015). Induced seismicity in the Netherlands.

Kombrink, H., Doornenbal, J. C., Duin, E. J. T., Den Dulk, M., Ten Veen, J. H., and Witmans, N. (2012). New insights into the geological structure of the netherlands; results of a detailed mapping project. *Netherlands Journal of Geosciences, Geologie en Mijnbouw*, 91(4):419–446.

Lorenz, J. C., Teufel, L. W., and Warpinski, N. R. (1991). Regional fractures: A mechanism for the formation of regional fractures at depth in flat-lying reservoirs. *AAPG bulletin*, 75(11):1714–1737.

Marketos, G., Govers, R., and Spiers, C. J. (2015). Ground motions induced by a producing hydrocarbon reservoir that is overlain by a viscoelastic rocksalt layer: a numerical model. *Geophysical Journal International*, 203(1):198–212.

McGarr, A. (2014). Maximum magnitude earthquakes induced by fluid injection. *Journal of Geophysical Research: Solid Earth*, 119(2):1008–1019.

McGarr, A., Simpson, D., and Seeber, L. (2002). Case histories of induced and triggered seismicity. *International Geophysics Series*, 81(A):647–664.

McGraw-Hill Education (2003). Mcgraw-hill dictionary of scientific and technical terms. *McGraw-Hill Professional: 6th edition.*

Mulders, F. M. M. (2003). Modelling of stress development and fault slip in and around a producing gas reservoir. *TU Delft, Delft University of Technology.*

NAM (2010). Bodemdaling door aardgaswinning, NAM gasvelden in Groningen, Friesland en het noorden van Drenthe: statusrapport 2010 en prognose tot het jaar 2070.

NAM (2013). Technical addendum to the Winningsplan Groningen 2013; Subsidence, induced earthquakes and seismic hazard analysis in the Groningen field.

Nash, W. and Cooley, I. (1959). Large deflections of a clamped elliptical plate subjected to uniform pressure. *Journal of Applied Mechanics*, 26(2):291–293.

Nelskamp, S., David, P., and Littke, R. (2008). A comparison of burial, maturity and temperature histories of selected wells from sedimentary basins in The Netherlands. *International Journal of Earth Sciences*, 97(5):931–953.

Nichols, G. (2009). Sedimentology and stratigraphy.

Nieuwland, D. A., Van Soest, W., and Den Boer, N. (2011). Structural geometry of the Bergermeer gas field: Implications for induced earthquake magnitudes.

NLOG (2005). Structuurkaarten.

Orlic, B. (2013). Site-specific geomechanical modeling for predicting stress changes around depleted gas reservoirs considered for CO_2 storage in the Netherlands. *47th US Rock Mechanics/Geomechanics Symposium.*

Pluymakers, A. M., Samuelson, J. E., Niemeijer, A. R., and Spiers, C. J. (2014). Effects of temperature and CO_2 on the frictional behavior of simulated anhydrite fault rock. *Journal of Geophysical Research: Solid Earth*, 119(12):8728–8747.

Ramm, M. (1992). Porosity-depth trends in reservoir sandstones: theoretical models related to Jurassic sandstones offshore Norway. *Marine and Petroleum Geology*, 9(5):553–567.

Roest, J. and Kuilman, W. (1994). Geomechanical analysis of small earthquakes at the Eleveld gas reservoir. *Rock Mechanics in Petroleum Engineering.*

Rutledge, J. T., Phillips, W. S., and Schuessler, B. K. (1998). Reservoir characterization using oil-production-induced microseismicity, Clinton County, Kentucky. *Tectonophysics*, 289(1):129–152.

Rutqvist, J., Birkholzer, J., and Tsang, C. (2008). Coupled reservoir-geomechanical analysis of the potential for tensile and shear failure associated with CO_2 injection in multilayered reservoir-caprock systems. *International Journal of Rock Mechanics and Mining Sciences*, 45(2):132–143.

Schutjens, P. M. T. M. (1991). Experimental compaction of quartz sand at low effective stress and temperature conditions. *Journal of the Geological Society*, 148(3):527–539.

Segall, P. (1989). Earthquakes triggered by fluid extraction. *Geology*, 17(10):942–946.

Segall, P. (1992). Induced stresses due to fluid extraction from axisymmetric reservoirs. *Pure and Applied Geophysics*, 139(3-4):535–560.

Segall, P. and Fitzgerald, S. D. (1998). A note on induced stress changes in hydrocarbon and geothermal reservoirs. *Tectonophysics*, 289(1):117–128.

Segall, P., Grasso, J., and Mossop, A. (1994). Poroelastic stressing and induced seismicity near the Lacq gas field, southwestern France. *Journal of Geophysical Research: Solid Earth*, 99(B8):15423–15438.

Timoshenko, S. and Woinowsky-Krieger, S. (1959). Theory of plates and shells.

Tipler, P. A. (1995). Physics for scientists and engineers. *Worth Publishers.*

Trautwein, U. and Huenges, E. (2005). Poroelastic behaviour of physical properties in Rotliegend sandstones under uniaxial strain. *International Journal of Rock Mechanics and Mining Sciences*, 42(7):924–932.

Van Eijs, R. M. H. E., Mulders, F. M. M., Nepveu, M., Kenter, C. J., and Scheffers, B. C. (2006). Correlation between hydrocarbon reservoir properties and induced seismicity in the Netherlands. *Elsevier.*

Van Wees, J., Stephenson, R., Ziegler, P., Bayer, U., McCann, T., Dadlez, R., Gaupp, R., Narkiewicz, M., Bitzer, F., and Scheck, M. (2000). On the origin of the southern Permian Basin, Central Europe. *Marine and Petroleum Geology*, 17(1):43–59.

Verweij, J., Simmelink, H., Underschultz, J., and Witmans, N. (2012). Pressure and fluid dynamic characterisation of the Dutch subsurface. *Netherlands Journal of Geosciences, Geologie en Mijnbouw*, 91(4):465–490.

Walderhaug, O. (1996). Kinetic modeling of quartz cementation and porosity loss in deeply buried sandstone reservoirs. *AAPG bulletin*, 80(5):731–745.

Wei-zang, C., Li-zhou, P., and Xiao-ming, L. (1992). Large deflection problem of a clamped elliptical plate subjected to uniform pressure. *Applied Mathematics and Mechanics*, 13(10):891–908.

Wiprut, D. and Zoback, M. D. (2000). Fault reactivation and fluid flow along a previously dormant normal fault in the northern North Sea. *Geology*, 28(7):595–598.

Young, W. C. and Budynas, R. G. (2002). Roark's formulas for stress and strain.

Zoback, M. (2010). Reservoir Geomechanics. *Cambridge University Press.*

13 Appendix 1

Table 16: *References used in field data collection.*

Reference number	Reference
1	NAM (2010)
2	Winningsplan Groningen 2013 (NAM)
3	Gaswinning vanaf de locaties Moddergat, Lauwersoog en Vierhuizen: Resultaten uitvoering meet- en regelcyclus 2007-2012 (NAM)
4	NAM (2013)
5	Geinduceerde aarbevingen Nederland 2014 (KNMI)
6	Winningsplan Anjum 2011 (NAM)
7	Winningsplan Annerveen 2003 (NAM)
8	Actualisatie winningsplan Annerveen 2011 (NAM)
9	Winningsplan Ameland 2011 (NAM)
10	Nieuwland et al. (2011)
11	Lecture Clemens Visser 2014 (NAM)
12	Wijziging Winningsplan Moddergat, Lauwersoog en Vierhuizen 2011 (NAM)
13	Aardbeving bij Smilde (Drenthe) 2005 (KNMI)
14	Winningsplan Kollum 2009 (NAM)
15	Winningsplan Assen 2009 (NAM)
16	Winningsplan Zevenhuizen 2004 (NAM)
17	Winningsplan Westerveld 2011 (NAM)
18	Annual Report 2003 (NLOG)
19	Deterministische hazard analyse voor geïnduceerde seismiciteit 2004 (TNO)
20	Bruns et al. (2013)
21	Nelskamp et al. (2008)
22	Winningsplan Harkema en Papekop 2009 (NAM)
23	Winningsplan Feerwerd, Houwerzijl, Kommerzijl, Leens, Munnekezijl, Saaksum Oost, Saaksum West, Boerakker, Pasop, Molenpolder, Sebaldeburen 2012 (NAM)
24	Winningsplan Grootegast, Kollummerland 2003 (NAM)
25	Winningsplan Oude Pekela, Blijham 2003 (NAM)
26	Winningsplan Surhuisterveen, Warffum 2003 (NAM)
27	Fokker et al. (2012)
28	Winningsplan Faan 2008 (NAM)
29	Winningsplan Bergermeer 2007 (BP)
30	Winningsplan Blija-Zuid 2011 (NAM)
31	Winningsplan Blija 2003 (NAM)
32	Opslagplan Grijpskerk 2003 (NAM)
33	Winningsplan Kielwindeweer 2003 (NAM)
34	Winningsplan Marum 2003 (NAM)
35	Winningsplan Tietjerksteradeel, Suawoude 2003 (NAM)
36	Winningsplan Gasselternijveen 2007 (NAM)
37	Opslagplan Norg 2003 (NAM)
38	Winningsplan Zuidwending-Oost 2005 (NAM)
39	Bergermeer Seismicity Study 2008 (TNO)
40	Hager and Toksöz (2009)
41	PGK Presentatie Bergermeer 2015 (TAQA)
42	EOW report TID-702 2008 (NAM)
43	EOW report WIT-02-S1 2007 (NAM)
44	KNMI (2015)
45	Dost et al. (2012)
46	Duin et al. (2006)

Table 17: *Field data of 68 onshore gas fields.*

Name	Field code	Structural map top reservoir available (Y/N)	Location	Reservoir type	Maximum burial depth (m)	Mean porosity	Compaction coefficient ($\cdot 10^{-5}\frac{1}{bar}$)	Present depth to reservoir top (m)	Reservoir thickness (m)	Reservoir temperature (°C)	Depth to GWC (m)	Production start	Production end	Initial gas pressure (bar)	Current gas pressure (bar)	Surface subsidence (cm)	Mean overburden density ($kg \cdot m^{-3}$)	Vertical overburden stress on reservoir top (MPa)	ΔP_f (MPa)	Vertical effective stress (MPa)	Type of primary caprock	Thickness of primary caprock (m)	Seismic (Y/N)	# induced earthquakes M_L>1.5	# induced earthquakes M_L>3	Maximum seismic magnitude	Total seismic moment (Nm)	Earthquake near fault zone (± 500 m) (Y/N)	Length field (m)	Width field m	Reference
Ameland-Noord	AMN	Y	AP	ROSLU	3350	0.115	0.8	3350	50	107	3388	1996	suspended	570	570	4	2255.03	74.11	0	74.11	Zechstein	1300	N	0	0	0	$1.26 \cdot 10^{9}$	N	7353	2353	3, 9, 11, 44, 46
Ameland-Oost	AME	Y	AP	ROSLU	3300	0.115	1	3300	110	110	3496	1986	producing	570	100	34.4	2254.50	72.10	47	119.10	Zechstein	1300	Y	2	0	1.8	$1.26 \cdot 10^{12}$	Y	12980	5329	3, 9, 44, 46
Ameland-Westgat	AWG	Y	AP	ROSLU	3250	0.115	0.8	3250	80	106	3360	1993	producing	570	300	10	2253.10	71.90	27	98.90	Zechstein	1300	N	0	0	0	$1.26 \cdot 10^{9}$	N	7532	1895	3, 9, 44, 46
Anjum	ANJ	Y	LT	ROSLU	3750	0.176	0.89	3750	51	136	3867	1997	producing	563	90	6	2271.94	83.58	47.30	130.89	Zechstein	750	N	0	0	0	$1.26 \cdot 10^{9}$	N	3829	3761	1, 3, 6, 44, 46
Annerveen	AVN	Y	LT GP LSB	Z2 RO	2780 2600-3200 4450/4650	0.117	0.36	2780	87	99	3080	1973	producing	346	15	10	2257.57	61.57	33.1	94.67	Zechstein	1000	Y	5	0	2.30	$1.38 \cdot 10^{13}$	Y	19179	6800	1, 4, 5, 7, 8, 18, 20, 44, 46
Appelscha	APS	Y	FP	RO	2640	0.173	0.52	2640	93	88	2672	1999	suspended	303	89	1	2262.67	58.60	21.4	80.00	Zechstein	800	Y	4	0	2.5	$3.99 \cdot 10^{12}$	Y	6039	1222	1, 13, 17, 46
Assen	ASN	Y	LT	RO	2880	0.145	0.52	2880	145	94	2943	2007	producing	337	186	1	2277.43	64.34	15.10	79.44	Zechstein	400	N	0	0	0	$1.26 \cdot 10^{9}$	N	4010	1470	1, 5, 15, 17, 44, 46
Bedum	BDM	Y	GP	RO	2875 2600 -3200	0.161	0.6	2875	220	102	3002	1985	producing	345	118	10	2252.39	63.53	22.7	86.21	Zechstein	1200	Y	1	0	1.6	$3.44 \cdot 10^{11}$	Y	12481	1581	1, 4, 5, 44, 46
Bergermeer	BGM	Y	CNB	RO	2800	0.223	0,3-1,1	2160	200	85	2227	1972	UGS	228	14.4	10.5	2282.64	48.37	21.36	69.73	Zechstein RBSH	250	Y	4	4	3.5	$4.23 \cdot 10^{14}$	Y	5771	1592	4, 10, 21, 29, 39, 40, 41, 45, 46
Blija Zuid	BLZ	Y	FP	ROSLU	2680	0.15	0.6	2680	112	100	2727	2012	producing	376	192	2	2264.76	59.54	18.40	77.94	Zechstein	750	N	0	0	0	$1.26 \cdot 10^{9}$	N	4060	1110	1, 30, 44, 46
Blija Zuid Oost	BLZO	Y	LT	ROSLU	2650	0.172	0.58	2650	102	97	2740 (GDT)	2001	producing	377	282	2	2255.99	58.65	9.5	68.15	Zechstein	1000	N	0	0	0	$1.26 \cdot 10^{9}$	N	3969	1644	1, 31, 44, 46
Blija-Ferwerderadeel	BLF	Y	FP	ROSLU	2550	0.167	0.49	2550	38	95	2670 (FWL)	1985	producing	377	262	2	2268.76	56.75	11.5	68.25	Zechstein	600	N	0	0	0	$1.26 \cdot 10^{9}$	N	6132	3917	1, 31, 44, 46
Blijham	BHM	Y	LSB	ROSL	4650	0.121	0.54	3396	70	115	3462	1984	producing	417	55	2	2277.52	64.79	36.20	100.10	Zechstein	400	N	0	0	0	$1.26 \cdot 10^{9}$	N	2737	1748	1, 20, 25, 44, 46
Boerakker	BRA	Y	LT	RO	2906	0.18	0.63	2906	190	103	2949	1998	producing	338	40	5	2258.98	64.40	29.80	94.20	Zechstein	1000	Y	0	0	0.9	$2.82 \cdot 10^{10}$	Y	5540	720	1, 5, 23, 44, 46
Een	EEN	Y	LT FP	ROCLT	2725	0.1017	0.54	2725	10	90	2682	2003	2007	299	131	1	2258.57	60.38	16.8	77.18	Zechstein	950	N	0	0	0	$1.26 \cdot 10^{9}$	N	6049	1442	1,17, 44, 46
Eleveld	ELV	Y	LT LSB	RO	3170 4650	0.132	0.50	3170	100	105	3290	1975	producing	377	25	2	2277.16	70.81	35.20	106.01	Zechstein	800	Y	8	0	2.7	$6.47 \cdot 10^{13}$	Y	3062	2013	1, 4, 5, 17, 18, 20, 44, 46
Engwierum	EWM	Y	LT	ROSL	3140	0.161	0.51	3140	103	119	3276	2002	2003	405	225	3	2258.42	69.57	18	87.57	Zechstein	1100	N	0	0	0	$1.26 \cdot 10^{9}$	N	1152	529	1, 14, 44, 46
Ezumazijl	EZZ	Y	LT	ROSLU	4000	0.151	0.69	4000	93	143	4083	1999	producing	493	91	5	2273.06	89.19	40.20	129.39	Zechstein	750	N	0	0	0	$1.26 \cdot 10^{9}$	N	4967	1951	1, 6, 44, 46
Faan	FAN	N	LT	ROSL	3275	0.156	0.51	3275	204	113	3355	2009	producing	387	300	2	2259.72	72.60	8.70	81.30	Zechstein	1100	N	0	0	0	$1.26 \cdot 10^{9}$	N	3012	1023	1, 28, 44, 46
Feerwerd	FRW	Y	GP LT	ROSL	3442	0.159	0.58	3442	115	120	3483	2000	producing	404	289	2	2258.57	76.26	11.50	87.76	Zechstein	1200	N	0	0	0	$1.26 \cdot 10^{9}$	N	3268	1151	1, 4, 23, 44, 46
Gasselternijveen	GSV	Y	LSB	Z2c	4450	0.146	0.3	3500	20	120	tilted contact 3575 -3450	2008	producing	565	300	1	2273.22	78.05	26.5	104.55	Zechstein	650	N	0	0	0	$1.26 \cdot 10^{9}$	N	2115	2067	1, 20, 36, 44, 46
Grijpskerk UGS	GRK	Y	LT	RO	3300	0.187	0.49	3300	223	118	3390	1993	UGS	393	370	4	2262.67	73.25	2.30	75.55	Zechstein	1000	Y	1	0	1.5	$2.24 \cdot 10^{11}$	Y	3538	2810	1, 32, 44, 46
Groningen	GRO	Y	GP	DC RO	2600 -3200	0.19	0.63	2750 -2900	110 -300	99	2971 -3016	1963	producing	347	105	35	2260.00	62.63	24.20	86.83	Basal Zechstein	50	Y	188	4	3.6	$1.00 \cdot 10^{16}$	Y	49213	30640	1, 2, 4
Grootegast	GGT	Y	LT	ROSL	2790	0.191	0.66	2790	87	98	2897	1979	producing	334	60	4	2254.47	61.70	27.4	89.10	Zechstein	1100	N	0	0	0	$1.26 \cdot 10^{9}$	N	3255	2134	1, 24, 44, 46
Harkema	HRK	N	FP	RO	2570	0.15	0.56	2570	60	95	2618 (FWL)	2010	producing	295	291	2	2267.18	57.16	0.40	57.56	Zechstein	650	N	0	0	0	$1.26 \cdot 10^{9}$	N	3032	1191	1, 22, 42, 46
Houwerzijl	HOU	Y	LT	ROSLU	3581	0.186	0.58	3581	118	126	3648	2000	producing	423	224	4.7	2262.30	79.47	19.90	99.37	Zechstein	1100	Y	0	0	1.4	$1.58 \cdot 10^{11}$	Y	3939	1241	1, 3, 23, 44, 46
Kielwindeweer	KWR	Y	GP	ROSL	3220	0.091	0.46	3220	115	106	3308	2003	producing	381	231	2	2256.41	71.28	15	86.28	Zechstein	1200	N	0	0	0	$1.26 \cdot 10^{9}$	N	2894	1498	1, 4, 5,18, 33, 44, 46
Kollum	KLM	Y	LT	ROSLU	3210	0.166	0.48	3210	94	116	3316	2002	producing	440	343	3	2256.31	71.05	9.70	80.75	Zechstein	1200	N	0	0	0	$1.26 \cdot 10^{9}$	N	5121	2764	1, 14, 44, 46
Kollum Noord	KLMN	Y	LT	ROSLU	3200	0.195	0.58	3200	99	117	3310 (FWL)	2001	producing	442	131	4.5	2259.01	70.91	31.1	102.01	Zechstein	1100	N	0	0	0	$1.26 \cdot 10^{9}$	N	5510	1022	1, 3, 14, 44, 46
Kollumerland	KOL	Y	LT	ROSL	2940	0.166	0.64	2940	90	101	2966	1989	producing	343	45	3	2253.23	64.99	29.80	94.79	Zechstein	1200	N	0	0	0	$1.26 \cdot 10^{9}$	N	3694	1844	1, 24, 44, 46
Kommerzijl	KMZ	Y	LT	RO	3476	0.18	0.59	3476	183	122	3535	2001	producing	410	194	4	2267.93	77.34	21.60	98.94	Zechstein	850	N	0	0	0	$1.26 \cdot 10^{9}$	N	2043	974	1, 23, 44, 46
Lauwersoog-C	LWOC	Y	AP LT	ROSLU	3970	0.103	0.40	3970	95	144	4058	2008	producing	500	500	1	2266.14	88.26	0	88.26	Zechstein	1050	N	0	0	0	$1.26 \cdot 10^{9}$	N	1772	1055	1, 12, 44, 46
Lauwersoog-Oost	LWOO	Y	AP	ROSLU	3975	0.1028	0.4	3975	95	143	4073	2008	producing	480	450	1	2266.17	88.37	3	91.37	Zechstein	1050	N	0	0	0	$1.26 \cdot 10^{9}$	N	4109	3894	1, 12, 44, 46
Lauwersoog-West	LWOW	Y	LT	ROSLU	3910	0.1028	0.4	3910	90	144	4055	2008	producing	479	450	1	2271.52	87.13	2.90	90.03	Zechstein	800	N	0	0	0	$1.26 \cdot 10^{9}$	N	4691	1615	1, 12, 44, 46

Name	Field code	Structural map top reservoir available (Y/N)	Location	Reservoir type	Maximum burial depth (m)	Mean porosity	Compaction coefficient ($\cdot 10^{-5}\frac{1}{bar}$)	Present depth to reservoir top (m)	Reservoir thickness (m)	Reservoir temperature (°C)	Depth to GWC (m)	Production start	Production end	Initial gas pressure (bar)	Current gas pressure (bar)	Surface subsidence (cm)	Mean overburden density ($kg \cdot m^{-3}$)	Vertical overburden stress on reservoir top (MPa)	ΔP_f (MPa)	Vertical effective stress (MPa)	Type of primary caprock	Thickness of primary caprock (m)	Seismic (Y/N)	# induced earthquakes M_L>1.5	# induced earthquakes M_L>3	Maximum seismic magnitude	Total seismic moment (Nm)	Earthquake near fault zone (± 500 m) (Y/N)	Length field (m)	Width field m	Reference
Leens	LNS	Y	GP	ROSLU	3620	0.196	0.59	3620	123	125	3646	2003	producing	424	221	3.8	2262.60	80.35	20.30	100.65	Zechstein	1100	N	0	0	0	$1.26 \cdot 10^9$	N	3092	994	1, 3, 4, 23, 44, 46
Marum	MAR	Y	FP	ROSL	2430	0.146	0.45	2430	121	90	2482	1978	producing	281	146	5	2267.72	54.06	13.5	67.56	Zechstein	600	N	0	0	0	$1.26 \cdot 10^9$	N	5282	1803	1, 34, 44, 46
Marumerlage	MAL	Y	FP	ROSL	2475	0.195	0.42	2475	128	92	2551	-	undeveloped, production start expected within 5 years	287	245	2	2262.67	54.94	4.20	59.14	Zechstein	750	N	0	0	0	$1.26 \cdot 10^9$	N	2932	2257	1, 44, 46
Metslawier	MET	Y	LT	ROSLU	3653	0.185	0.98	3653	44	133	3728 (FWL)	1997	ceased	559	100	4.60	2261.61	81.05	45.90	126.95	Zechstein	1150	Y	0	0	1.4	$1.59 \cdot 10^{11}$	N	2979	2624	1, 3, 6, 44, 46
Moddergat	MGT	Y	LT	ROSLU	3685	0.15	0.3	3685	105	138	3885	2007	producing	567	535	3.5	2276.50	82.30	3.20	85.50	Zechstein	550	N	0	0	0	$1.26 \cdot 10^9$	N	4757	3515	1, 3, 12, 44, 46
Molenpolder	MPR	Y	LT	ROSLU	3144	0.21	0.54	3144	92	107	3195	2001	producing	424	163	4	2258.50	69.67	26.10	95.76	Zechstein	1100	N	0	0	0	$1.26 \cdot 10^9$	N	3648	1209	1, 23, 44, 46
Munnekezijl	MKZ	Y	LT	ROSLU	3550	0.16	0.56	3550	110	128	3650	1995	producing	424	120	7.1	2259.52	78.69	30.40	109.09	Zechstein	1200	N	0	0	0	$1.26 \cdot 10^9$	N	7148	2704	1, 3, 23, 44, 46
Nes	NES	Y	LT	ROSLU	3680	0.143	0.3	3680	105	132	3731	2007	producing	564	516	3.5	2266.71	81.83	4.80	86.63	Zechstein	950	N	0	0	0	$1.26 \cdot 10^9$	N	5485	2688	1, 3, 12, 44
Norg UGS	NOR	Y	LT	ROSL	2650	0.15	0.49	2650	169	96	2847	1983/1995	UGS	327	305	2	2259.38	58.74	2.20	60.94	Zechstein	900	Y	1	0	1.5	$2.80 \cdot 10^{11}$	Y	17475	2271	1, 37, 44, 46
Norg-Zuid	NRZ	Y	LT	RO	2700	0.112	0.45	2700	142	95	2783	1999	ceased	317	90	3	2249.96	59.59	22.70	82.29	Zechstein	1200	N	0	0	0	$1.26 \cdot 10^9$	N	3159	2222	1, 17, 44, 46
Oostrum	OSM	Y	LT	RO	3450	0.157	0.6	3450	99	123	3534	2002	producing	522	137	2.4	2256.04	76.35	38.5	114.85	Zechstein	1300	N	0	0	0	$1.26 \cdot 10^9$	N	2446	1160	1, 3, 14, 44, 46
Opende-Oost	OPO	Y	FP	RO	2495	0.171	0.64	2495	147	93	2570	1993	producing	292	137	3	2262.89	55.39	15.50	70.89	Zechstein	750	N	0	0	0	$1.26 \cdot 10^9$	N	3518	1280	1, 34, 44, 46
Oude Pekela	OPK	Y	LSB	RO	4650	0.139	0.57	2880	66	98	3000	1995	producing	331	33	4	2279.00	64.39	29.8	94.19	Zechstein	350	N	0	0	0	$1.26 \cdot 10^9$	N	3302	1468	1, 5, 25, 44, 46
Pasop	PSP	Y	LT	ROCLT	3090	0.115	0.61	3090	173	106	3123	1997	producing	358	164	6	2263.73	68.62	19.40	88.02	Zechstein	900	N	0	0	0	$2.82 \cdot 10^{10}$	Y	3985	765	1, 23, 44, 46
Roden (blok 1)	ROD	Y	LT	RO	2950	0.151	0.47	2950	191	101	3021	1976	suspended	345	89	2	2257.91	65.34	25.6	90.94	Zechstein	1050	Y	1	0	2.1	$1.82 \cdot 10^{12}$	Y	5879	1510	1, 5, 17, 44, 46
Roden (blok 2)	ROD	Y	LT	RO	2950	0.151	0.47	2950	191	101	3021	1976	suspended	345	270	2	2256.39	65.30	7.5	72.80	Zechstein	1100	N	0	0	0	$1.26 \cdot 10^9$	N	2853	1059	1, 5, 17, 44, 46
Rodewolt	RDW	Y	GP	RO	3080 (2600-3200)	0.173	0.54	3080	227	111	3140	-	undeveloped, production start expected within 5 years	351	342	10	2257.81	68.22	0.90	69.12	Zechstein	1100	Y	0	0	1.2	$7.94 \cdot 10^{10}$	Y	2920	500	1, 4, 44, 46
Roswinkel	RSW	Y	LSB	RBM	4250	0.20	1.50	2100	210	85	2280	1980	suspended (2005)	331	290	17	2281.49	47.00	4.10	51.10	RNSOC and Rotliegend Evaporites	1200	Y	22	3	3.4	$4.86 \cdot 10^{14}$	Y	11778	2870	4, 5, 20, 27
Saaksum (O)	SSM	Y	LT	ROSLU SL	3446	0.1641	0.19	3446	127	123	3528	1999	producing	412	207	4	2261.22	76.44	20.5	96.94	Zechstein	1100	Y	0	0	1.3	$1.12 \cdot 10^{11}$	Y	3366	2398	1, 23, 44, 46
Saaksum (W)	SSM	Y	LT GP	ROSLU SL	3514	0.1641	0.19	3514	120	122	3528	1999	producing	412	200	5	2264.33	78.06	21.20	99.26	Zechstein	1000	Y	0	0	1	$3.98 \cdot 10^{10}$	Y	3737	1378	1, 23, 44, 46
Sebaldeburen	SEB	Y	LT	ROSLU	2844	0.151	0.58	2844	173	100	2949	1997	producing	338	50	4	2259.09	63.028	28.80	91.83	Zechstein	975	N	0	0	0	$1.26 \cdot 10^9$	N	2915	691	1, 23, 44, 46
Snawoude	SUW	Y	FP	KNNS RO	2440	0.141	1.05	2440	143	77 90	2486	1984	producing	283	53	11	2267.81	54.28	23	77.28	Zechstein	600	N	0	0	0	$1.26 \cdot 10^9$	N	5735	1162	1, 35, 44, 46
Surhuisterveen	SHV	Y	FP	RO	2550	0.143	0.63	2550	85	94	2571	2008	producing	292	144	2	2267.00	56.71	14.80	71.51	Zechstein	650	N	0	0	0	$1.26 \cdot 10^9$	N	2938	586	1, 26, 44, 46
Tietjerksteradeel RO	TID	Y	FP	ROSL	2400	0.192	0.95	2400	140	92	2500	1974	producing	284	47	14	2269.31	53.43	23.70	77.13	Zechstein	550	N	0	0	0	$1.26 \cdot 10^9$	N	10400	4000	1, 22, 35, 44
Tietjerksteradeel KNNS	TID	Y	FP	KNNS	1940	0.147	1.40	1940	30	78	1952	1977	producing	221	20	14	2286.63	43.52	20.10	63.62	KNNC	71	Y	1	0	1.8	$6.31 colot 10^{11}$	N	12000	5250	1, 35, 44
Ureterp	URE	Y	FP	ROSL	2400	0.957	0.61	2400	125	90	2473.5	1978	producing	281	55	6	2269.31	53.43	22.6	76.03	ROCLT	550	Y	0	0	1	$3.98 \cdot 10^{10}$	Y	8241	1237	1, 18, 34, 44, 46
Usquert	USQ	Y	GP	ROSL	2950 2600-3200	0.196	0.50	2950	232	108	2972	-	undeveloped, production start expected within 5 years	347	318	10	2257.91	65.34	2.90	68.24	Zechstein	1050	N	0	0	0	$1.26 \cdot 10^9$	N	2343	2243	1, 4, 5, 44, 46
Vierhuizen (Oost)	VHN	Y	LT	ROSLU	3900	0.147	0.50	3900	91	138	3930	2008	producing	459	459	2.6	2264.56	86.64	0	86.64	Zechstein	1100	N	0	0	0	$1.26 \cdot 10^9$	N	3165	1132	1, 3, 12, 44, 46
Vries (North)	VRSN	Y	LT	ROSL	3100	0.104	0.60	3100	140	103	3108	1991	producing	356	164	6	2263.81	68.84	19.2	88.04	Zechstein	900	Y	2	0	1.9	$1.86 \cdot 10^{12}$	Y	4001	3000	1, 5, 17, 44, 46
Vries (South)	VRSZ	Y	LT	ROSL	3090	0.104	0.45	3090	140	101	3149	1991	producing	362	84	6	2272.46	68.88	27.80	96.68	Zechstein	600	Y	1	0	1.5	$2.24 \cdot 10^{11}$	Y	6685	1287	1, 5, 17, 44, 46
Warffum	WRF	Y	GP	ROSL	2944 2600 -3200	0.198	0.67	2944	213	105	3043	1986	producing	357	212	9	2257.85	65.21	14.5	79.71	Zechstein	1050	Y	0	0	1.1	$5.62 \cdot 10^{10}$	Y	4496	2051	1, 4, 5, 26, 44, 46
Witterdiep	WTP	N	FP	ROSL	3500	0.110	0.45	3500	122	99	3600	2007	producing	341	59	2	2273.22	78.05	28.20	106.25	Zechstein	650	Y	1	0	1.7	$4.47 \cdot 10^{11}$	Y	3874	426	1, 17, 43, 44, 46
Zevenhuizen	ZVH	Y	FP LT	ROCLT	2600	0.153	0.57	2600	14	95	2693	2008	producing	306	35	1	2251.88	57.44	27.1	84.54	Zechstein	1100	N	0	0	0	$1.26 \cdot 10^9$	N	2683	1608	1, 5, 16, 17, 46
Zuidwending-Oost	ZWDE	N	LSB	ROSL	4650	0.124	0.54	2900	70	95	3000	2006	producing	347	137	6	2279.07	64.84	21	85.84	Zechstein	350	Y	1	0	1.6	$3.16 \cdot 10^{11}$	Y	1853	1302	1, 20, 38, 44, 46

14 Appendix 2

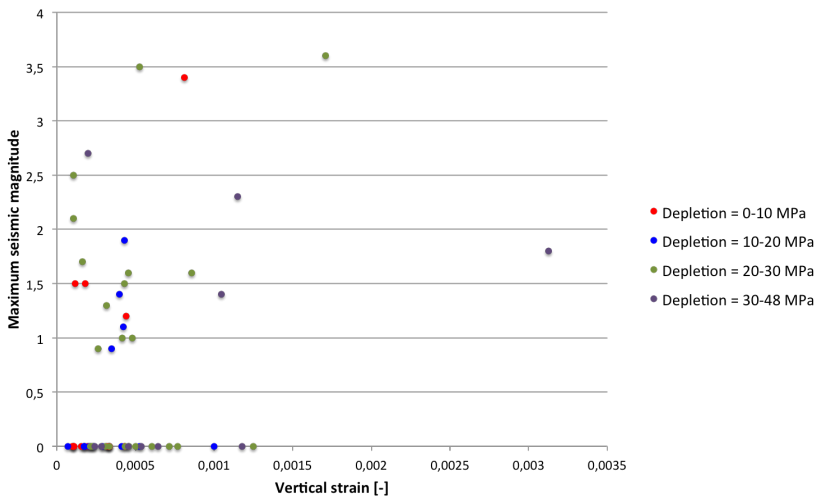

Figure 73: *Maximum seismic magnitude (Richter scale) versus vertical strain for 63 onshore gas fields.*

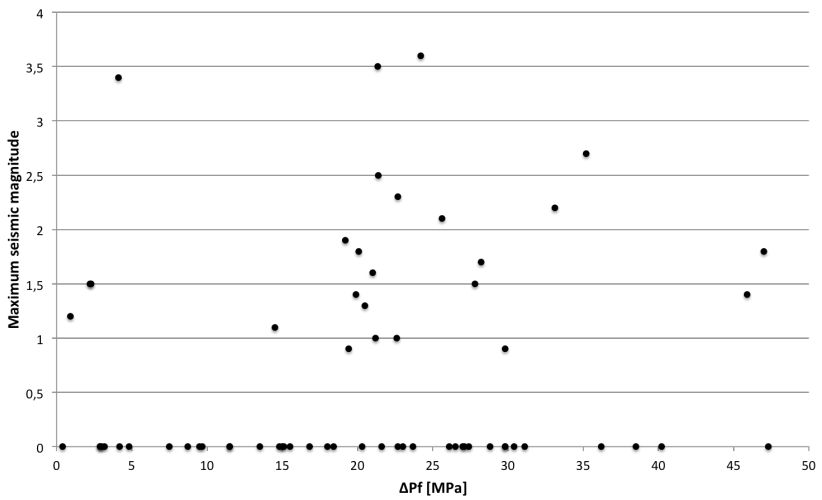

Figure 74: *Maximum seismic magnitude (Richter scale) versus ΔP_f for 65 onshore gas fields.*

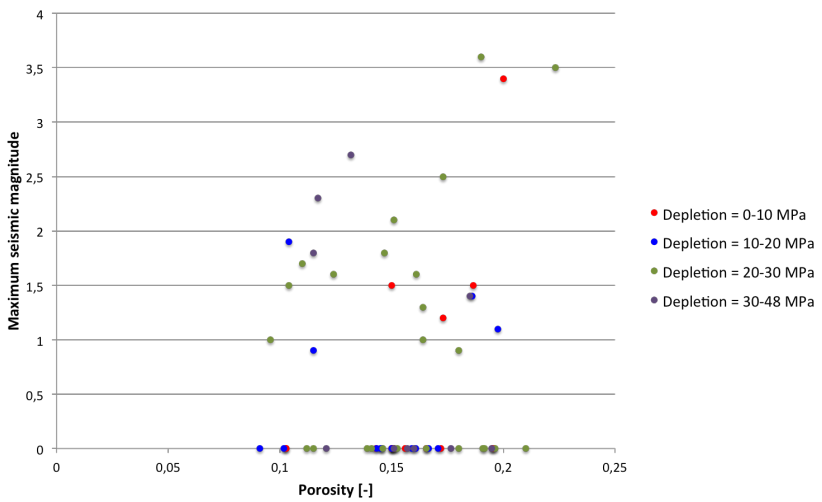

Figure 75: *Maximum seismic magnitude (Richter scale) versus mean porosity for 65 onshore gas fields.*

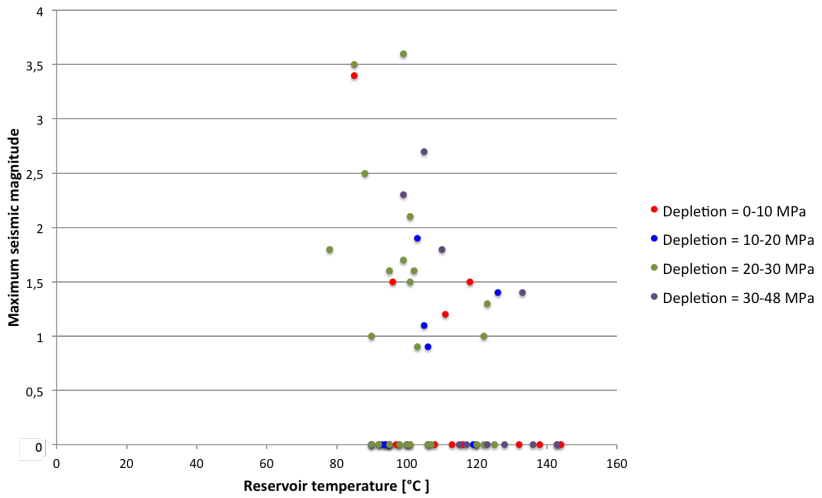

Figure 76: *Maximum seismic magnitude (Richter scale) versus reservoir temperature for 65 onshore gas fields.*

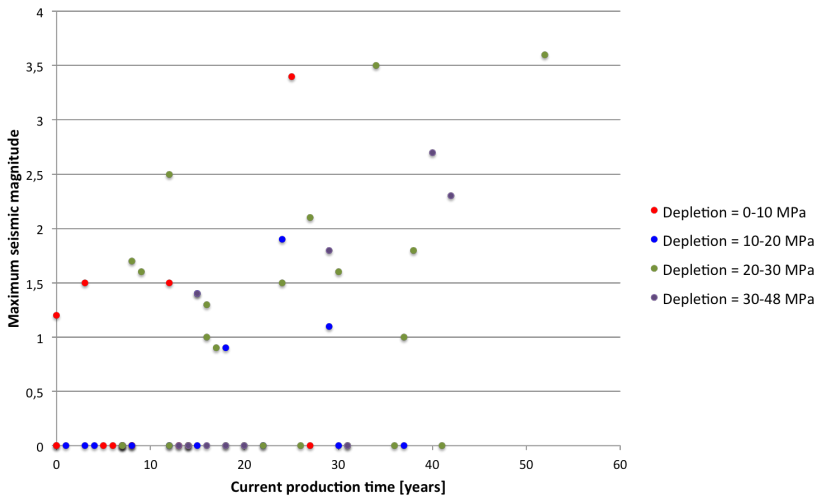

Figure 77: *Maximum seismic magnitude (Richter scale) versus current production time for 65 onshore gas fields.*

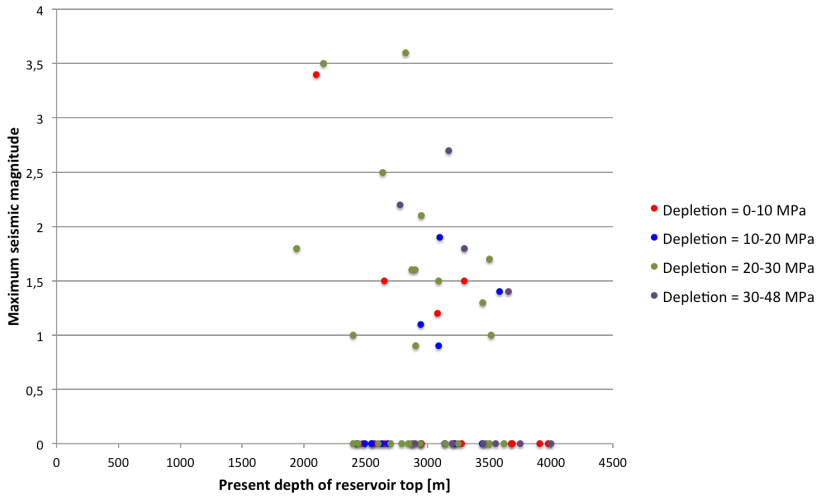

Figure 78: *Maximum seismic magnitude (Richter scale) versus present depth of reservoir top for 65 onshore gas fields.*

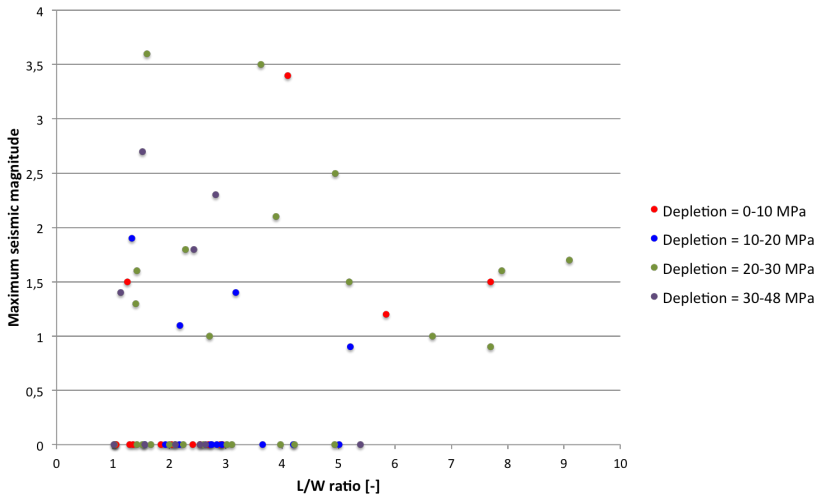

Figure 79: *Maximum seismic magnitude (Richter scale) versus L/W ratio for 65 onshore gas fields.*

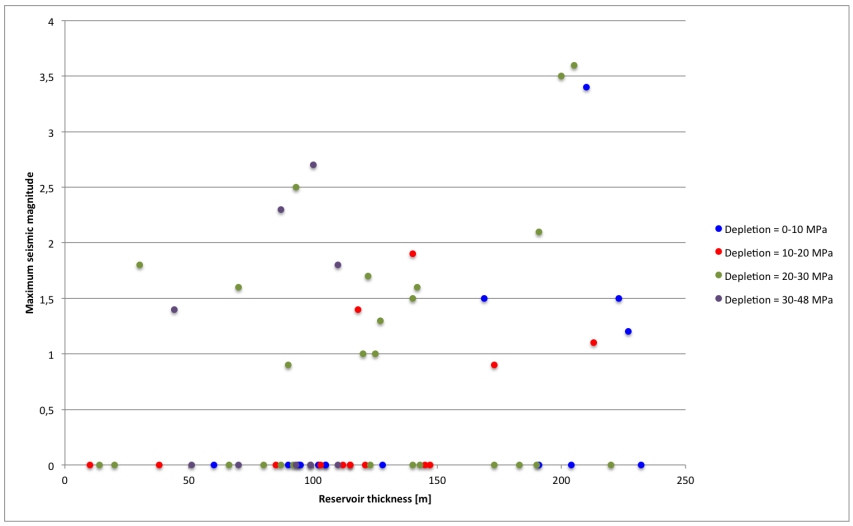

Figure 80: *Maximum seismic magnitude (Richter scale) versus reservoir thickness for 65 onshore gas fields.*

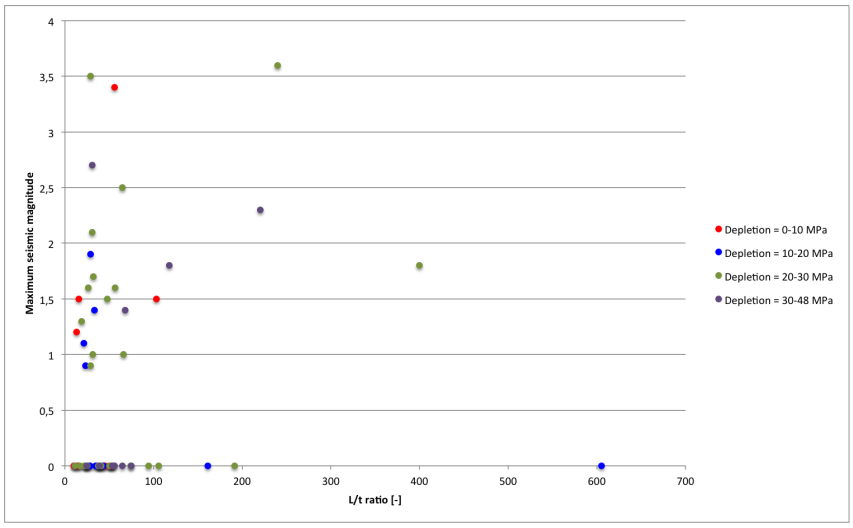

Figure 81: *Maximum seismic magnitude (Richter scale) versus L/t ratio for 65 onshore gas fields.*

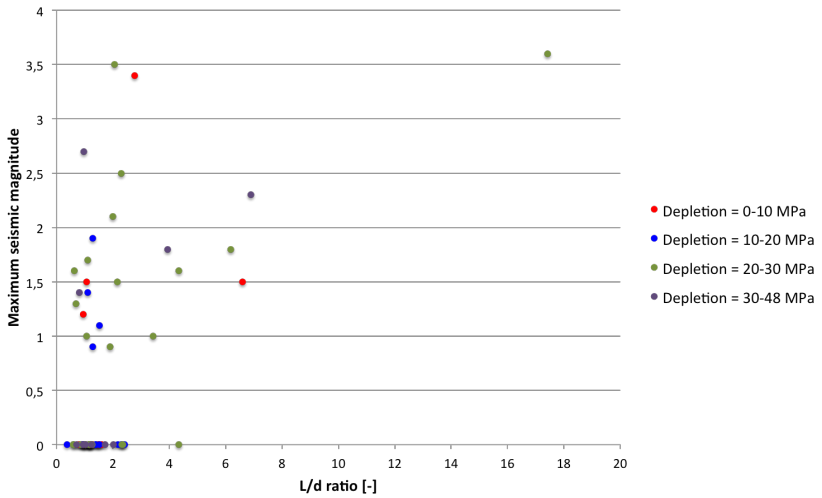

Figure 82: *Maximum seismic magnitude (Richter scale) versus L/d ratio for 65 onshore gas fields.*

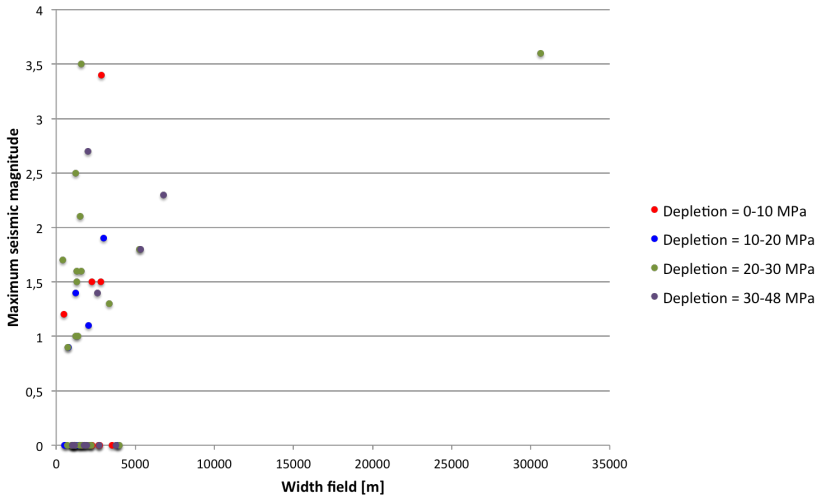

Figure 83: *Maximum seismic magnitude (Richter scale) versus field width for 64 onshore gas fields.*

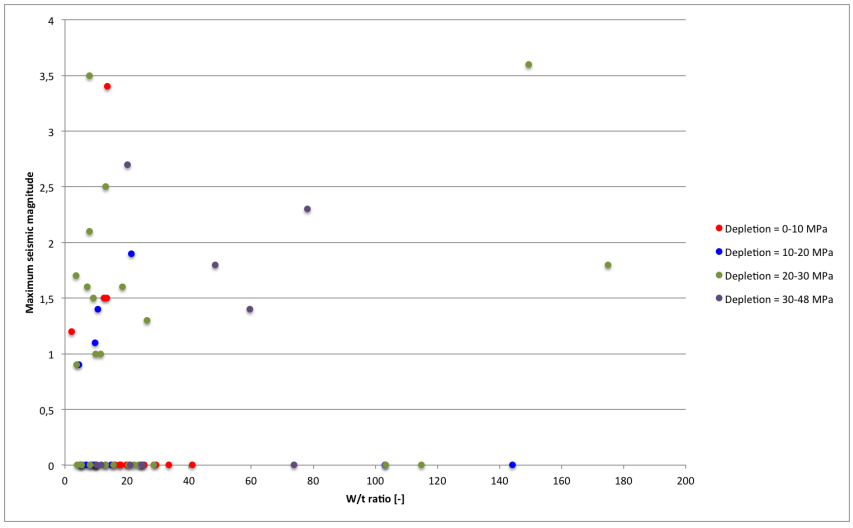

Figure 84: *Maximum seismic magnitude (Richter scale) versus W/t ratio for 65 onshore gas fields.*

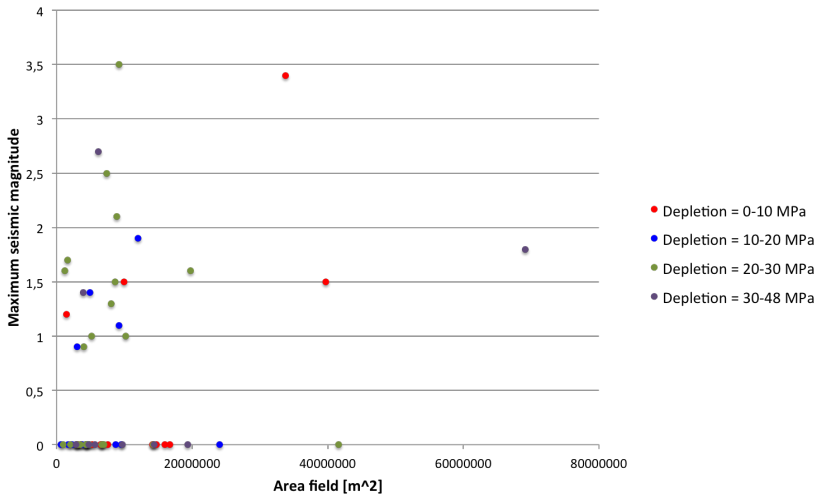

Figure 85: *Maximum seismic magnitude (Richter scale) versus field area for 63 onshore gas fields.*

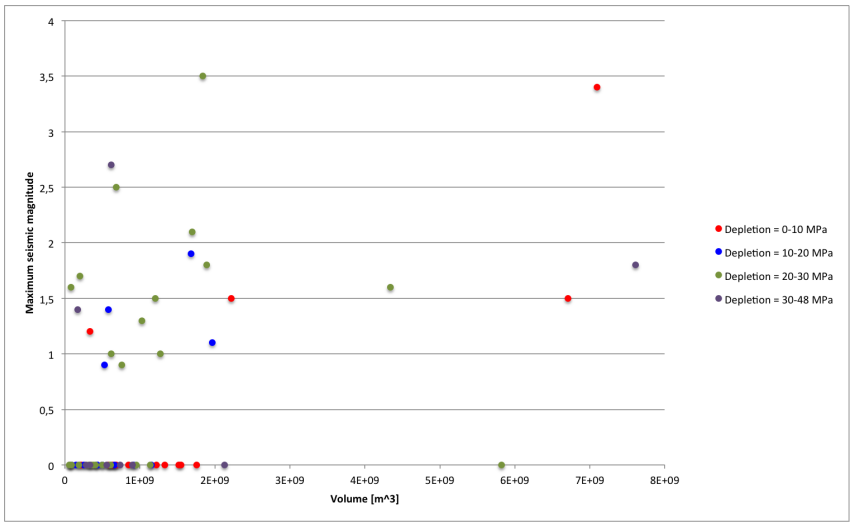

Figure 86: *Maximum seismic magnitude (Richter scale) versus field volume for 63 onshore gas fields.*

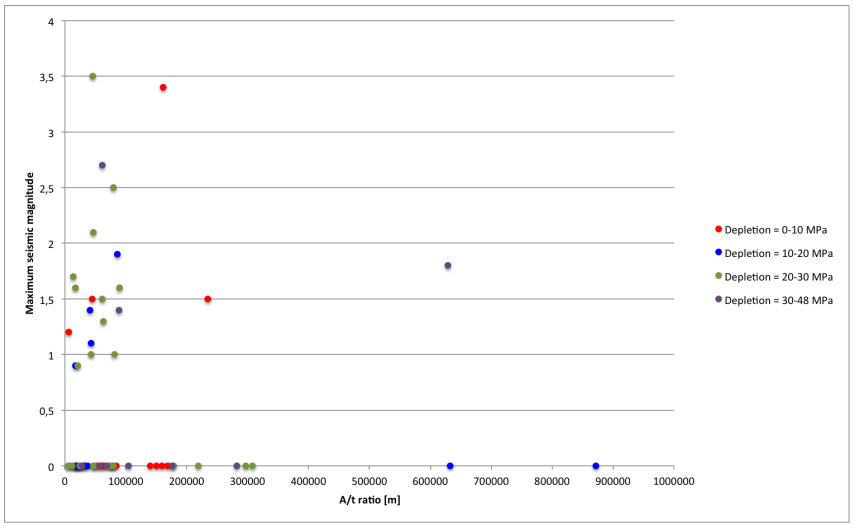

Figure 87: *Maximum seismic magnitude (Richter scale) versus A/t ratio for 62 onshore gas fields.*

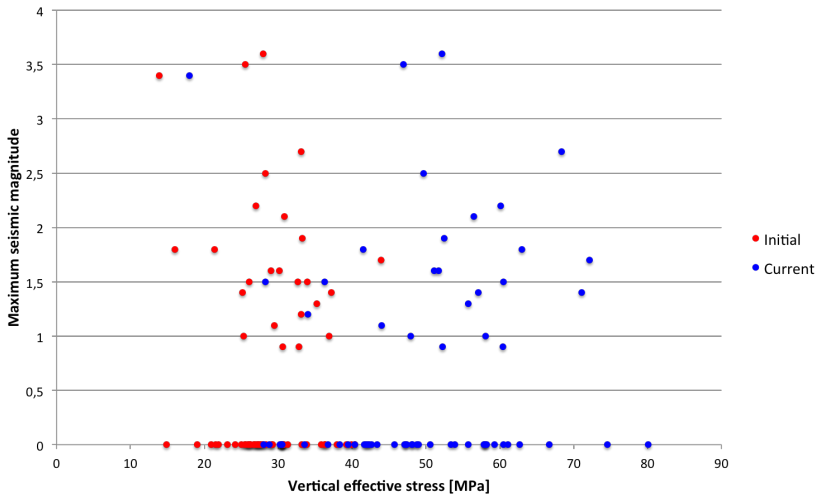

Figure 88: *Maximum seismic magnitude (Richter scale) versus the vertical effective stress (initial and current) of 65 onshore gas fields.*

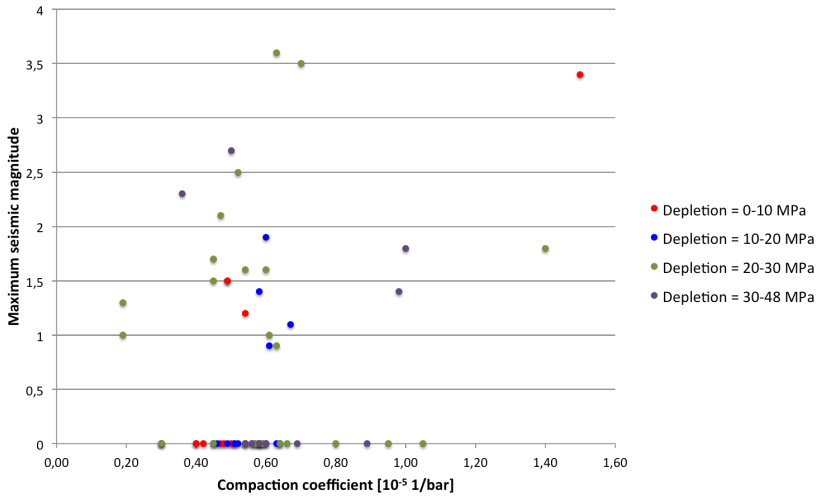

Figure 89: *Maximum seismic magnitude (Richter scale) versus the uniaxial compaction coefficient for 65 onshore gas fields.*

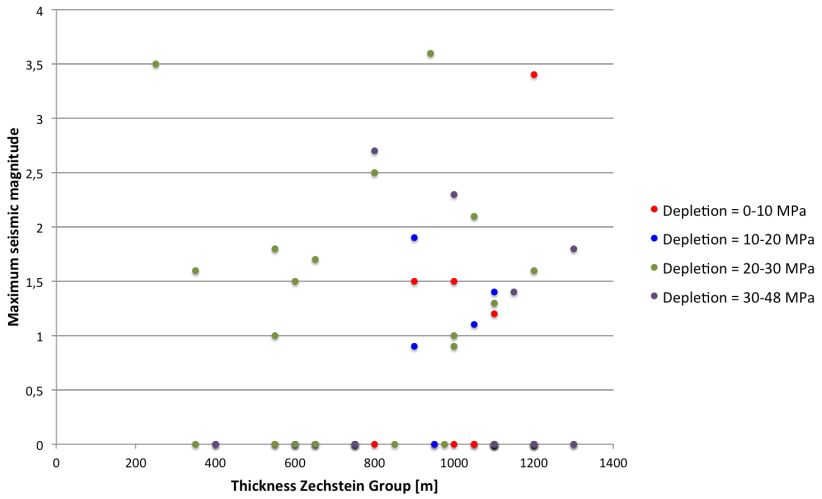

Figure 90: *Maximum seismic magnitude (Richter scale) versus Zechstein Group thickness for 65 onshore gas fields.*

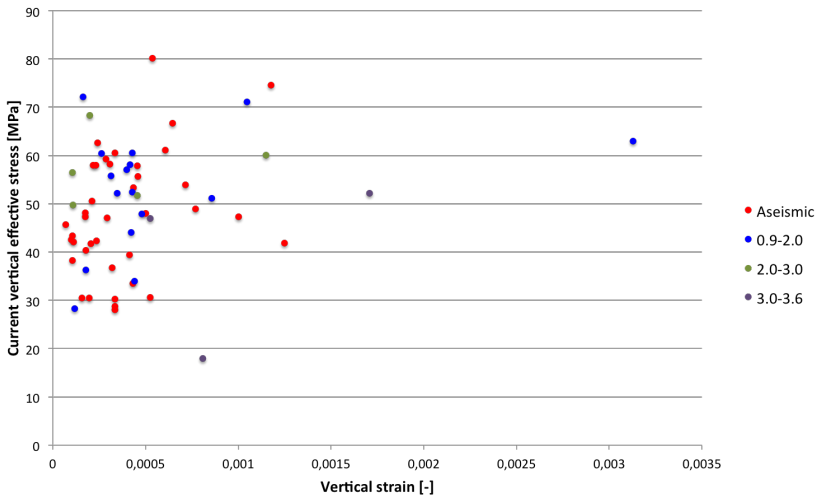

Figure 91: *Current vertical effective stress versus vertical strain for 63 onshore gas fields, subdivided into maximum seismic magnitude interval (Richter scale).*

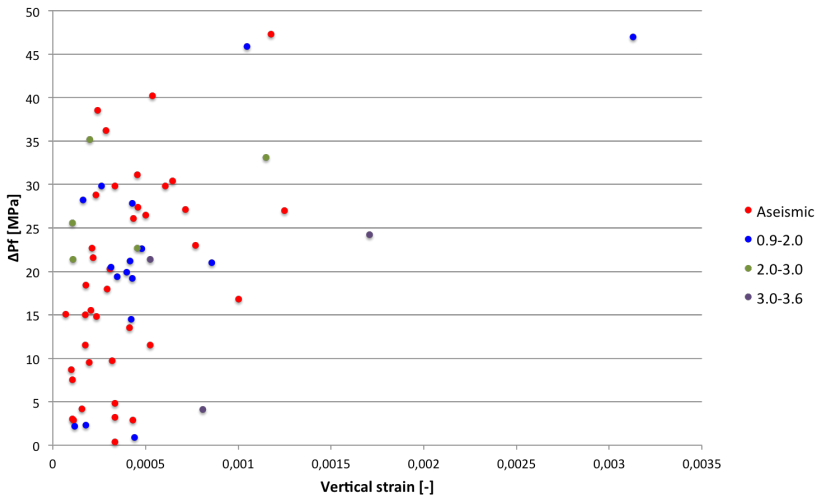

Figure 92: ΔP_f *versus vertical strain for 63 onshore gas fields, subdivided into maximum seismic magnitude interval (Richter scale).*

15 Appendix 3

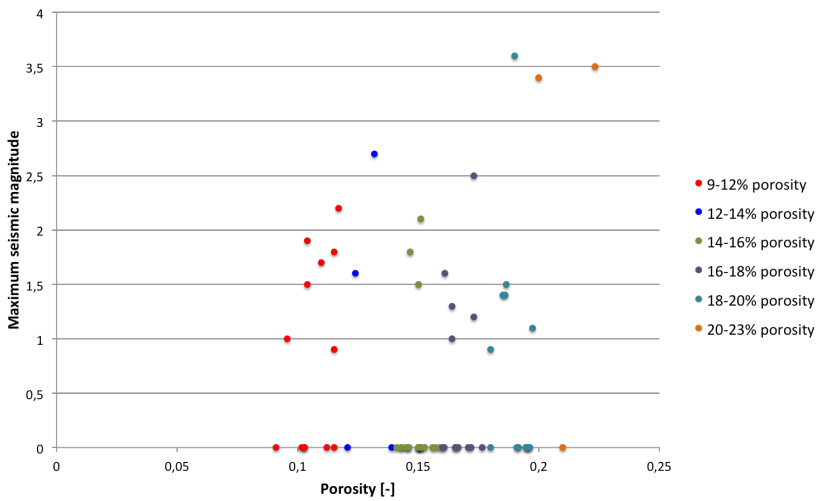

Figure 93: *Maximum seismic magnitude (Richter scale) versus mean porosity for 65 onshore gas fields, subdivided into porosity range.*

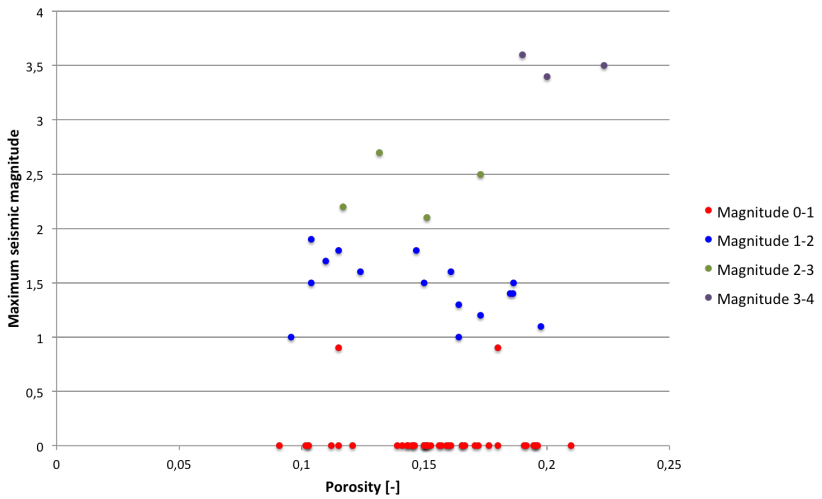

Figure 94: *Maximum seismic magnitude (Richter scale) versus mean porosity for 65 onshore gas fields, subdivided into maximum seismic magnitude range.*

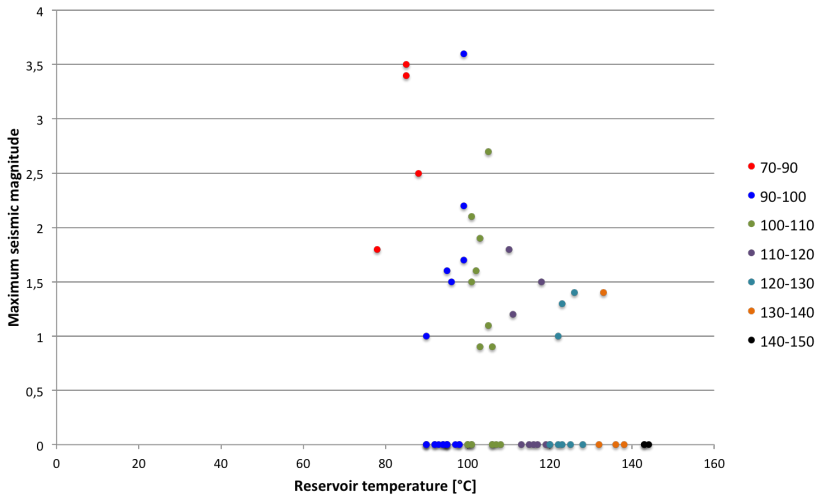

Figure 95: *Maximum seismic magnitude (Richter scale) versus temperature for 65 onshore gas fields, subdivided into temperature range.*

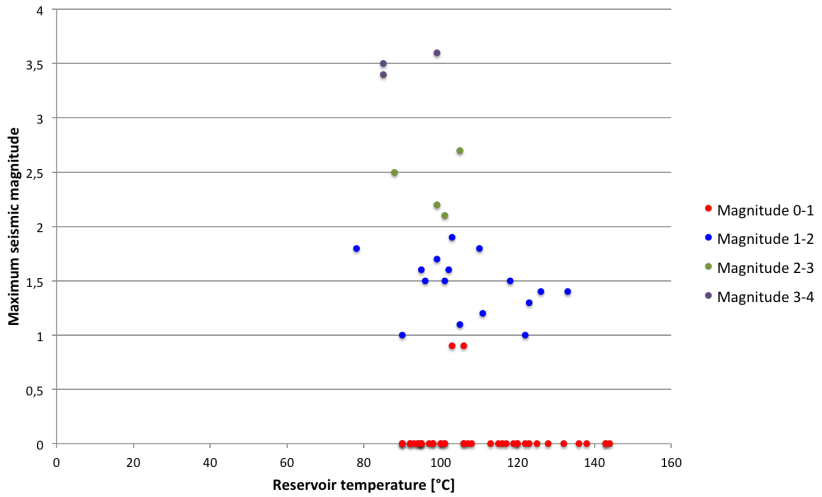

Figure 96: *Maximum seismic magnitude (Richter scale) versus temperature for 65 onshore gas fields, subdivided into maximum seismic magnitude range.*

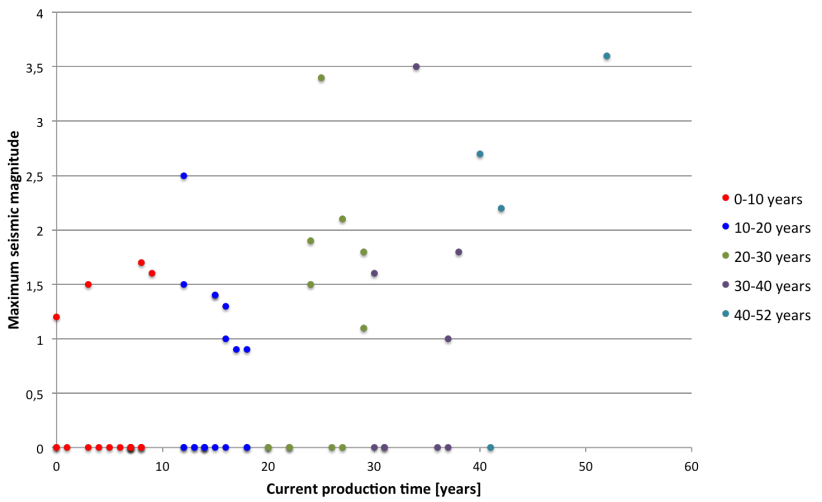

Figure 97: *Maximum seismic magnitude (Richter scale) versus current production time for 65 onshore gas fields, subdivided into production time range.*

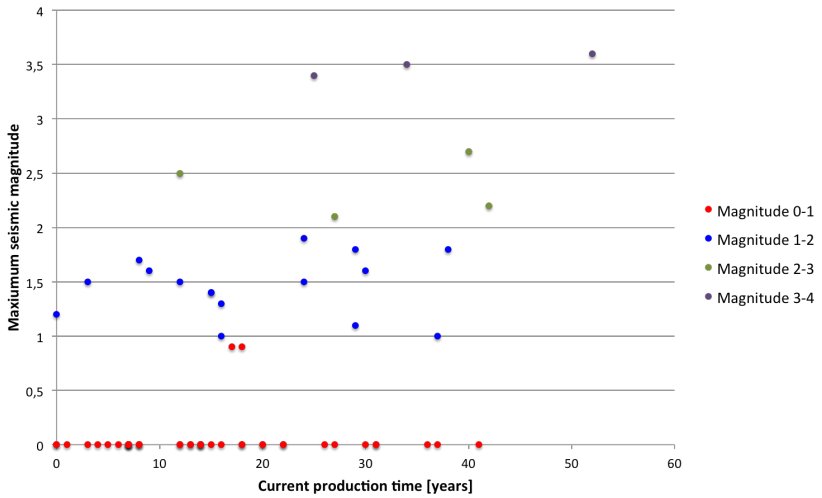

Figure 98: *Maximum seismic magnitude (Richter scale) versus current production time for 65 onshore gas fields, subdivided into maximum seismic magnitude range.*

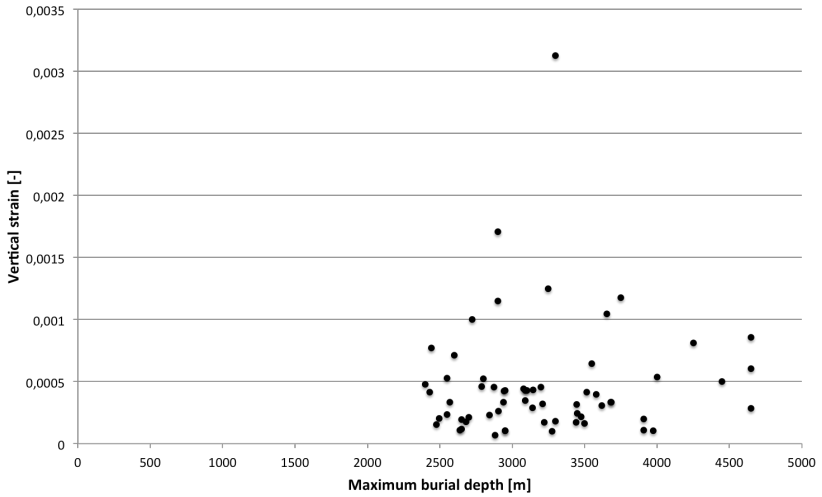

Figure 99: *Vertical strain versus maximum burial depth for 63 onshore gas fields.*

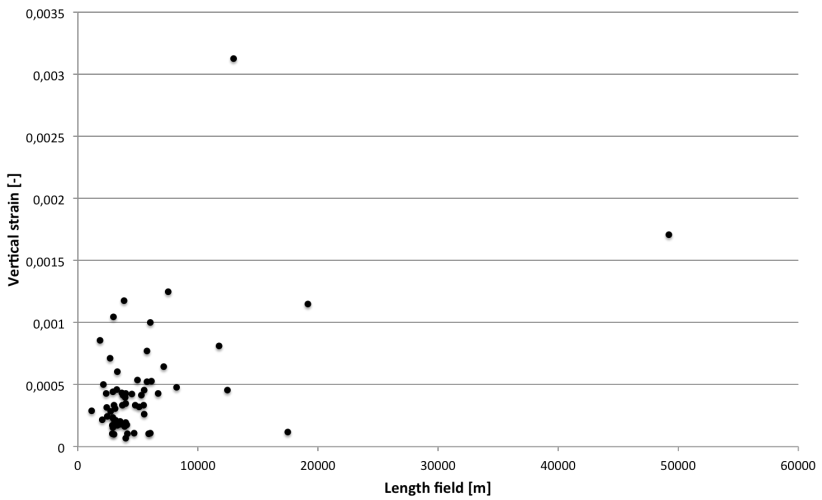

Figure 100: *Vertical strain versus field length for 63 onshore gas fields.*

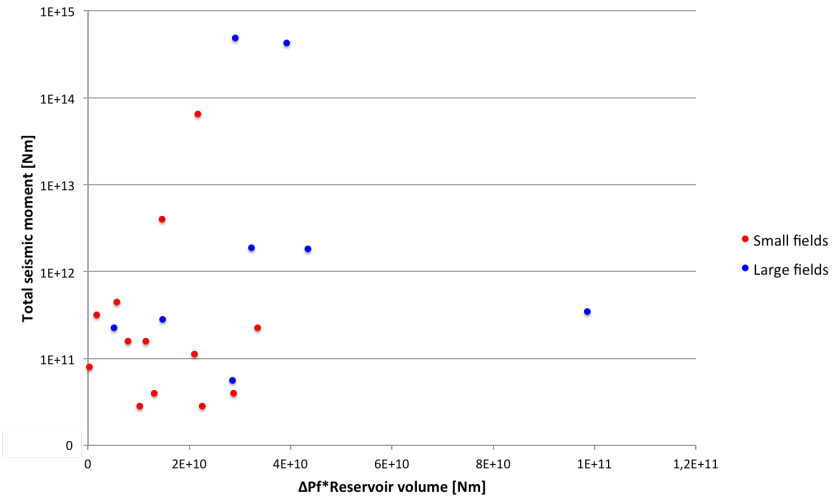

Figure 101: *Total seismic moment versus reservoir or field volume times ΔP_f for 21 seismic onshore gas fields, subdivided into small and large fields.*